



Title	Ultimate Shear Behavior and Modeling of Reinforced Concrete Members Jacketed by Fiber Reinforced Polymer and Steel
Author(s)	Jirawattanasomkul, Tidarut
Citation	北海道大学. 博士(工学) 甲第11131号
Issue Date	2013-09-25
DOI	10.14943/doctoral.k11131
Doc URL	<a href="http://hdl.handle.net/2115/53882">http://hdl.handle.net/2115/53882</a>
Type	theses (doctoral)
File Information	Tidarut_Jirawattanasomkul.pdf



[Instructions for use](#)

Ultimate Shear Behavior and Modeling of Reinforced Concrete Members Jacketed  
by Fiber Reinforced Polymer and Steel

連続繊維もしくは鋼板巻立て補強鉄筋コンクリート  
部材の終局せん断挙動とモデル

by  
Tidarut JIRAWATTANASOMKUL

A Dissertation in Civil Engineering Submitted in  
Partial Fulfillment of the Requirement for  
the Degree of Doctor of Philosophy

English Engineering Education Program (E3)  
Graduate School of Engineering  
Hokkaido University

September 2013

**ACKNOWLEDGEMENT**

I would like to express my sincere gratitude to my supervisor, Professor Tamon UEDA, for giving such a great opportunity to study in Japan, especially Hokkaido University. Your invaluable supports during this study are really appreciated.

I would like to extend my humble thanks to the committee members, Associate Professor Koshiro NISHIMURA, Associate Professor Yasuhiko SATO, Professor Hiroshi YOKOTA, Professor Takafumi SUGIYAMA, Professor Toshiro HAYASHIKAWA, and Professor Shunji KANIE. Your invaluable comments and kind guidance on technical knowledge truly help improve the quality of this dissertation.

I would like to extend my gratitude and appreciation to Dr. Werawan MANAKUL-UEDA, former program coordinator in English Engineering Education program, for all the supports, encouragements, kind assistance to my academic and non-academic matters.

My sincere gratitude is extended to Associate Professor Yasuhiko SATO and Assistant Professor Hitoshi FURUUCHI. I would also like to thank to Mr. Tsutomu Kimura for assisting and guiding during my experimental works. To the lab's members, thank you so much for sharing either happy or tough time together when we were conducting our experiments. I would especially like to thank my lovely friends and colleagues, at Laboratory of Engineering for Maintenance System who have always cared about my life, health, fatty, beauty and all matters.

To my best friends, Thana and Pitcha, thank you so much for your encouragement. I would also like to thank you all my friends here in Thailand and Japan, Oliver, Matteo, Kira and many friends whom I did not mention, for all your helps.

To my family, I have no word which can express my thanks for your supports, understanding, encouragement and especially your unconditional love.



Tidarut JIRAWATTANASOMKUL

2013/06/12

### ABSTRACT

Many existing reinforced concrete (RC) members built using old design codes are susceptible to catastrophic collapse during a major earthquake due to their insufficient shear strength and member ductility. Use of fiber-reinforced polymer (FRP) composites as the external bonding/jacketing material of RC members to improve their shear strength and ductility has been a widely used because of the high strength-to-weight ratio and corrosion resistance of FRP composites. The most often used FRP composites include carbon-fiber reinforced polymer (CFRP), glass-fiber reinforced polymer (GFRP), and aramid-fiber-reinforced polymer (AFRP) composites, which are termed conventional FRPs. In recent years, a new category of FRP composites, which are made of polyethylene naphthalate (PEN) or polyethylene terephthalate (PET) fibers, have emerged as an alternative to conventional FRPs as the strengthening materials of RC members. These FRPs have a much larger rupture strain (LRS) compared to conventional FRPs. Although their elastic modulus and strength are relatively low, they are much cheaper than conventional FRPs. It should be noted that the relatively low strength and modulus of LRS FRP can be compensated by the use of a greater amount of the fiber material, whereas the small rupture strain of conventional FRP cannot be compensated in this way. Up till now, it has remained unclear how to predict the shear strength of LRS FRP-strengthened RC members, which in turn influence their overall behaviors. Moreover, the efficiency of LRS FRP composites for the shear strengthening of RC members remains a concern because concrete degradation may occur before the full activation of the strain capacity of LRS FRP composites.

This research program aims to conduct an experimental study for the first time on the shear strength and deformation behavior of RC members strengthened with LRS FRP composites. Tests on ten RC beams strengthened in shear with fully wrapped PET FRP sheets have been conducted considering the following test parameters: the strengthening ratio, the longitudinal reinforcement ratio and the shear-span to effective-depth ratio. The increase in the amount of PET FRP sheets led to an increase of the shear strength and shear ductility, whereas a lower longitudinal reinforcement ratio and a smaller shear-span to effective-depth ratio corresponded to improved shear ductility. PET FRP sheets developed very high strains, namely the maximum strains of 1.4–6% at the peak shear loads and as high as 14.0% at the defined ultimate state (i.e., the load dropped by 20% compared to its peak load). Consequently, PET FRP sheets can be used to enhance the shear strength of RC beams while substantially increasing the member ductility. In particular, PET FRP sheets did not rupture at the peak load, and led to a ductile shear failure of the strengthened RC members. This failure mode also enabled us to clearly observe the behavior of shear strength degradation of concrete with increase in shear deformation even before the peak strength was developed. The shear contribution of concrete was found to degrade by 0–54.6% depending on the volumetric ratio of the FRP sheets, the shear-span to effective-depth ratio and the member depth. Owing to the close relationships among the concrete shear deterioration, the member shear deformation and the strain levels in both FRP sheets and transverse steel reinforcement as observed in the current study, further research work was carried out to build up a comprehensive model to explain the above relationships.

The development of a comprehensive shear strength model is proposed to precisely predict not only the concrete shear deterioration but also the overall load-deformation responses of RC members. The proposed model, based on the work of Sato et al., is extended to account for the stiffness of both flexural and shear reinforcements, enabling us to connect interaction between flexural and shear strength behaviors. To address this interaction, a flexure-shear interaction (FSI) analytical method is presented and verified using existing experimental results, and demonstrate shear strength and ductility enhancement of RC columns confined with several alternative jacketing materials, including CFRP, AFRP, PEN, and PET FRPs. As part of the overall analytical process, in specimens failing in shear, the reduction in load-carrying capacity with increase in deformation can be considered as a reduction of the contribution of the shear strength behavior caused by the reduction in secant stiffness of both shear and flexural reinforcements and residual concrete strength. However, in specimens failing in flexure, the load-carrying

capacity decreases due to concrete crushing along with the buckling of the compression reinforcement. The influence of the shear strength behavior on the flexural deformation is introduced through the tension shift phenomenon which increases the flexural deformation. Meanwhile, the flexural strength behavior affects the shear deformation through the yielding of flexural reinforcement, which decreases the shear strength of concrete and also increases the shear reinforcement strain, causing an increase of the shear deformation. The FSI analytical method can precisely predict the strain response of shear reinforcement, including the rupture of the FRP jackets. It is proven that FRP with high fracture strain (PEN and PET) is less likely to fracture than conventional fiber (Aramid and carbon) at ultimate deformation.

The final goal of this research program is to extend the FSI analytical method to the cases of steel-jacketed RC members with different jacketing shapes (i.e., elliptical and rectangular shapes). Comparing FRP and steel jacketing, FRP jacket can resist the shear crack opening only in the fiber alignment whereas steel jacket can resist the opening in both vertical and lateral, leading to different in the concrete shear strength and its degradation. Namely, concrete shear strength in steel jacketing is larger than that in FRP jacketing since shear crack opening restrained by a steel jacket causes the aggregate interlock of concrete, which results in it contributing to the shear resistance. In the FSI analytical method, the concrete contribution to the shear strength is therefore significantly affected by the steel jacket, and its contribution to shear strength is considered equivalent to that in a continuous transverse steel reinforcement. Considering confinement shape, elliptical steel jackets provides better enhancement of the flexural performance of inadequately confined columns than that of rectangular jacket. Using these concepts, the FSI analytical method can successfully predict the load-deformation envelope responses of RC columns with steel-jacketing. It can be concluded that the FSI analytical method is expeditious and efficient for use in predicting structural response of RC members with and without various types of seismic jacketing, while maintaining a high degree of accuracy.

Table of contents

<b>1. INTRODUCTION</b>	
1.1. INTRODUCTORY REMARKS	1
1.2. OBJECTIVES AND SCOPE	3
1.3. ORGANIZATION	4
<b>2. PREVIOUS RESEARCH AND BACKGROUND</b>	
2.1. INTRODUCTION	6
2.2. EXPERIMENTAL STUDIES	6
2.2.1. Beam tests	6
2.2.2. Column tests	7
2.3. MODELS FOR SHEAR STRENGTH	10
2.3.1. ACI 318-02 (2002)	10
2.3.2. Canadian standards (2004)	11
2.3.3. CEB-FIP model code (2011)	12
2.3.4. Japan Society of Civil Engineering (2007)	12
2.4. DEFORMATIONS	12
2.4.1. Flexural deformation	12
2.4.2. Shear deformation	12
2.4.3. Pull-out deformation	13
2.4.3.1. Slip of reinforcement at yield strain	13
2.4.3.2. Slip of reinforcement after yield	13
<b>3. EXPERIMENTAL SETUP AND RESULTS</b>	
3.1. INTRODUCTION	15
3.2. EXPERIMENTAL PROGRAMS	15
3.2.1. Details of specimens	15
3.2.2. Materials	16
3.2.2.1. Concrete and steel reinforcement	16
3.2.2.2. PET sheet	18
3.2.3. Test procedures and instrumentation	19
3.2.3.1. Loading system, strain gauges and total deformations	19
3.2.3.2. Shear deformation devices	20
3.3. RESULTS AND DISCUSSION	21
3.3.1. Failure modes and crack patterns	21
3.3.2. Overall load-deformation responses	23
3.3.3. Evaluation of shear deformation	26
3.3.4. Strain development in PET FRP sheets and transverse steel reinforcement	27
3.3.5. Degradation of the shear contribution of concrete	30
3.4. SUMMARY	32
<b>4. MATERIAL AND STRENGTH MODELS</b>	
4.1. INTRODUCTION	33
4.2. MATERIAL MODELS FOR STRENGTH ANALYSIS	33
4.2.1. Concrete	33
4.2.2. Steel reinforcement	34
4.2.3. FRP sheet	34
4.2.4. Confinement effect	35
4.3. FLEXURAL STRENGTH	37

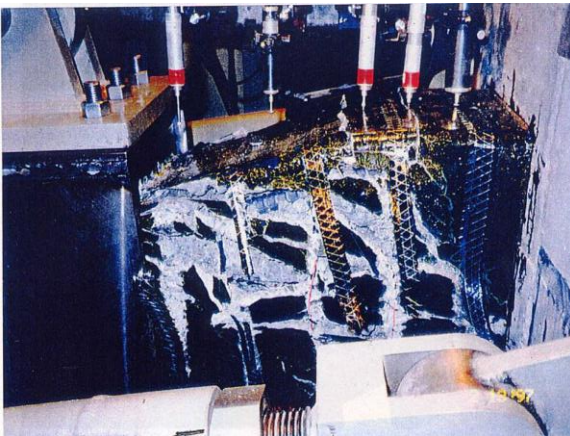
<b>4.4. SHEAR STRENGTH</b>	38
<b>4.5. INTERACTION BETWEEN FLEXURAL AND SHEAR STRENGTHS</b>	43
<b>4.6. DEFORMATIONS MODELS</b>	44
<b>4.6.1. Flexural deformation model</b>	44
<b>4.6.2. Shear deformation model</b>	45
<b>4.6.2.1. Shear deformation in pre-yielding region</b>	45
<b>4.6.2.2. Shear deformation in post-yielding region</b>	48
<b>4.6.3. Pull-out deformation model</b>	48
<b>4.7. INTERACTION OF FLEXURE AND SHEAR ON DEFORMATION MODEL</b>	48
<b>4.8. THE FSI ANALYTICAL PROCEDURE</b>	50
<b>4.9. SUMMARY</b>	52
<b>5. MODEL VERIFICATIONS</b>	
<b>5.1. INTRODUCTION</b>	53
<b>5.2. LOAD-DEFORMATION MODELS AND COMBINED RESPONSE</b>	53
<b>5.2.1. Comparison of peak shear strength from experiments and models</b>	53
<b>5.2.1.1. Beam tests</b>	53
<b>5.2.1.2. Column tests</b>	54
<b>5.2.2. Comparison of load-deformation from experiments and models</b>	56
<b>5.2.2.1. Experimental results of Anggawiddjaja et al.</b>	57
<b>5.2.2.2. Experimental results of Iacobucci et al.</b>	59
<b>5.2.2.3. Experimental results of Saatcioglu and Ozceb</b>	60
<b>5.2.2.4. Experimental results of Sezen et al.</b>	60
<b>5.2.2.5. Experimental results of Aboutaha et al. and Priestley et al.</b>	60
<b>5.2.3. Comparison of deformation components from experiments and models</b>	
<b>5.3. COMPARISON OF CALCULATED AND MEASURED SHEAR FORCE COMPONENTS</b>	62
<b>5.4. COMPARISON OF DEFORMATION COMPONENTS FROM EXPERIMENTS AND MODELS</b>	62
<b>5.5. SUMMARY</b>	64
<b>6. CONCLUSIONS AND FUTURE CONCERN</b>	
<b>6.1. CONCLUSIONS</b>	65
<b>6.1.1. Observed behavior of test specimens and evaluation of experimental data</b>	65
<b>6.1.2. Analytical methods</b>	65
<b>6.1.3. Applicable range of the proposed analytical methods</b>	66
<b>6.2. FUTURE CONCERNS</b>	67
<b>REFERENCES</b>	69
<b>APPENDIX A</b>	73

## CHAPTER 1

### INTRODUCTION

#### 1.1. INTRODUCTORY REMARKS

During the Great Hanshin Earthquake, many reinforced concrete (RC) columns collapsed catastrophically because of insufficient shear strength and low ductility. Shear failure is often brittle, catastrophic, and leads to severe damage at a low ductility level [48-49]. To improve seismic performance of existing columns, strengthening with Fiber Reinforced Polymer (FRP) is widely used because it shows great promise in high specific strength and corrosion resistance [8,31,63]. Conventional FRPs—Carbon Fiber Reinforced Polymer (CFRP) and Aramid Fiber Reinforced Polymer (AFRP)—are effective in enhancing shear strength, but they are brittle because of their low fracture strains (Fig. 1.1a), resulting in early rupture and loss of load-carrying capacity before the achievement of high ductility in shear-dominant cases [5-6,23]. To avoid this early rupture behavior, alternative FRP materials were developed with high fracture strain, in particular Polyethylene Naphthalate (PEN) and Polyethylene Terephthalate (PET), which enhance shear strength and ductility while being more economical [66]. Materials with high fracture strain often show low stiffness. The low stiffness can be compensated by the use of more material; however, the low fracture strain cannot be compensated in this way. Consequently, high-fracture-strain materials are preferable for achieving the required ductility performance (Fig. 1.1b).



(a) CFRP- jacketed RC member tested by Sirbu [61]



(b) PET- jacketed RC member tested by Senda [56]

**Fig. 1.1** Conventional FRP and large rupture FRP

Prediction of FRP-strengthened RC columns from the pre-peak to post-peak regions has been a great challenge for seismic engineers owing to the nonlinear behavior caused by complicated interactions between flexural and shear strength behaviors. Most design specifications to date [2,11-12,20,25,27-28] have ignored these interactions, although previous research [6,34,38-39,41] has revealed that the flexural strength behavior influences the shear strength behavior in the yielding of the reinforcement and also the concrete strength degradation. Many investigators [6,34,38-39,41] have reported a drop in potential shear strength capacity even before the maximum flexural strength is reached. Although the shear force carried

by the concrete remains almost constant before the longitudinal reinforcement yields, after yielding this shear force carried by concrete becomes smaller as the shear stress in the shear reinforcement continues to be increased. This phenomenon clearly shows that the shear force carried by the concrete, such as the dowel force and the contribution of compression zone, decreases after the main reinforcement deforms plastically. Meanwhile, the shear strength behavior significantly affects the flexural strength behavior related to the reduction of the neutral axis depth due to shear crack opening. Another limitation of existing designs is that the prediction method for the deformation and ductility does not account for both flexure and shear deformation mechanisms and their interaction. In reality, the decrease in secant stiffness of flexural reinforcement due to flexural yielding and concrete strength deterioration directly influences the shear deformation, and the tension shift effect in the truss mechanism after shear cracking induces an additional flexural deformation [40-41,65]. To increase confidence in the safety of RC columns with and without FRP jacketing, a precise analytical method to predict the load-deformation response should be established for all possible failure modes.

Among the most common analytical methods for predicting load-deformation response of RC columns is the section analysis method or so-called fiber model [13,21]. This method assumes that plane sections before bending remain plane after bending while ignoring the shear behavior. In reality, the shear behavior, such as the formation of shear cracks, significantly dominates the structural behavior. However, the performance of columns failing in shear or shear-flexure cannot be estimated by this section analysis, because the shear behavior is not taken into account. To consider the shear behavior, truss mechanism or strut-and-tie models [22,32,42] have been developed to predict shear strengths. However, the shear strengths estimated by these models vary over a wide range, and none of these models take into account the degradation of the shear behavior in their prediction of the post-peak behavior of RC columns precisely. To account for both flexural and shear behaviors, one research group has successfully developed the Modified Concrete Field Theory (MCFT) based on the Finite Element Method (FEM) [9,42,60,67-68]. In MCFT, a column is discretized into a large number of elements characterized by biaxial stresses and stiffness, and analyzed using a nonlinear FEM. However, such computations are complicated and impractical for engineering design. Consequently, empirical models have been developed for simplicity [34,41,52-54,57].

Prediction of the degradation in shear strength in RC columns subjected to reversed cyclic loading using empirical models has been proposed by many groups [33,34,41,52-54,57] in the context of catastrophic shear failure related to diagonal shear cracking. Their models describe reasonably well the degradation of the shear strength on increasing the flexural deformation. However, the shear strength capacity is significantly degraded by the total deformation rather than by only the flexural deformation [19,71], so these models are inherently imprecise. In RC columns, the total deformation consists of flexural, shear, and pull-out deformations. Each deformation component not only degrades the shear strength, but also affects the shear strength behavior. Sato et al. [52-54] proposed a model for the shear strength of RC members that accounts for the stiffness of the flexural and shear reinforcements rather than using a deformation-based approach. In their models, the yielding of reinforcements causes a reduction of equivalent stiffness or so-called secant stiffness, leading to a reduction in the shear strength. Moreover, they proposed the use of the average strain of shear reinforcement based on the reduction of the tension stiffness of concrete surrounding the shear reinforcement. This allows the shear reinforcement fracture to be predicted. Although these models were successful, they were verified by separating shear strength contribution into many complicated components.

To address these deficiencies, a flexure-shear interaction (FSI) analytical method is presented which allows a more precise prediction of the load-deformation responses of RC columns with or without

FRP-jacketing. In this FSI analytical method, conventional section analysis is applied by including a parameter for the confinement ratio as a function of the secant stiffness of the transverse steel and fiber reinforcements. By including the effects of shear, the truss mechanism proposed by Sato et al. [52-54] is combined with the section analysis. After the onset of shear cracks, the additional flexural deformation due to the tension shift phenomenon is included for a more precise prediction of the flexural deformation. Use of a shear deformation model based on the truss mechanism accounts for the effects of tension stiffening, fiber confinement and proposed strut angle. The shear and flexural deformations are combined with the pull-out deformations to obtain an accurate prediction of the total deformations of the columns. The proposed analytical method is verified using existing experimental results, and demonstrate shear strength and ductility enhancement of RC columns confined with both low and high fracture strain fiber materials, including CFRP, AFRP, PEN and PET FRP sheet.

The final goal of this research program is to extend the FSI analytical method to predict peak shear strength in the cases of steel-jacketed RC members with different jacketing shapes (i.e., elliptical and rectangular shapes). Comparing FRP and steel jacketing, FRP jacket can resist the shear crack opening only in the fiber alignment whereas steel jacket can resist the opening in both vertical and lateral, leading to different in the concrete shear strength and its degradation. Namely, concrete shear strength in steel jacketing is larger than that in FRP jacketing since shear crack opening restrained by a steel jacket causes the aggregate interlock of concrete, which results in it contributing to the shear resistance. In the FSI analytical method, the concrete contribution to the shear strength is therefore significantly affected by the steel jacket, and its contribution to shear strength is considered equivalent to that in a continuous transverse steel reinforcement. Considering confinement shape, elliptical steel jackets provides better enhancement of the flexural performance of inadequately confined columns than that of rectangular jacket. Using these concepts, the FSI analytical method can successfully predict the load-deformation envelope responses of RC columns with steel-jacketing. It can be concluded that the FSI analytical method is expeditious and efficient for use in predicting structural response of RC members with and without various types of seismic jacketing, while maintaining a high degree of accuracy.

## **1.2. OBJECTIVES AND SCOPE**

In this study, the conventional section analysis approach or fiber model was modified for shear behavior to be applicable for displacement-based evaluation of reinforced concrete members. The numerical analysis of RC members was verified by means of a series of experiments on both beams and columns strengthened with and without seismic jacketing. Those RC members were tested under monotonic and reversed cyclic loading; parameters such as steel reinforcement and fiber ratio were varied. Therefore, the objective of this research study is to develop the model for predicting the strength and deformation of members with and without seismic retrofitting at ultimate state.

- 1) The experimental program involves only PET FRP wrapped RC beams.
- 2) To develop accurate predictive shear strength model with consideration of confinement effect and strain development in FRP jacket, steel jacket and steel reinforcement.
- 3) In the case of FRP jacketing, both conventional FRPs (i.e., CFRP and AFRP) and LRS FRPs (i.e., PEN and PET FRP) considered in this research program are solely fully wrapped FRPs.
- 4) In the case of steel jacketing, RC columns are strengthened by welded steel plates so brittle shear failure can be prevented and the column can develop its ultimate flexural capacity.

- 5) In FSI analytical method, the following features are considered:
- a. A shear strength model represents degradation of shear strength in post-peak region;
  - b. A shear deformation model along the plastic hinge zone is considered in the pre- and post-yielding regions;
  - c. A flexural strength model considering confinement effects of transverse reinforcement and jacket (i.e., FRP and steel plates);
  - d. An additional flexural deformation model is taken into account owing to tension shifting;
  - e. The interactions between shear and flexural strength behaviors include (i) neutral axis depth reduction due to shear cracking, (ii) flexural reinforcement stress increase due to shear cracking (tension shift effect), (iii) effects of yielding of flexural reinforcement on shear strength, and (iv) effect of concrete compression softening on shear strength.
- 6) The proposed analytical method is demonstrated to predict accurately the pre-peak and post-peak load-deformation response, including the strain response of shear reinforcement until the ultimate point of the rupture of non- and FRP-jacketed RC columns.

### **1.3. ORGANIZATION**

The dissertation is divided into six chapters and basic contents of each chapter are shown in Fig 1.2. In Chapter 2 the background of previous experiments tested by other researchers and shear strength model codes is described. Then, in Chapter 3, the details of experimental programs and results are described. In Chapter 4 the relevant models for prediction of load-deformation responses (i.e., stress-strain relationships, flexural strength, shear strength, and deformation models) are outlined. In addition, the related computational procedures are outlined. Chapter 5 describes the verifications and application of the proposed models to a set of test specimens. Finally, Chapter 6 provides conclusions and future concerns.

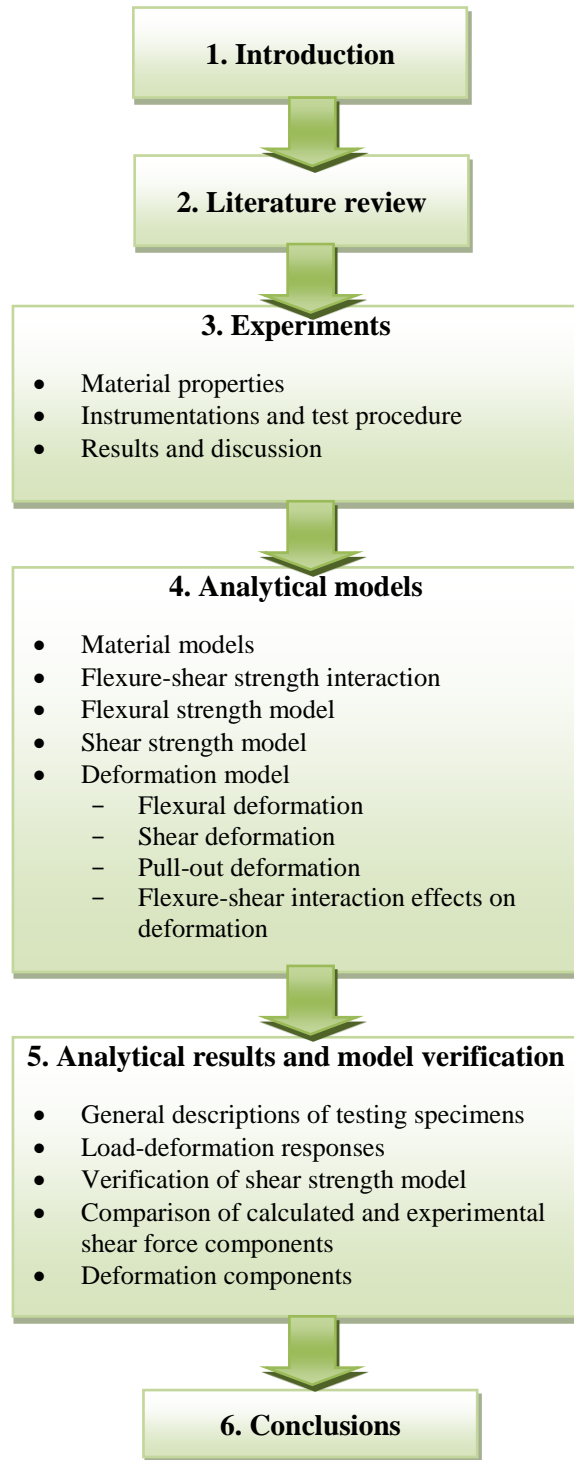


**Fig. 1.2.** Organizations of dissertation

CHAPTER 2

PREVIOUS RESEARCH AND BACKGROUND

2.1. INTRODUCTION

This chapter provides a general review of the behavior of reinforced concrete members which are strengthened with fiber reinforced polymers (FRPs) and steel plates subjected to cyclic loading. Background information on the material characteristics of confined concrete, steel with hardening stage, FRP with high fracturing strain, and mechanism of RC members strengthened by FRP is reviewed. In addition, summary of the previous experimental research on this topic is studied including an examination of the various key parameters and failure mechanisms.

2.2. EXPERIMENTAL STUDIES

2.2.1. Beam tests [30,44]

The experimental results of RC beams with and without PET FRP-jacketed failing in shear [30,44] were taken to investigate shear strength behaviors. The example of cross section and characteristics of beam specimens are shown in Fig. 2.1. The details of beam specimens are presented in Table 2.1.

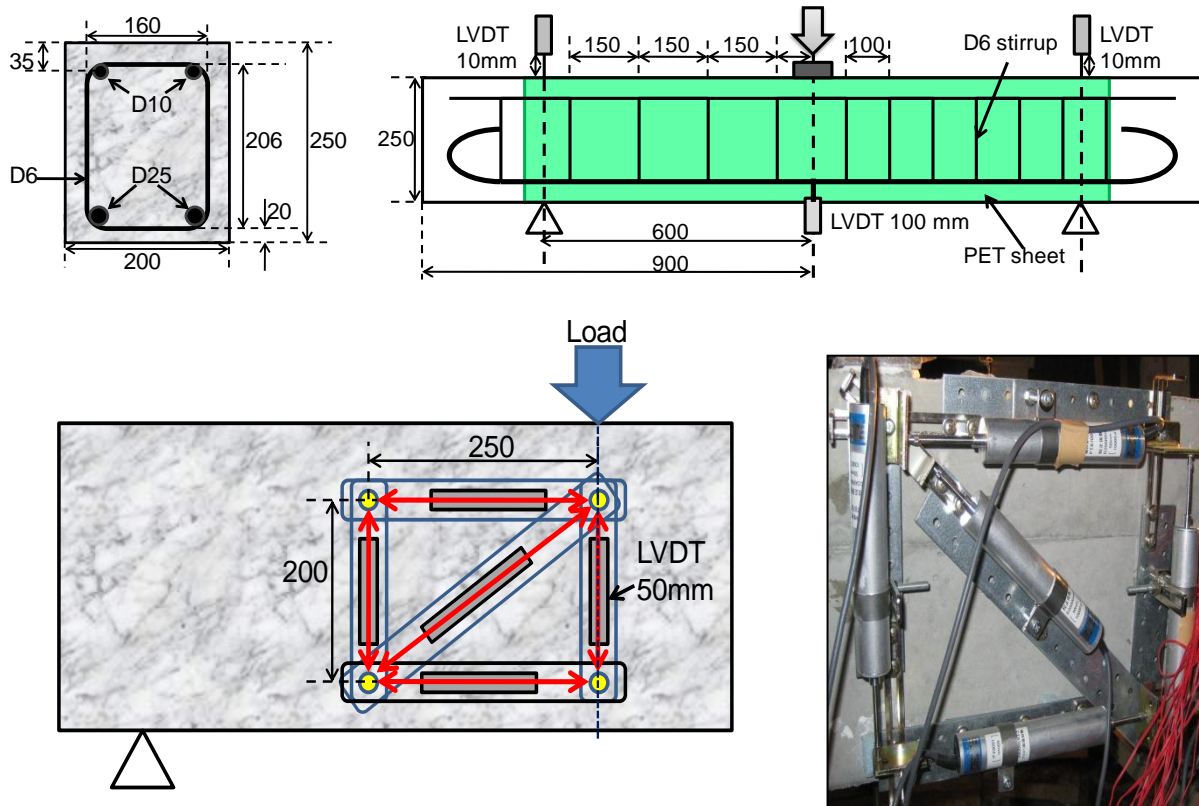


Fig. 2.1 Cross section and characteristics of specimens [30]

**Table 2.1** Details of beam specimens [30,44]

Specimen	$f_c$ (MPa)	$f_{cc}$ (MPa)	$a/d$ -	$p_s E_s$	$p_w E_w$	$p_f E_f$	$V_{c-cal}$ (kN)	$V_{s-cal}$ (kN)	$V_{exp}$ (kN)	$V_{cal}$ (kN)	$V_{exp}/V_{cal}$ (kN)
B1 <sup>[30]</sup>	36.0	36.0	2.8	209.0	188.1	0.00	83.3	42.2	90.0	125.4	0.72
B2 <sup>[30]</sup>	36.0	52.7	2.8	209.0	188.1	0.00	106.4	72.7	N/A	179.1	N/A
B3 <sup>[30]</sup>	36.0	46.6	2.8	209.0	188.1	0.00	101.7	66.3	N/A	168.0	N/A
B4 <sup>[30]</sup>	36.0	49.1	2.8	209.0	188.1	0.00	103.7	69.0	N/A	172.6	N/A
B5 <sup>[6]</sup>	36.0	40.1	2.8	209.0	188.1	0.00	95.6	58.7	N/A	154.3	N/A
R8 <sup>[44]</sup>	26.7	26.7	3.36	286.9	289.8	0.00	75.7	30.2	81.2	105.9	0.77
R9 <sup>[44]</sup>	29.6	29.6	3.36	860.7	869.4	0.00	117.0	20.7	106.4	137.7	0.77
R10 <sup>[44]</sup>	29.6	29.6	3.36	430.4	434.7	0.00	91.2	31.9	76.7	123.2	0.62
R11 <sup>[44]</sup>	26.0	26.0	3.36	430.4	434.7	0.00	94.7	25.9	91.2	120.6	0.76
R12 <sup>[44]</sup>	34.0	34.0	3.6	860.7	869.4	0.00	126.9	16.7	111.6	143.6	0.78
R13 <sup>[44]</sup>	32.3	32.3	3.6	286.9	289.8	0.00	77.6	26.9	152.4	104.5	1.46
R14 <sup>[44]</sup>	29.0	29.0	3.36	860.7	869.4	0.00	116.4	20.5	91.2	136.9	0.67
R15 <sup>[44]</sup>	29.9	29.9	3.6	430.4	434.7	0.00	89.4	24.0	142.4	113.4	1.26
R16 <sup>[44]</sup>	31.6	31.6	3.6	430.4	434.7	0.00	97.2	23.7	142.4	120.9	1.18
R20 <sup>[44]</sup>	43.0	43.0	3.36	286.9	289.8	0.00	85.2	38.3	91.6	123.6	0.74
R21 <sup>[44]</sup>	48.2	48.2	3.6	860.7	869.4	0.00	129.2	20.8	152.4	150.0	1.02
R22 <sup>[44]</sup>	29.5	29.5	4.5	430.4	434.7	0.00	82.7	26.0	81.2	108.7	0.75
R23 <sup>[44]</sup>	30.2	30.2	2.24	430.4	434.7	0.00	112.5	35.5	100.7	148.1	0.68
R24 <sup>[44]</sup>	30.9	30.9	5.05	860.7	869.4	0.00	110.7	13.0	93.9	123.7	0.76
R25 <sup>[44]</sup>	30.8	30.8	3.6	860.7	869.4	0.00	115.5	16.6	106.6	132.1	0.81
R26 <sup>[44]</sup>	36.6	36.6	2.4	430.4	434.7	0.00	107.6	33.2	152.4	140.8	1.08
R27 <sup>[44]</sup>	13.7	13.7	3.6	430.4	434.7	0.00	78.8	15.6	96.6	94.5	1.02
R28 <sup>[44]</sup>	31.6	31.6	3.6	860.7	857.8	0.00	124.3	16.3	182.8	140.6	1.30

N/A = cannot observe the ultimate load due to the flexural failure

### 2.2.2. Column tests

To evaluate the applicability and accuracy of the FSI analytical method, experimental results of twenty tests on RC columns failing in shear, flexure-shear and flexure were compiled. Fig. 2.2 shows a test setup and an example of a specimen tested by Anggawiddjaja et al. [5-6]. Data sets of a total of fifteen square RC columns (denoted as SP) tested by Anggawiddjaja et al. [5-6] are used, involving various types of FRP jackets, Aramid, PEN and PET fibers. The cross-sections of their columns are 400×400 mm<sup>2</sup> and 600×600 mm<sup>2</sup>, as shown in Fig. 2.3a.

Data sets of RC columns tested by Iacobucci et al. [23] are also used. In their study, reinforced concrete square columns with insufficient shear steel reinforcement were used to represent existing old columns designed according to old seismic specifications. Their main focus was on testing RC columns with and without CFRP jacketing under lateral cyclic displacement and high axial load ratio ( $P/f_{co}A_g$ ). Their columns are denoted as AS and ASC with a cross-section of 305×305 mm<sup>2</sup>, as shown in Fig. 2.3b. Additionally, the FRP was aligned along the entire height of the specimens. The fibers were oriented perpendicular to the longitudinal axis of the column or in the shear direction. According to the flat coupon tensile tests [5-6,23], the fracture strains of Aramid, PEN, PET and carbon fiber composite are 4.1%, 4.5%, 13.8% and 1.26%, respectively. More data sets on plain RC columns failing in shear tested by

Saatcioglu and Ozceb [51] and by Sezen et al. [57] are used to verify the applicability of the analytical method to typical reinforced concrete. In their study, reinforced concrete square columns are used with varied shear steel reinforcement ratio, concrete compressive strength and axial load ratio. Their columns are denoted as U1-U4, 2CLD12, 2CHD12, 2CVD12 and 2CLD12M with a cross-section of  $350 \times 350 \text{ mm}^2$  and  $457 \times 457 \text{ mm}^2$ , as shown in Figs. 2.3c and 2.3d. Data sets of RC columns tested by Aboutaha et al. [1] and Priestley et al. [45-46] to investigate the effect of rectangular and elliptical steel jackets. The columns from Aboutaha et al. [1] are denoted as SC with an original cross-section of  $457 \times 914 \text{ mm}^2$ , whereas the columns from Priestley et al. [45-46] are denoted as R with an original cross-section of  $406 \times 610 \text{ mm}^2$ . Cross-sections of their specimens are also illustrated in Figs. 2.3e and 2.3f.

The details of the specimens are previously shown in Table 2.2, in which column (1) shows the specimen labels, and the types of FRP jacket, when applicable are shown in columns (2). The material and geometry properties are shown in columns (3) to (10) in the order of shear-span to effective-depth ratio ( $a/d$ ), unconfined concrete compressive strength ( $f'_{co}$ ), ratio of the tension reinforcement ( $\rho_s$ ), ratio of steel shear reinforcement ( $\rho_w$ ), volumetric ratio of fiber reinforcement ( $\rho_f$ ) and an axial load ratio ( $P/f'_{co}A_g$ ). The failure mode, as shown in column 11, corresponds to the definitions which will be explained later.

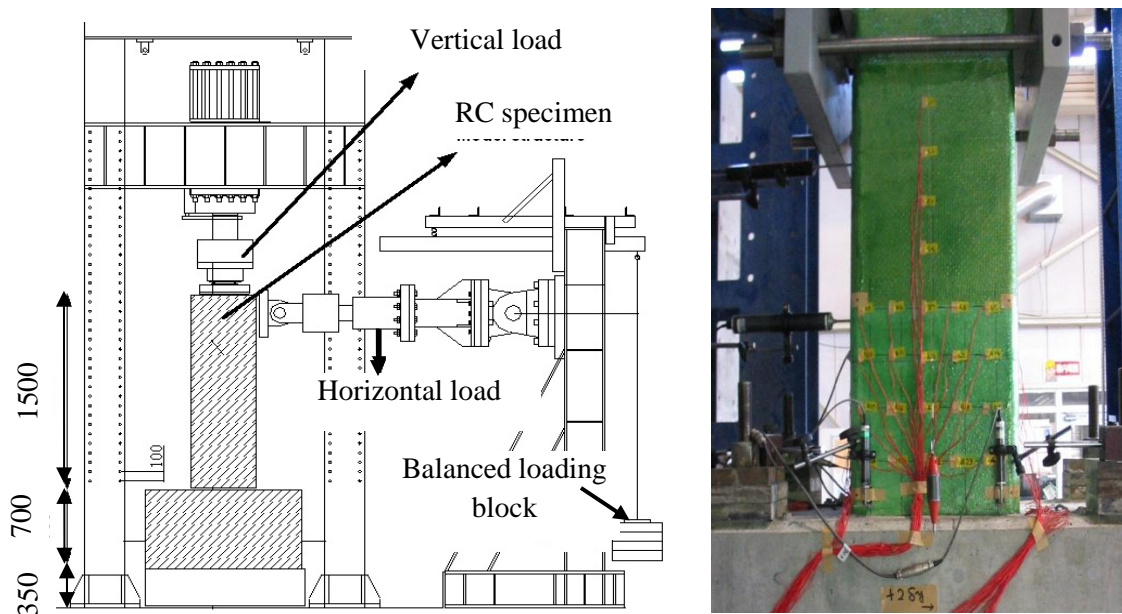


**Fig. 2.2** Test setup and an example of specimen tested by Anggawidjaja et al. [5-6]

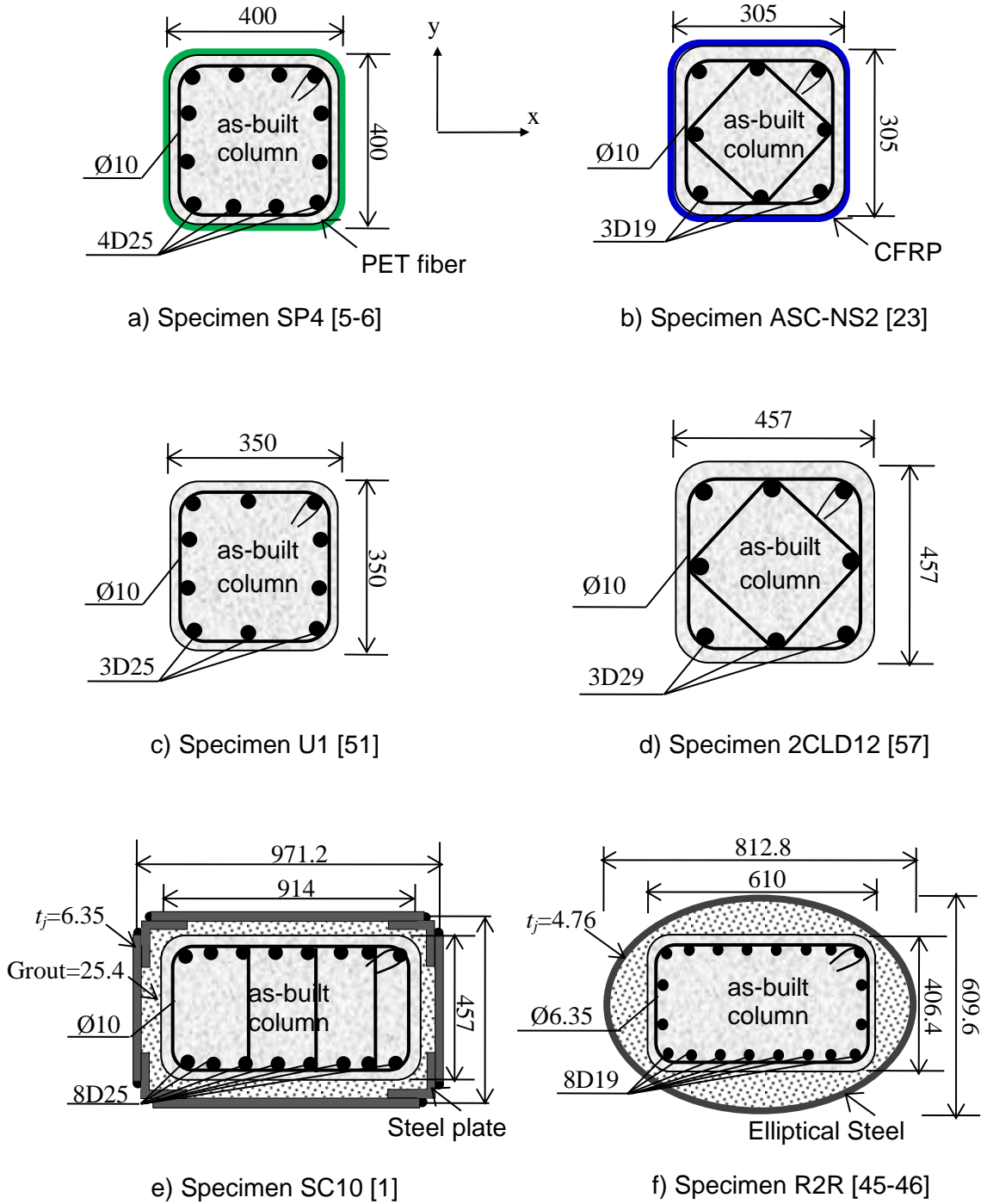


Fig. 2.3 Cross section and characteristics of column specimens [1,5-6,23,45-46,51,57]

**Table 2.2** Details of column specimens [1,5-6,23,45-46,51,57]

Reference	Specimen	Fiber	<i>b</i>	<i>h</i>	<i>a/d</i>	<i>f'co</i>	$\rho_s$	$\rho_w$	$\rho_f$	$P/A_g f'co$	Failure	
	(1)	(2)	(3)	(4)	(5)	(6)	(7)	(8)	(9)	(10)	(11)	
Aboutaha et al. [1]	SC9	None	914	457	3	16.0	2.20	0.10	0.00	0.00	Mode II	
	SC10	Steel	914	457	3	16.5	2.20	0.10	2.50	0.00	Mode III	
	SP1	None	400	400	3	29.5	2.87	0.16	0.00	0.03	Mode II	
	SP2	Aramid	400	400	3	29.5	2.87	0.16	0.13	0.03	Mode IV	
	SP3	PEN	400	400	3	29.5	2.87	0.16	0.38	0.03	Mode IV	
	SP4	PET	400	400	3	29.5	2.87	0.16	0.37	0.03	Mode III	
	SP5	PET	400	400	3	31.7	2.87	0.16	0.19	0.03	Mode III	
	SP6	PET	400	400	4	31.7	2.87	0.16	0.12	0.03	Mode III	
	Anggawidjaja et al. [5-6]	SP7	PET	400	400	4	31.7	2.87	0.16	0.06	0.03	Mode III
		SP8	None	400	400	4	31.7	2.87	0.16	0.00	0.03	Mode II
SP9		PET	400	400	4	31.7	3.59	0.16	0.12	0.03	Mode III	
SP10		PET	400	400	4	31.7	2.15	0.16	0.06	0.03	Mode III	
SP11		PET	600	600	4	31.7	2.82	0.20	0.25	0.03	Mode III	
SP12		PET	600	600	4	31.7	2.82	0.20	0.125	0.03	Mode III	
SP13		PET	600	600	4	34.5	2.82	0.20	0.29	0.03	Mode III	
SP14		PET	600	600	4	23.7	2.82	0.09	0.42	0.03	Mode III	
SP15		PEN	600	600	4	31.1	2.82	0.09	0.42	0.03	Mode III	
Iacobucci et al. [23]		AS-NS1	None	305	305	3	31.4	1.30	0.61	0.00	0.40	Mode II
	ASC-NS2	CFRP	305	305	3	36.5	1.30	0.61	0.65	0.38	Mode III	
	ASC-NS3	CFRP	305	305	3	36.9	1.30	0.61	1.30	0.65	Mode III	
	ASC-NS4	CFRP	305	305	3	36.9	1.30	0.61	0.65	0.65	Mode III	
	ASC-NS5	CFRP	305	305	3	37.0	1.30	0.61	1.96	0.65	Mode III	
Priestley et al. [45-46]	R1A	None	610	416.4	2.8	24.8	1.30	0.14	0.00	0.06	Mode II	
	R2R	Steel	610	416.4	2.8	25.2	1.30	0.14	1.56	0.06	Mode IV	
Saatcioglu and Ozceb [51]	U1	None	350	350	3.3	43.6	3.3	0.3	0	0.00	Mode III	
	U2	None	350	350	3.3	30.2	3.3	0.3	0	0.16	Mode III	
	U3	None	350	350	3.3	34.8	3.3	0.6	0	0.14	Mode III	
	U4	None	350	350	3.3	34.8	3.3	0.9	0	0.14	Mode III	
Sezen et al. [57]	2CLD12	None	457	457	3.7	21.1	2.5	0.17	0	0.15	ModeII	
	2CHD12	None	457	457	3.7	21.1	2.5	0.17	0	0.61	ModeII	
	2CVD12	None	457	457	3.7	20.9	2.5	0.17	0	0.51	ModeII	
	2CLD12M	None	457	457	3.7	21.8	2.5	0.17	0	0.15	ModeII	

\*Mode I = Brittle shear failure, Mode II = Brittle shear failure after yielding, Mode III = Less brittle shear failure after yielding, and Mode IV = Flexural failure

### 2.3. MODELS FOR SHEAR STRENGTH

#### 2.3.1. ACI 318-05 [2]

According to the ACI 318-2005 [2], the nominal shear strength,  $V_n$ , is calculated as the summation of contributions from concrete,  $V_c$ , and the transverse reinforcement,  $V_s$ .

$$V_n = V_c + V_s \tag{2.1}$$

$$V_c = 0.166 \left( 1 + \frac{P}{13.8A_g} \right) \sqrt{f'_c} b d \quad (\text{unit: MPa}) \quad (2.2)$$

an effective shear area of  $A_e = 0.8bh = 0.8A_g$  for rectangular columns, where  $A_g$  is gross column area. The shear reinforcement contribution is calculated as follows:

$$V_s = \frac{A_v f_y d}{s} \quad (2.3)$$

### 2.3.2. Canadian Standard (CSA- 2004) [11]

Given this shear model for beams, the shear strength of a member can be taken as a combination of an aggregate interlock component ( $V_c$ ), a steel component that depends on the number of stirrup legs that cross the diagonal shear crack ( $V_s$ ), and the vertical component of any prestressing force ( $V_p$ ). Thus the shear strength of members in the CSA code is taken as

$$V_n = V_c + V_s + V_p \quad (2.4)$$

However,  $V_r$  shall not exceed

$$V_n = 0.25 \sqrt{f'_c} b_w d_v \quad (2.5)$$

The value of  $V_c$  shall be computed from

$$V_c = \phi_c \lambda \beta \sqrt{f'_c} b_w d_v \quad (2.6)$$

In the determination of  $V_c$ , the term  $\sqrt{f'_c}$  shall not be taken greater than 8 MPa. For members with transverse reinforcement perpendicular to the longitudinal axis,  $V_s$  shall be computed from

$$V_s = \frac{\phi_s A_v f_y d_v \cot \theta}{s} \quad (2.7)$$

where  $b_w$  is the web width,  $d_v$  is the flexural lever arm in the beam,  $\phi_c$  is the resistance factor for concrete,  $\lambda$  is a factor to account for low-density concrete,  $\beta$  is a factor to account for aggregate interlock in concrete members,  $f'_c$  is the concrete cylinder strength,  $A_v$  is the area of transverse reinforcement,  $\phi_s$  is the resistance factor for reinforcing steel,  $f_y$  is the yield strength of the reinforcement,  $s$  is the spacing of the shear reinforcement, and  $\theta$  is the angle of average principal compression in the beam with respect to the longitudinal axis.

The shear area used in the 2004 CSA code is the web width ( $b_w$ ) multiplied by the flexural lever arm ( $d_v = 0.9d$ ) rather than by the effective depth,  $d$ , as used by the ACI code and the 1994 CSA simplified method. This has been selected because it is closer to the reality of how shear is resisted by a section. Consider that taking the shear area to the top of the cross section implicitly means that the top surface of the member resists a shear stress when it is well known that shear stresses must approach zero at the top and bottom surfaces of a member. An additional limit in the use of Eq. (2.6) is that the value of  $\sqrt{f'_c}$  is not to be taken as greater than 8 MPa, similar to the ACI restriction for high-strength concrete. Eq. (2.6) also shows the maximum shear strength limit, which is based on the crushing capacity of cracked concrete in diagonal compression. Experiments have shown that concrete members can resist much higher shear stresses than those suggested by the traditional ACI maximum shear limit as used in the 1994 CSA simplified method.

To determine the shear strength of a member by the general method, it is necessary to determine the values of  $\beta$  and  $\theta$  for use in Eq. (2.6). These have generally been defined with respect to the three shear parameters discussed in the following sections.

### 2.3.3. CEB-FIP Model code [12]

In CEB-FIP Model code the classical design tasks like design for shear, torsion and punching are found.

$$V_n = V_c + V_s \quad (2.8)$$

The value of  $V_c$  shall be computed from

$$V_c = \phi_c \lambda \beta \sqrt{f'_c} b_w d_v \quad (2.9)$$

In the determination of  $V_c$ , the term  $\sqrt{f'_c}$  shall not be taken greater than 8 MPa. For members with transverse reinforcement perpendicular to the longitudinal axis,  $V_s$  shall be computed from

$$V_s = \frac{\phi_s A_v f_y d_v \cot \theta}{s} \quad (2.10)$$

### 2.3.4. Japan Society of Civil Engineering [25]

For a linear member provided with transverse steel reinforcement, the shear force is carried by transverse steel reinforcement after the initiation of diagonal cracks and the load-carrying mechanism is transformed to a truss mechanism.

$$V_n = V_c + V_s \quad (2.11)$$

$$V_c = 0.2 \left( \sqrt[4]{1000/d} \right)^3 \sqrt[3]{100 \rho_w f'_c} b d \quad (2.12)$$

$$V_s = \frac{A_v f_y z}{s}, z = \frac{d}{1.15} \quad (2.13)$$

## 2.4. DEFORMATIONS

Total deformation of RC columns generally consists of three components which are flexural, shear and pull-out deformation. Although for simplicity these three deformations are considered to occur independently, they actually interact with each other.

### 2.4.1. Flexural deformation

The flexural deformation can be obtained by integrating curvature along the column length as in Eq.(2.14). This curvature is calculated from section analysis as discussed in the flexural behavior.

$$\Delta_{flexure} = \int_0^l \int_0^l \phi dz dz \quad (2.14)$$

### 2.4.2. Shear deformation

The most common method to predict shear deformation is through the use of truss mechanism. The truss mechanism is considered to be applicable after diagonal shear crack forms in the structure. Before the formation of flexural or diagonal cracks, the shear deformation is predicted by using the principles of

elasticity. The truss mechanism considers the shear deformation is caused due to shortening of compression strut ( $\delta_{s1}$ ) and elongation of tension tie ( $\delta_{s2}$ ). The equations are as follows:

$$\delta_{s1} = \frac{V_s}{E_c b_w (\cot \theta + \cot \alpha) \sin^4 \theta} \quad (2.15)$$

$$\delta_{s2} = \frac{V_s s}{E_w \left[ A_w + \frac{E_c}{E_w} A_{ce} \right] (\cot \theta + \cot \alpha) \sin^3 \alpha} \quad (2.16)$$

Ueda et al. [65] proposed a shear deformation model based on truss mechanism which considers the effect of concrete effective in concrete and additional flexural deformation due to shear cracking. Fig. 2.4 shows the truss mechanism model from Ueda et al. [65].

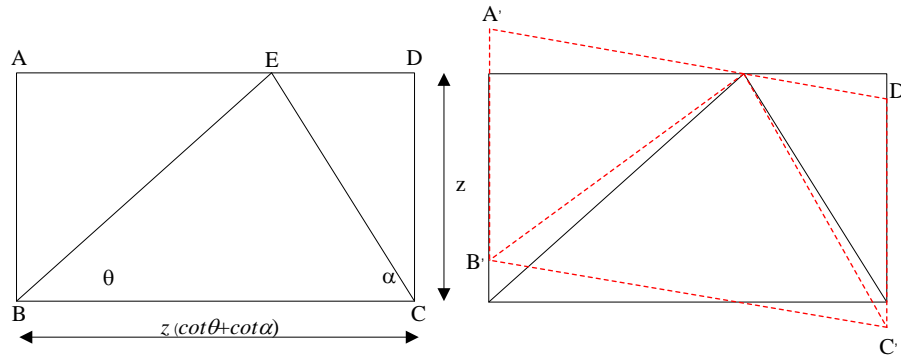


**Fig. 2.4** Shear deformation based on truss analogy [65]

### 2.4.3. Pull-out deformation

The slip of reinforcement is predicted analytically at the yielding load using Eqs. (2.17) and (2.18), and after yielding of longitudinal reinforcement using Eqs. (2.19) and (2.20). The pullout deformation equations proposed by Shima et al. [59] for different stages of reinforcement strain are as follow:

#### 2.4.3.1. Slip of reinforcement at yield strain

$$S = \frac{7.4 \alpha_y \cdot \varepsilon_y (2 + 3500 \varepsilon_y)}{f'_{ck}{}^{2/3}} \cdot \varphi \quad (2.17)$$

$$\alpha_y = 1 + 0.9 e^{0.45(1 - \frac{C_s}{\varphi})} \quad (2.18)$$

#### 2.4.3.2. Slip of reinforcement after yield

$$S = s \cdot \frac{\varphi}{K f_c} \quad (2.19)$$

where  $s$ - value is different for each strain level of reinforcement

- When the reinforcement strain takes the value of yield strain ( $\varepsilon_y$ )

$$s = \varepsilon_y (2 + 3,500 \varepsilon_y) \cdot \alpha_y \quad (2.20)$$

- When the reinforcement strain is at the initiation point of strain hardening area ( $\varepsilon_{sh}$ )

$$s = 0.5(\varepsilon_{sh} - \varepsilon_y) + s(\varepsilon_y) \quad (2.21)$$

- When the reinforcement strain takes the value at the change in gradient of the non-dimensional slip in the reinforcement strain hardening area ( $\varepsilon_a$ )

$$s = 0.08(f_u - f_y)(\varepsilon_a - \varepsilon_{sh}) + s(\varepsilon_{sh}) \quad (2.22)$$

$$\varepsilon_a = \varepsilon_{sh} + \left( \frac{0.132 - \frac{s(\varepsilon_y)}{2}}{0.13(f_u - f_y)} \right) \quad (2.23)$$

- When the reinforcement strain is greater than  $\varepsilon_a$

$$s = 0.027(f_u - f_y)(\varepsilon_s - \varepsilon_a) + s(\varepsilon_a) \quad (2.24)$$

where

- $S$  = pullout of reinforcement (cm),
- $\alpha_y$  = effect of bar spacing,
- $\varphi$  = diameter of reinforcement bar (cm),
- $f'_{ck}$  = strength of footing concrete (N/mm<sup>2</sup>),
- $f_y$  = yield strength of reinforcement (N/mm<sup>2</sup>),
- $f_u$  = tensile strength of reinforcement (N/mm<sup>2</sup>),
- $C_s$  = bar spacing (cm),
- $\varepsilon_y$  = strain at reinforcement yield,
- $\varepsilon_{sh}$  = strain at initiation of reinforcement strain hardening,
- $\varepsilon_a$  = point of non-dimensional slip gradient change in strain hardening area,
- $\varepsilon_s$  = reinforcement strain.

By substituting the slip of reinforcement ( $S$ ) value to Eq. (2.19), deformation of piers due to pullout of reinforcement can be obtained analytically.

## CHAPTER 3

### EXPERIMENTAL SETUP AND RESULTS

#### 3.1. INTRODUCTION

This chapter presents an experimental study on the shear behavior of reinforced concrete (RC) members fully wrapped with polyethylene terephthalate (PET) fiber reinforced polymer (FRP) composites, which are a new type of FRP material characterized with a much larger rupture strain (LRS) compared to conventional FRPs (i.e., made of carbon, glass, and aramid fibers). A total of ten PET fully-wrapped RC beams, which were designed to fail in shear and with different shear-span to effective-depth ratios, transverse reinforcement ratios and shear strengthening ratios, were tested under four-point bending loads. The overall load-deflection responses and the shear deformation of the beams as well as the strain development of the transverse steel reinforcement and the FRP jackets were carefully observed. Based upon the extensive strain measurements, the shear contributions by concrete, FRP and transverse reinforcement are differentiated. The behavior of PET FRP composites as the jacket material of RC members will be reported by use of nominal shear stress and drift ratio at mid-span. The failure modes and crack patterns will be shown and compared with that of the control RC beam. Shear deformation was also measured and calculated to evaluate the effect of shear crack opening with different strengthening ratio, longitudinal reinforcement ratio, and shear-span to effective-depth ratio. Moreover, the distribution of strain developed in FRP sheets and transverse steel reinforcement will be shown in order to clarify the influence of FRP sheets.

#### 3.2. EXPERIMENTAL PROGRAMS

##### 3.2.1. Details of Specimens

Ten simply-supported RC beams designed to fail in shear were subjected to four-point bending loads. RC beams rather than RC columns as the test members allows the elimination of the effects of pull-out from footings and lateral buckling of the longitudinal reinforcement, enabling more accurate shear deformation measurement. However, the current study of shear behavior is applicable only for the cases, in which axial loading is not a significant concern (e.g. bridge columns). Two groups of RC beams were prepared (see Table 3.1):

(1) Group 1 included a reference RC beam (SP1) and five RC beams fully wrapped with different amounts of FRP composites (SP2 to SP6), all with identical longitudinal and transverse steel reinforcement as the reference beam but different strengthening ratios of FRP. Each specimen had a cross section of 250 mm × 270 mm, whose corners were chamfered with a radius of 11 mm to prevent stress concentration, and the shear span was 600 mm, resulting in a shear-span to effective-depth ratio of 2.50. The longitudinal reinforcement and transverse steel reinforcement ratios were 2.53% and 0.17%, respectively, in all the six specimens, whereas the volumetric ratio (i.e., calculated based on the nominal thickness of the LRS FRP sheets) of the wrapped LRS FRP composites varied from 0.11 % to 0.45%.

(2) Group 2 included four RC beams (SP7 to SP10) that had different sectional dimensions and shear-span to effective-depth ratios to the reference beam. This group was designed to investigate the effects of the longitudinal reinforcement ratio and shear-span to effective-depth ratio. SP7, representing a deep

beam with dimensions 250 mm (width) × 500 mm (height) and a shear span of 1125 mm (see Table 1), whereas SP8 and SP9 had dimensions of 250 mm (width) × 270 mm (height) and a shear span length of 600 mm. SP10, representing a small section of beam, had dimensions 100 mm (width) × 150 (height) mm and a shear span of 300 mm. The specimen corners were chamfered with a radius of 11 mm. SP7 and SP9 were designed to have a similar shear strengthening ratio and shear-span to effective-depth ratio as SP5, whereas the longitudinal reinforcement ratio was made different. SP8 had a similar shear strengthening and longitudinal reinforcement ratio as SP3, whereas the shear-span to effective-depth ratio was made different. SP10 had a large spacing of transverse reinforcement significantly less than that required in the JSCE-2007 specification.

For all strengthened specimens (SP2 to SP10), a continuous fiber sheet with the main fibers oriented in the transverse direction was fully wrapped around the RC beam with an overlapping zone of length 250 designed to span the top side (subject to compression) of the specimens for firm anchorage.

### 3.2.2. Materials

#### 3.2.2.1. Concrete and steel reinforcement

Two groups of specimens were cast with two batches of ready-mixed concrete with a maximum 20 mm size of aggregate. At the time of testing, the cylinder concrete strengths of the first and second batches of concrete were 25.3 MPa and 32.6 MPa, respectively. The longitudinal steel reinforcement and transverse steel reinforcement were tested to find their tensile stress-strain relationship. The longitudinal reinforcement used in Groups 1 and 2 specimens had a 25 mm diameter with yield strengths of 382 MPa, and 539 MPa, respectively, except in SP10 for which a 13 mm diameter of compression reinforcement was used with a yield strength of 360 MPa (see Tables 3.1 and 3.2). In specimens SP1 to SP9, the transverse reinforcement had a 6 mm diameter and a 350 MPa yield strength, whereas for SP10 the transverse reinforcement had a 13 mm diameter and the same yield strength.

**Table 3.2** Material properties of steel reinforcement

Item	Diameter (mm)	Sectional area (mm <sup>2</sup> )	Yielding strength (MPa)	Young's modulus (MPa)	Yielding strain (µε)
<b>Longitudinal reinforcement</b>					
D25 (SD345)	25	506.7	382	188,000	2,000
D25 (SD490)	25	506.7	539	198,000	2,700
D13 (SD360)	13	126.7	360	180,000	2,000
<b>Transverse Reinforcement</b>					
D13	13	126.7	360	180,000	2,000
D6	6	31.67	350	196,000	1,800

**Ultimate Shear behavior and Modeling of Reinforced Concrete Members Jacketed by FRP and Steel**

**Table 3.1** Details of test specimens

Items	Specimen										
	unit	SP1	SP2	SP3	SP4	SP5	SP6	SP7	SP8	SP9	SP10
$f'_c$	MPa	25.3	25.3	25.3	25.3	25.3	25.3	32.6	32.6	32.6	32.6
$b$	mm	250	250	250	250	250	250	250	250	250	100
$h$	mm	270	270	270	270	270	270	500	270	270	150
$d$	mm	240	240	240	240	240	240	450	240	240	120
$a$	mm	600	600	600	600	600	600	1125	750	600	300
$a/d$	-	2.50	2.50	2.50	2.50	2.50	2.50	2.50	3.13	2.50	2.50
Longitudinal reinforcement in compression		←————— 3D25 (SD345) —————→				—————→ 5D25 (SD345)			3D25 (SD345)	3D25 (SD345)	2D13 (SD360)
Longitudinal reinforcement in tension		←————— 5D25 (SD345) —————→				—————→ 10D25 (SD490)			5D25 (SD490)	4D25 (SD490)	1D25 (SD490)
Transverse reinforcement		D6	D6	D6	D6	D6	D6	D6	D6	D6	D13
$\rho_{sc}$	%	2.53	2.53	2.53	2.53	2.53	2.53	2.30	2.50	2.50	2.10
$\rho_{st}$	%	4.22	4.22	4.22	4.22	4.22	4.22	4.50	4.22	3.38	4.22
$\rho_w$	%	0.17	0.17	0.17	0.17	0.17	0.17	0.17	0.17	0.17	0.25
$\rho_f$	%	0.00	0.11	0.17	0.22	0.34	0.45	0.34	0.17	0.34	0.19
$s$	mm	150	150	150	150	150	150	150	150	150	250
$t_f$	mm	0	0.28	0.42	0.56	0.84	1.12	0.84	0.42	0.84	0.18
$A_w$	mm <sup>2</sup>	63.34	63.34	63.34	63.34	63.34	63.34	63.34	63.34	63.34	253.40
$E_f$	GPa	0	9.58	9.58	9.58	9.58	9.58	9.58	9.58	9.58	9.58
$E_w$	GPa	196	196	196	196	196	196	196	196	196	196
$E_f t_f$	KN/mm	0.00	0.34	4.02	5.36	8.05	10.73	8.05	4.02	8.05	1.72
$E_w A_w / s$	KN/mm	82.76	82.76	82.76	82.76	82.76	82.76	82.76	82.76	82.76	198.67
$E_f t_f / (E_w A_w / s)$	-	-	0.03	0.05	0.06	0.10	0.13	0.10	0.05	0.10	0.01

$f'_c$  = compressive strength of concrete cylinder;  $b$  = width of beam cross-section;  $h$  = total depth of beam cross-section;  $d$  = effective depth of beam cross-section;  $a$  = shear span;  $a/d$  = shear-span to effective-depth ratio;  $\rho_{sc}$  = ratio of compression reinforcement;  $\rho_{st}$  = ratio of tension reinforcement;  $\rho_w$  = ratio of transverse steel reinforcement;  $\rho_f$  = volumetric ratio of FRP sheet;  $s$  = spacing of transverse steel reinforcement;  $t_f$  = total nominal thickness of FRP sheet for both shear sides;  $A_w$  = total cross-sectional area of both legs for one single transverse steel reinforcement;  $E_f$ ,  $E_w$  = Young's modulus of FRP sheet, and Young's modulus of transverse steel reinforcement.

3.2.2.2. PET sheet

Polyethylene terephthalate (PET) dry fiber sheets (PET-600) were used in the experiments to form LRS FRP composites. Flat coupon tests for PET FRP composites were conducted to determine their tensile properties following the JSCE standard E541-2000 [26]. The tensile coupons sheets had a nominal thickness of 0.841 mm, a length of 280 mm and a width of 13 mm. The coupon preparation followed the usual wet lay-up process involving the impregnation of a large area of fiber sheet with a matrix epoxy resin, which consisted of a main resin component and a hardener, with a mix ratio of 2:1 by weight. After one week of curing in the laboratory environment, the hardened large PET FRP plate was cut into many strips (i.e., testing coupons) with the required dimensions. Glass FRP (GFRP) tabs (25 mm long and 13 mm wide) were bonded to strengthen the two ends of each PET FRP coupon and to ensure uniform stress transfer from the loading heads during the tensile tests, which were performed at a constant loading rate equivalent to 1% strain per minute. An image measurement method [24,50] was used to capture the tensile strain of each PET flat coupon with a gauge length of 45 mm (Fig. 3.1a). The tensile stress in the PET FRP composite was calculated from the tensile load on the basis of the nominal area of the fiber sheet. All six coupons were tested and found to fail in the central region of the specimens. Fig. 1b shows the obtained tensile stress-strain relationships. The PET FRP sheets exhibit a bilinear stress-strain behavior caused by the motion of amorphous phases and by the sliding or failing of macromolecular chains in PET and PET fibers [14,33]. During the initial deformation, the amorphous regions within the microfibrils align themselves with a similar orientation to that in the mesamorphous phase. The stress-strain curve moves to the transition point that occurs when the applied load starts to strain the bonds in both the amorphous and crystalline phases. Table 3.3 presents a summary of the material properties of PET FRP sheets provided by the manufacturer and obtained from the present tensile tests. Two different values of elastic modulus, namely the initial elastic modulus ( $E_1$ ) for the first linear portion of the stress-strain relationship and the second-stage elastic modulus ( $E_2$ ) for the second linear part are given in the table, together with the strain value at the transition point ( $\epsilon_0$ ) between the two linear portions.

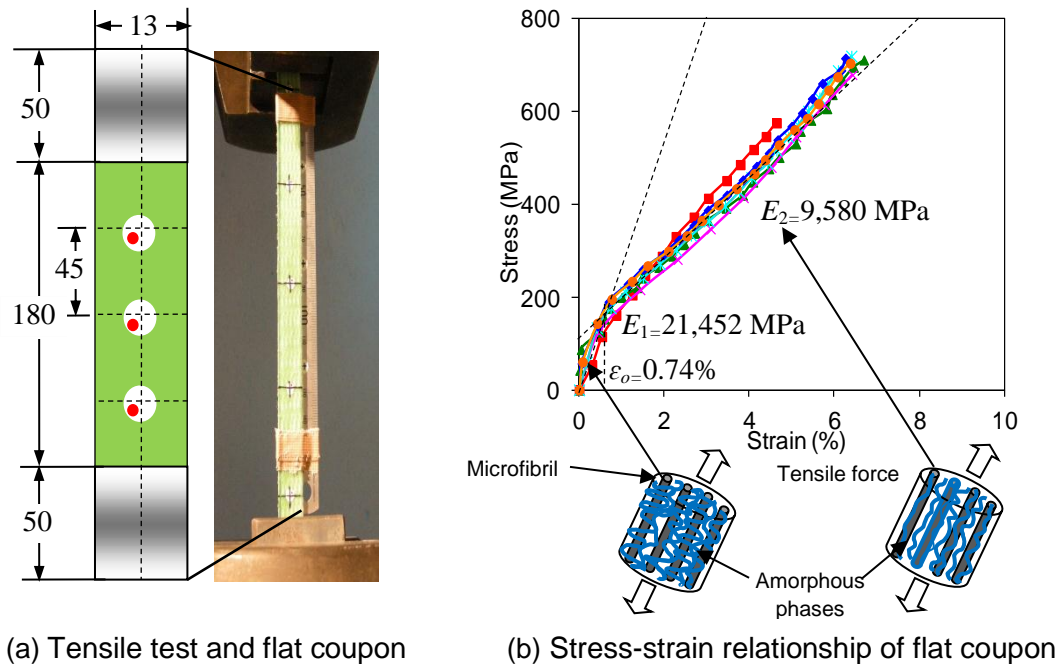


Fig. 3.1 Tensile test of flat coupon:

Table 3.3 Material properties of PET FRP sheets

Product	Manufacturer data				Present tensile tests					
	Nominal thickness (mm)	Tensile strength (MPa)	Young's modulus (MPa)	Rupture strain (%)	Nominal thickness (mm)	Tensile strength (MPa)	Strain at transition, $\epsilon_o$ (%)	Rupture strain (%)	$E_1$ (MPa)	$E_2$ (MPa)
PET-600	0.841	740	10,000	6.7-8.2	2.5	704	0.74	6.43	21,452	9,580

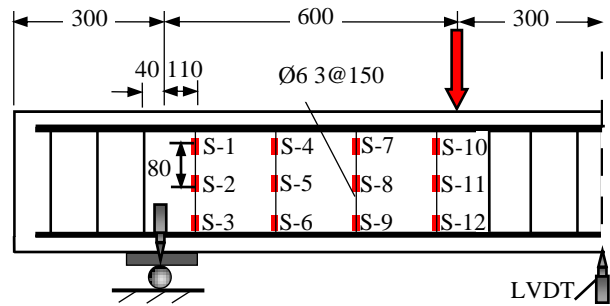
3.2.3. Test procedures and instrumentation

3.2.3.1. Loading system, strain gauges and total deformations

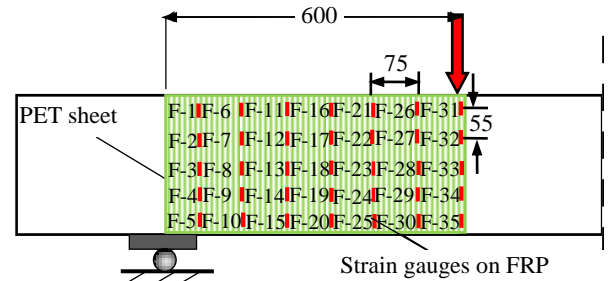
All the beam specimens were tested under four-point loads and carefully instrumented during the tests to monitor the loads, mid-span beam deflections and strains of transverse reinforcement and PET FRP composites (Fig. 3.2a). The locations of strain gauges and Linear Variable Differential Transformers (LVDTs) are illustrated in Figs. 3.2b and 3.2c. The strain gauges were located in the region where shear cracks are expected to occur. A network of strain gauges (with a gauge length of 10 mm) were mounted on all the transverse reinforcements at a spacing of 80 mm. Asymmetrical loading was applied to ensure failure to occur within this span. Strain gauges were also attached onto the PEF FRP at one beam side within the shear span. The gauge length was also 10 mm and the spacing between adjacent gauges was 55 mm. For each specimen, deformations were measured using LVDTs at two supports and at mid-span.



(a) Asymmetrical loading



(b) Locations of strain gauges on steel reinforcement

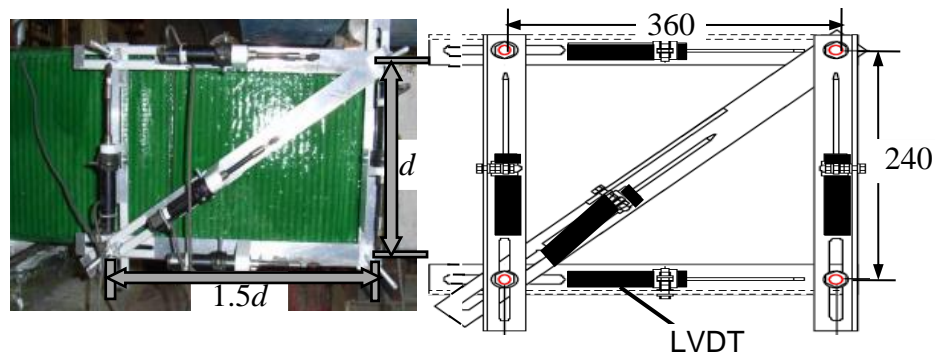


(c) Locations of strain gauges on FRP

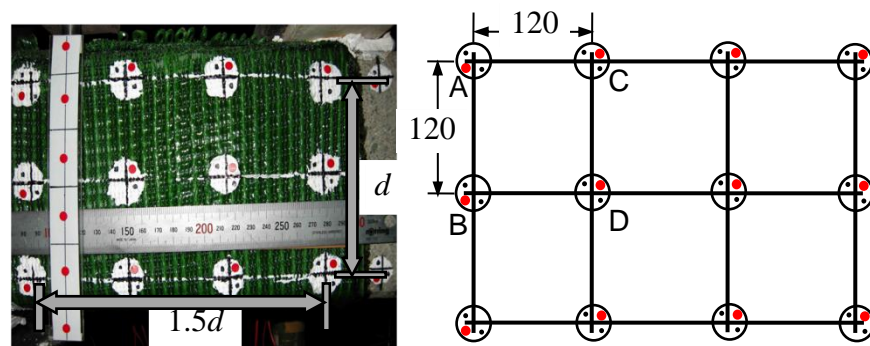
Fig. 3.2 Test setup (SP1–SP6, SP9)

### 3.2.3.2. Shear deformation devices

Various techniques have been attempted to measure the shear deformation of RC members, including the placement of LVDTs (e.g., Massone and Wallace [37]; Anggawidjaja et al. [5]), the use of potentiometric extensometers for curvature and shear strain measurements (e.g., Debernardi and Taliano [18]), and the laser speckle method (e.g., Ueda et al. [65]). Conventional LVDT-based methods were used here, as shown in Fig. 3.3a, for the measurement of shear deformation for the first batch of specimens (i.e., SP1 to SP6). However, for the second batch of specimens, the shear deformation measurement was done using a more advanced digital image correlation (DIC) method with the help of charge-coupled device (CCD) cameras (Fig. 3.3b). This method probes cracks and shear deformation of concrete surfaces with high image quality, low processing cost, and can monitor until the failure of specimens while avoiding causing specimen damage (Ito et al. [24]; Qi et al. [50]). For confirmation purposes, the conventional LVDT-based method was implemented in parallel with the DIC method for SP7, whereas only the DIC method was implemented for specimens SP8 to SP10 after its reliability was confirmed. The measurement of shear deformation focused on the plastic hinge region of the specimens, which is within  $1.5d$  from the loading point to the support location. This region is most likely to experience shear deterioration particularly during seismic loading (Anggawidjaja et al. [5]). The frame for installing the LVDTs and the grid for the calibration points in the DIC method are shown in Figs. 3.3a and 3.3b, respectively. In the DIC measurement, the measured region was divided into many square grids, each of which had four target coordinating points A, B, C and D (Fig. 3.3b). In order to produce a physical picture, the image was translated into the digital information of target coordinate using commercially available software such as Adobe Photoshop. Based upon the digital information, the shear deformation of each tested beam could be calculated.



(a) Strain deformation measurement using LVDTs in SP1–SP6



(b) Strain deformation measurement using LVDTs in SP7–SP10

**Fig. 3.3** Measurement of shear deformation

### 3.3. RESULTS AND DISCUSSION

#### 3.3.1. Failure modes and crack patterns

Figure 3.4 shows the failure modes of specimens SP1 to SP10 presenting the sketches of the failed specimens and photographs after the removal of the LRS FRP jackets. The black lines drawn on the concrete surface show the locations of cracks, and the hatched areas indicate the bulges on the concrete surface and spalling of concrete. Except SP6, which had the largest shear strengthening ratio (Table 3.1), all other specimens failed in shear with clear shear deformation (i.e., no yielding of flexural reinforcement was observed before the yielding of transverse steel reinforcement). The shear failure in the ultimate state was mainly caused by the crushing of the concrete in the compression zone at the top of the critical diagonal crack (i.e., shear compression failure). At the peak load, PET FRP composites showed no sign of rupture, except in SP10. For the reference SP1, spalling of concrete cover occurred. However, in all strengthened specimens the spalling of concrete was prevented by the FRP confinement. Instead, bulging of PET FRP composites was seen at the top of the compression region, as indicated by the hatched areas in Fig. 3.4.

The angles of major diagonal shear cracks ( $\theta_{cr}$ ) were evaluated both from visible shear cracks and from the locations of maximum strains developed in transverse steel reinforcement and PET FRP sheets at different beam sections, as shown in Fig. 3.4 using dashed lines. The values of these angles varied from  $39^\circ$  to  $53^\circ$  to the member axis. In the first group of specimens, the reference specimen (SP1) developed two major shear cracks at an angle of  $45^\circ$ . In the strengthened specimens SP2 to SP5, the angle of the major shear cracks were slightly less than  $45^\circ$  ranging  $44^\circ$  to  $39^\circ$ . As the member deformation increased further, partial debonding of the FRP occurred near the critical shear crack or at the edge of the beam (see Fig. 3.5), and a loud noise was produced owing to the bulge of the concrete in the compression region. Finally, the PET FRP composites at the corner locations ruptured, leading to concrete crushing and a complete detachment of the FRP from the concrete substrate (Fig. 3.5). SP6, with a 0.45% volumetric ratio of FRP, showed no major shear deformation (Fig. 3.4) because of a confinement effect.

SP8 in the second group with a relatively high shear-span to effective-depth ratio ( $a/d = 3.13$ ) exhibited a crack angle of  $49^\circ$  in the plastic hinge area. In SP7, whose ratio of shear reinforcement spacing to beam depth is smaller than the others, showed the largest crack angle ( $\theta_{cr} = 53^\circ$ ) among all the specimens. In SP10, PET FRP sheets ruptured at the moment when the diagonal shear crack penetrated to the compression zone of concrete, and the major shear crack did not pass any transverse steel reinforcement because of their large spacing (i.e.,  $s = 250$  mm); the PET FRP sheets ruptured at the shear crack locations rather than the corners of the beam section owing to the significant shear stress transferred from the concrete to the FRP, leading to a diagonal tension failure of the member. This is an example of a poor truss mechanism by which the shear stresses were not transferred through the truss nodes, leading to member collapse in a very brittle behavior.

Overall, apart from the case when the transverse steel reinforcement ratio is extremely low, PET FRP composites prevented crack opening in the strengthened beams that leads to multiple shear cracks in the shear critical zones. Fig. 3.5 shows the locations where the PET FRP sheets ruptured, indicating that the breakage of PET FRP sheets usually started from the corner of the beam section near to the loading plate (e.g., in SP4). In addition, the rupture of PET FRP sheets was observed mostly at a large shear deformation level.

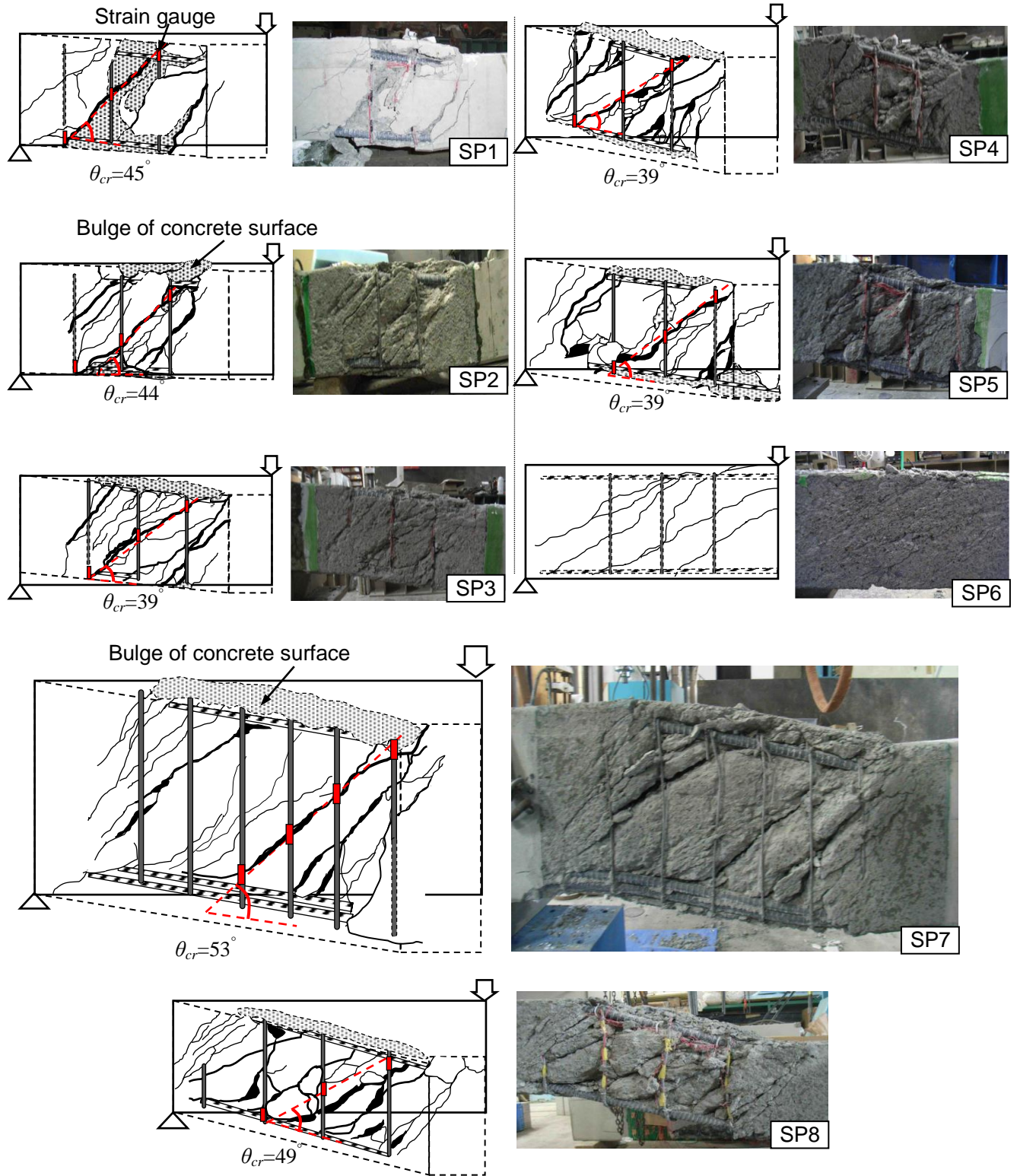


Fig. 3.4 Failure modes and crack patterns

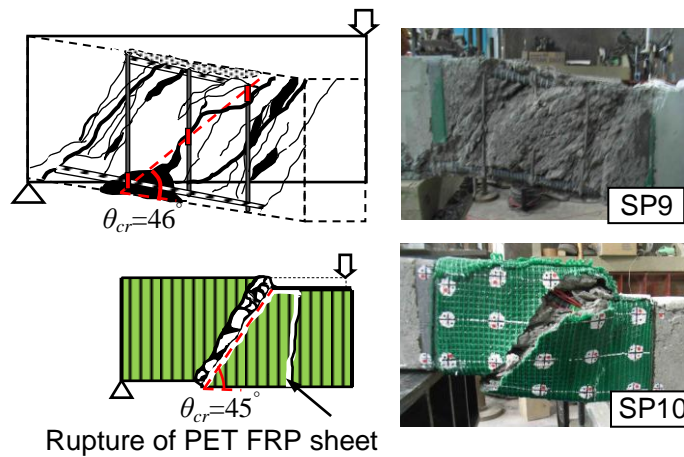


Fig. 3.4 Failure modes and crack patterns (Continued)

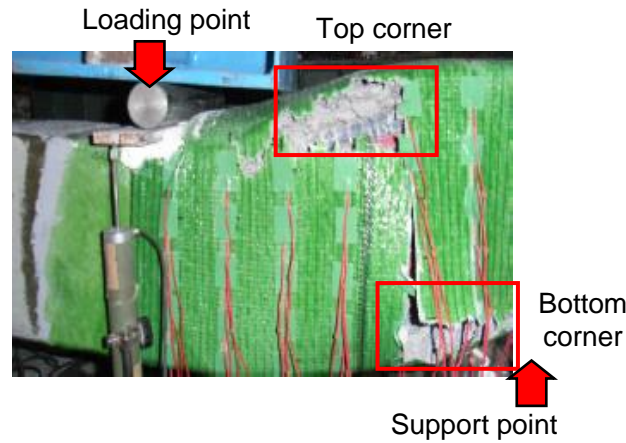


Fig. 3.5 Rupture and debonding location in PET sheet at termination of test in SP4

### 3.3.2. Overall load-deformation responses

The overall shear force vs. mid-span deflection responses of specimens SP1 to SP6 and SP7 to SP10 are presented in Figs. 3.6a and 3.6b, respectively; the shear force ( $V_i$ ) is presented using a nominal shear stress ( $v_i$ ) by dividing the shear force by the effective cross section (i.e.,  $v_i = V_i/bd$ ). The mid-span deflection is presented by the drift ratio ( $\delta$ ), which is defined as the ratio of the mid-span deflection ( $\Delta_{total}$ ) to the shear span ( $a$ ).

The reference specimen (SP1) showed a linearly increasing portion until the peak load and a sudden drop of the load-carrying capacity afterwards, indicating a typical brittle shear failure of the member. During the tests of specimens SP2 to SP5 the evolution of the member's mid-span deflection was terminated at the rupture of PET FRP sheets. The corners in SP5 were not well rounded, resulting in the premature rupture of FRP at a corner, and subsequently a lower ultimate ductility was achieved compared to SP4. For SP6, which failed in flexure, neither FRP rupture nor the decrease in shear capacity was observed even at the drift ratio of 12%, at which point the test was stopped owing to the extremely large deformation. It is interesting that specimens SP2 to SP5 also exhibited significant ductility although they

failed in shear. The nominal shear stress achieved in the peak of the linear portion of the load-deflection response increased with the amount of PET fiber sheets, as did the drift ratio. This is because that, with increasing strengthening ratio, the confinement provided by LRS FRP not only prevented concrete from spalling off but also restrained the widening of shear cracks. The considerable ductility development before the member's shear failure seems to be a unique characteristic of PET FRP-strengthened RC members. In other words, the shear failure is no longer brittle.

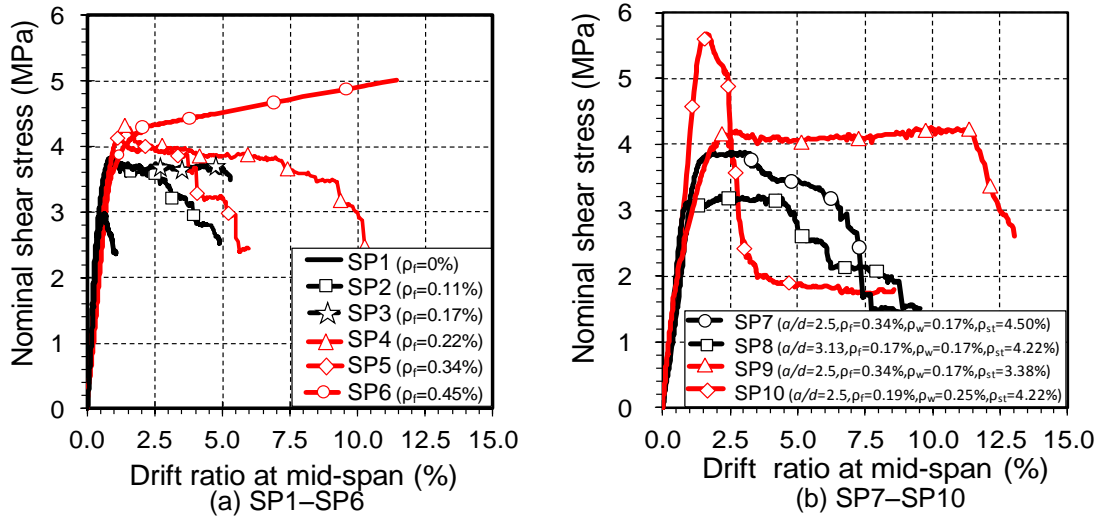


**Fig. 3.6** Relationships between nominal shear stress ( $v$ ) and drift ratio at mid-span ( $\delta$ )

In the second group, SP10 was subjected to a brittle shear failure, and exhibited a load-deflection response similar to that of the reference SP1. The nominal shear strength of SP10 was the highest among all the specimens mainly because it had the smallest sectional dimensions (Fig. 3.6b). SP7 to SP9 exhibited ductile shear failure (Fig. 3.6b). SP7 and SP9 had similar shear-span to effective-depth ratio and strengthening ratio as SP5. The difference between these three specimens was their longitudinal reinforcement ratios; SP9, which had the lowest value, achieved the highest shear ductility, as shown in Fig. 3.6b, because of its highest shear to flexural strength ratio. SP7 exhibited the smallest ductility owing to its higher longitudinal reinforcement ratio, as shown in Fig. 3.6b. The largest sectional dimensions of SP7 may also be the reason for its lower shear ductility, because concrete degradation may be faster in the case of large-depth RC beams owing to the widening of concrete cracks in the web. This is also witnessed by the observed crack patterns (Fig. 3.4). SP8 had the same longitudinal reinforcement ratio and shear strengthening ratio as SP3, whereas their shear-span to effective-depth ratios were different. Both two specimens maintained a constant nominal shear stress until the drift ratio of approximately 5% (Figs. 3.6a and 3.6b). However, SP8 showed more ductility compared to SP3 because the former had a larger shear-span to effective-depth ratio than the latter (Figs. 3.6a and 3.6b).

Table 3.4 presents a comparison between the tested shear strengths and the predicted ones based upon existing design codes. The shear strengths are compared in terms of three components, which are from concrete ( $v_c$ ), transverse steel reinforcement ( $v_s$ ) and LRS FRP sheet ( $v_f$ ). Each component is computed based on the existing design equations in the JSCE codes, JSCE 2001; JSCE 2007 [25,27] (see Appendix A). For the test values, the shear stresses carried by the transverse steel reinforcement ( $v_{s-test}$ ) and LRS FRP ( $v_{f-test}$ ) are obtained from their measured strain values, and then the shear contribution of concrete ( $v_c$ ).

## Ultimate Shear behavior and Modeling of Reinforced Concrete Members Jacketed by FRP and Steel

$v_{test}$ ) can be obtained. The estimations of the contributions of the transverse steel reinforcement and LRS FRP also depend on the shear crack angle ( $\theta_{cr}$ ) of each specimen, which is also summarized in Table 3.4. The approaches by which the strain values of transverse steel reinforcement and LRS FRP were chosen for calculation will be elaborated later. It is seen in Table 3.4 that generally the shear contribution of concrete is underestimated while the shear contribution of LRS FRP composites is overestimated. The underestimation of the concrete shear contribution is due to the conservative nature of the design equations, whereas the overestimation of the FRP contribution arises because the design equation was derived from the experimental data of carbon and Aramid FRPs which often show the rupture of FRP at the peak load.

**Table 3.4** Summary of test results in shear-stress and drift-ratio component

Items	unit	Specimen										
		SP1	SP2	SP3	SP4	SP5	SP6	SP7	SP8	SP9	SP10	
Calculation at $\lambda$	$v_c$	MPa	1.78	1.78	1.78	1.78	1.78	1.78	1.69	1.77	1.79	2.30
	$v_s$	MPa	1.48	1.48	1.48	1.48	1.48	1.48	1.58	1.85	1.48	1.85
	$v_f$	MPa	-	0.27	0.41	0.55	0.82	1.10	0.82	0.41	0.82	0.44
	$v_t$	MPa	3.26	3.53	3.67	3.80	4.08	4.35	4.09	4.03	4.09	4.59
	$v_{mu}$	MPa	5.58	5.58	5.58	5.58	5.58	5.58	5.94	5.75	6.25	6.11
	$v_f/v_{mu}$	-	0.58	0.63	0.66	0.68	0.73	0.78	0.69	0.70	0.65	0.75
Test at $\delta_p$	$v_{c-test}$	MPa	1.86	2.59	2.25	2.78	2.45	2.30	1.05	0.75	1.35	4.40
	$v_{s-test}$	MPa	1.12	1.06	1.11	1.11	1.11	1.14	1.11	1.19	1.19	0.99
	$v_{f-test}$	MPa	-	0.23	0.46	0.44	0.62	1.00	1.73	1.29	1.72	0.28
	$v_{t-test}$	MPa	2.97	3.87	3.82	4.33	4.14	4.43	3.89	3.22	4.26	5.68
	$\delta_p$	%	0.66	0.95	0.80	1.39	1.14	11.44	2.61	4.28	9.96	1.64
	$\delta_{sp}$	%	0.48	0.23	0.16	0.42	0.22	0.91	2.35	2.70	6.13	0.62
	$\delta_{sp}/\delta_p$	-	0.73	0.24	0.20	0.30	0.19	0.08	0.90	0.63	0.62	0.38
Test at $\delta_u^*$	$v_{c-test}$	MPa	1.33	1.60	-	0.34	1.49	-	0.48	0.47	0.45	2.90
	$v_{s-test}$	MPa	1.05	1.17	-	1.22	1.08	-	1.14	1.19	1.19	1.18
	$v_{f-test}$	MPa	-	0.32	-	1.91	0.73	-	1.41	0.08	1.78	0.23
	$v_{t-test}$	MPa	2.38	3.10	-	3.46	3.30	-	3.03	2.58	3.42	4.31
	$\delta_u$	%	0.96	3.76	-	8.46	4.06	-	6.60	5.28	12.06	2.49
At the end of test	$v_{c-test}$	MPa	1.25	1.30	1.17	0.00	0.99	2.30	0.12	0.35	0.00	0.00
	$v_{s-test}$	MPa	1.11	1.11	1.17	1.22	1.08	1.14	1.13	0.80	1.19	1.88
	$v_{f-test}$	MPa	0.00	0.13	1.15	0.80	0.38	1.00	0.21	0.29	1.55	0.22
	$v_{t-test}$	MPa	2.37	2.54	3.49	2.01	2.45	4.43	1.46	1.44	2.61	1.79
	$\delta_{end}$	%	1.07	4.89	5.27	11.42	6.0	11.44	8.84	9.53	13.05	8.59
<b>Failure mode</b>	-	Shear. comp	Flexure	Diag. tens								

\*The ultimate state ( $\delta_u$ ) is defined to be reached with the load dropped by 20% compared to its peak load; Shear. comp = Shear compression failure; Diag. tens = Diagonal tension failure.

### 3.3.3. Evaluation of shear deformation

The shear deformation of tested beams was calculated based on Massone and Wallace's (2004) method [37]. As shown in Fig. 3.7, the undeformed rectangular shape is represented by a truss element enclosed by dashed lines, whereas the deformed shape due to pure shear deformation is represented by the shaded area.

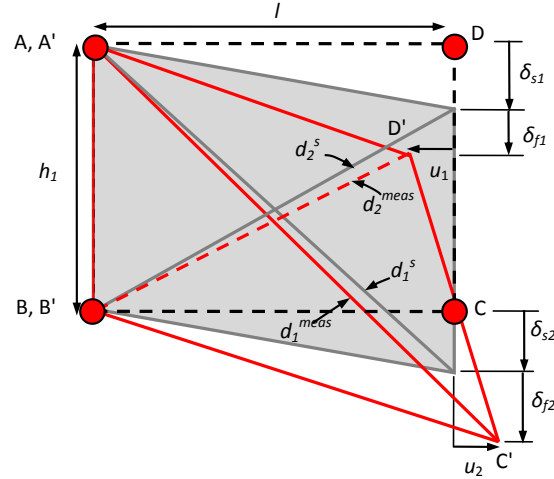


**Fig. 3.7** Deformed configuration (Massone and Wallace 2004) [37]

The total deformation corresponding to the combined flexural and shear deformations is illustrated by the solid lines. In case of shear deformation without flexural effect, the center of rotation is located at the centroid of the truss unit. The average shear deformation ( $\delta_s$ ) for a specific coordinate of the concerned truss can be obtained as follows:

$$\delta_s = \frac{\sqrt{|d_1^{meas}|^2 - |l + u_2|^2} - \sqrt{|d_2^{meas}|^2 - |l + u_1|^2}}{2} - \delta_f \quad (3.1)$$

where  $d_1^{meas}$  and  $d_2^{meas}$  are the measured diagonal lengths of the deformed truss due to combined shear and flexural actions;  $u_1$  and  $u_2$  are the horizontal displacements at the top and bottom of the truss unit, respectively; and  $l$  is length of the truss unit.

The contribution of the flexural deformation ( $\delta_f$ ) can be attributed to the rotation of tension and compression chords, BC and AD, respectively (Fig. 3.7). In this study, the vertical displacements due to flexure action i.e.,  $\delta_{f1} = \delta_{f2} = \delta_f$  is assumed to be identical for each beam cross section and can be calculated as follows:

$$\delta_f = \alpha l \frac{u_1 - u_2}{h_1} \quad (3.2)$$

where:  $\alpha$  is value describing the distance from the top of the section to the centroid of the sectional curvature distribution, and is taken as 0.5, assuming that the center of rotation is at the mid-height of the truss element;  $h_1$  is the height of the truss unit, and  $l$  is the length of the truss unit. All the parameters used in Eqs. (1) and (2) are illustrated in Fig. 3.7. The values of  $d_1^{meas}$ ,  $d_2^{meas}$ ,  $u_1$  and  $u_2$  were obtained from the LVDT and DIC-based measurement methods (Figs. 3.3a and 3.3b). Shear deformation contributed to total deformation at peak load ( $\delta_{sp}/\delta_p$ ) is also summarized in Table 3.4.

Figure 3.8 shows the relationships between the nominal shear stress ( $v_t$ ) and the drift ratio due to shear deformation at the mid-span ( $\delta_s$ ). In the first group of specimens, SP1 shows a small value of shear drift ratio at the ultimate state. In addition, at the same loading level, its shear deformation is larger than that of other specimens, because the shear crack propagated rapidly in this reference specimen. For strengthened specimens, the shear drift ratio at the ultimate state increases significantly because PET FRP sheets restrained the widening of shear cracks, shifting the member from brittle diagonal tension failure to shear compression failure. SP6 failing in flexure shows the smallest shear drift ratio because no significant shear crack widening occurred. Therefore, the major deformation was contributed by the flexural effect. In the second group of specimens, SP7 with the greatest depth shows a significant increase in the shear deformation. SP10 failed in a very brittle manner, since all shear stresses due to concrete crack opening were transferred to FRP sheets, leading to the rupture of FRP followed by the sudden loss of the shear load-carrying capacity. The strain development in FRP sheet and transverse steel reinforcement will be reported in the next session.

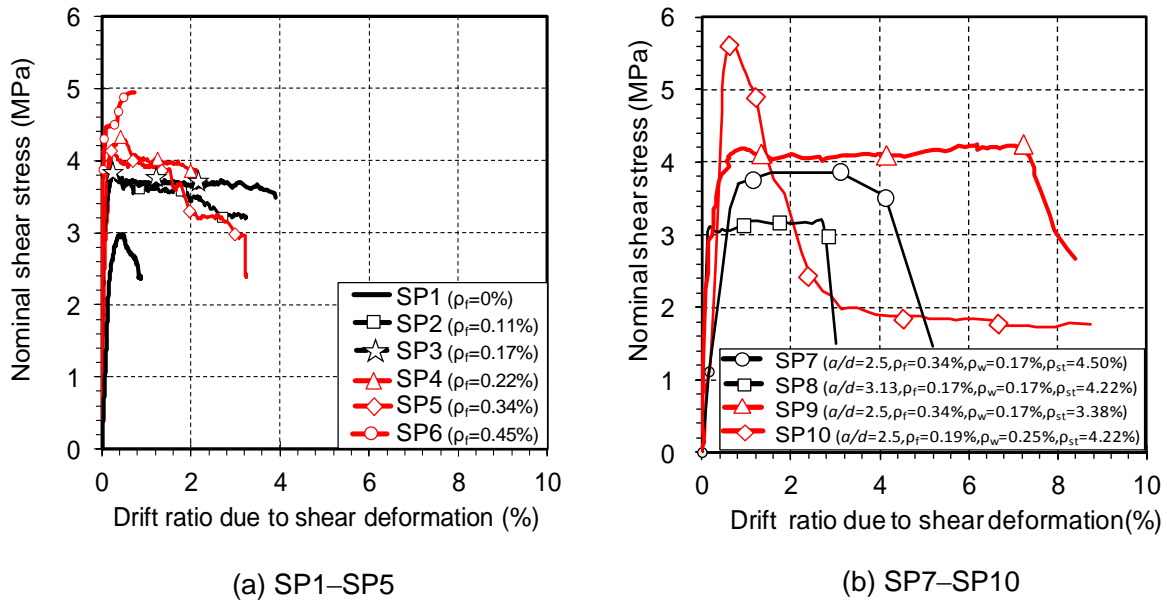


Fig. 3.8 Relationships between nominal shear stress ( $v_t$ ) and drift ratio due to shear deformation at mid-span ( $\delta_s$ )

### 3.3.4. Strain development in PET FRP sheets and transverse steel reinforcement

The strains in PET FRP sheets at the shear sides of the beams in fact were induced by two types of action: (1) opening of shear cracks in concrete due to shear action, and (2) the lateral expansion of concrete in the beam section due to flexure. It is difficult to differentiate these two effects through experimental measurement. Taking SP2 as an example, Fig. 3.9 presents the typical strain distributions in PET FRP sheets along the shear span (Fig. 3.9a) as well as along the beam height (Fig. 3.9b) at the peak load. For each measured section (i.e., represented by a strip in Fig. 3.9) along the shear span, there is a maximum strain observed in the FRP sheets (Fig. 3.9b). Most of these maximum strains were observed around a major diagonal shear crack (see the dashed line in Fig. 3.9a) in the shear-critical region of the member. However, some of them deviated somewhat from the dashed lines probably due to the existence of multi-shear cracks. The high strains at the top corner of the section near the loading plate, due to the bulging of concrete, result in a dilatation of the FRP sheets in the outward direction (see Figs. 3.4 and 3.9b).

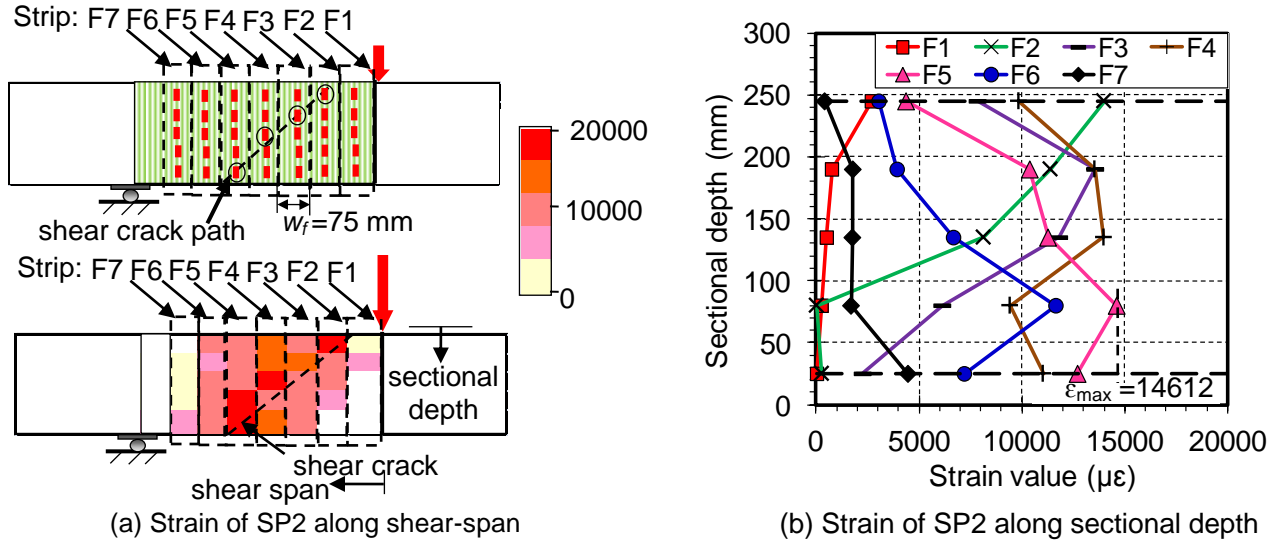


Fig. 3.9 Strain distribution of PET FRP sheet along the shear-span length at peak load

Figure 3.10 shows the strain distributions in transverse steel reinforcement along the shear span and the sectional depth. The strain distributions of transverse steel reinforcement in the shear-critical region are similar to those of PET FRP sheets. However, the maximum strains are always observed at the mid-height of the shear side of the beam (Fig. 3.10a) rather than the top corner because there is negligible effect of the concrete bulging on the transverse steel reinforcement.

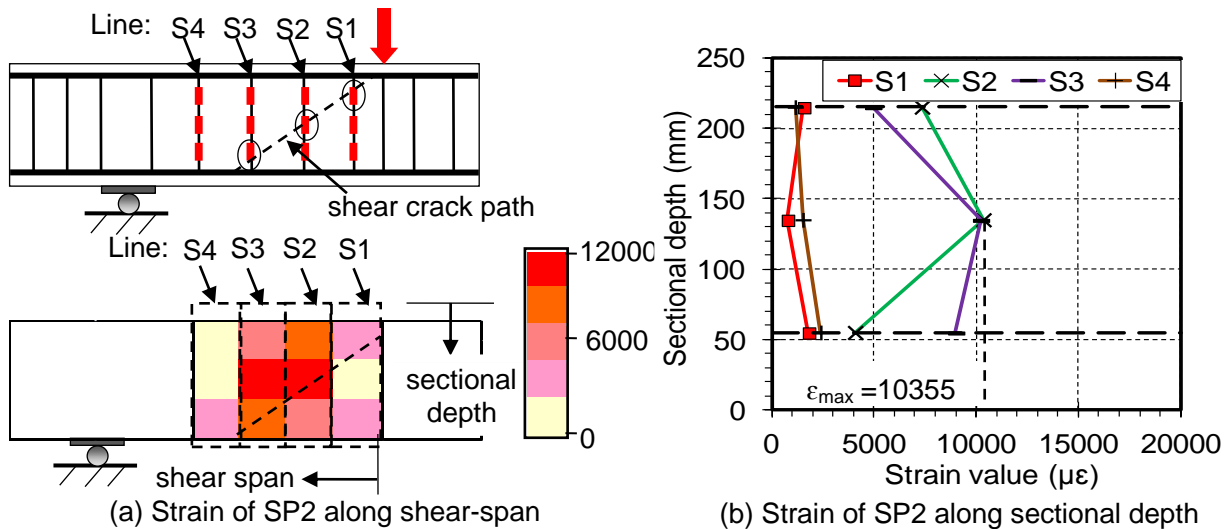
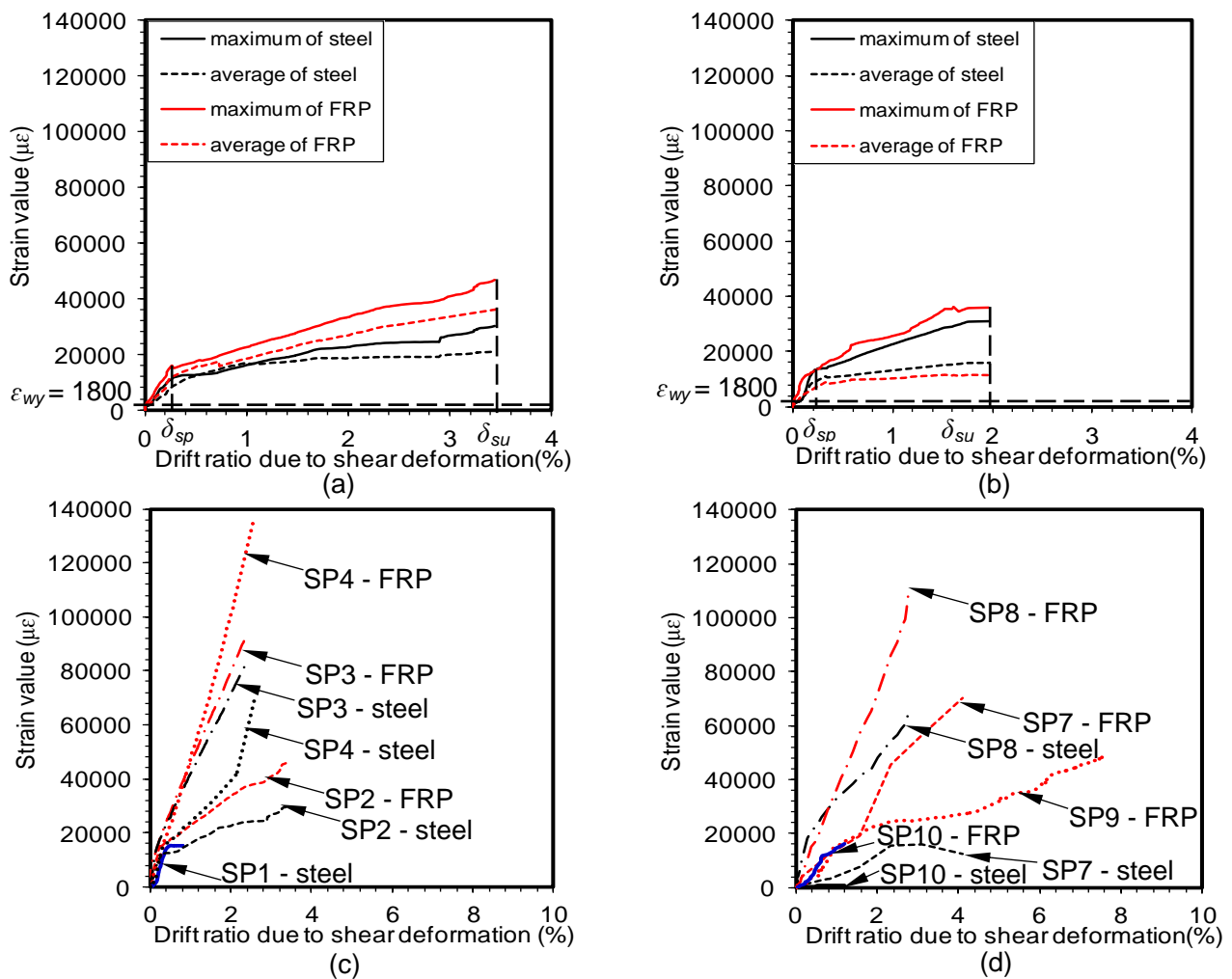


Fig. 3.10 Strain distribution of transverse steel reinforcement s along the shear-span length at peak load

The locations of strain gauges bonded on FRP sheets and transverse steel reinforcement intersected with the critical shear crack are also shown in Figs. 3.9 and 3.10. The readings of the strain gauges at these locations (i.e., marked with circles in strips F2 to F5 in Fig. 3.9, and in lines S1 to S3 in Fig. 3.10) were

recorded to calculate the shear stress contribution from FRP sheets ( $v_{f-test}$ ) and the transverse steel reinforcement ( $v_{s-test}$ ), which represent integrals of the tensile force along each strip/line.

Figure 3.11 shows the typical development of the strains in transverse steel reinforcement and PET FRP sheets with the shear deformation, which is also represented by the drift ratio, until the members' ultimate states. The locations where the maximum strains in both transverse steel reinforcement and PET FRP sheets in all the specimens are summarized in Figs. 2b, 2c and 2d. The average strains of transverse steel reinforcement and PET FRP sheets are the average values of all strain readings on the strip on which the maximum value was observed. In all the strengthened beams, the transverse steel reinforcement and PET FRP sheets tended to have similar maximum strain values before the yielding of the transverse steel reinforcement. An approximately linear increase of the maximum and average strains with the shear deformation was seen during this period. Beyond this the strain increase in transverse steel reinforcement and PET FRP sheets behaved nonlinearly. The rate of strain increase in FRP sheets and transverse steel reinforcement first increased due to the stiffness degradation of the transverse steel reinforcement and then decreased after the peak load ( $\delta_{sp}$ ). In the reference specimen, the increase in strain of transverse reinforcement was, however, nearly constant after the peak load because the ultimate state was reached shortly after the shear crack propagation. The strain increase in LRS FRP sheets was usually larger than



**Fig. 3.11** Strain development of PET FRP

that in transverse steel reinforcement because of the dual effects of LRS FRP sheets (i.e., shear strengthening and confinement effects).

The difference between the average strain and the maximum strain of FRP sheets reflects the extent of strain localization. It is seen that such a difference was smaller in SP2 (Fig. 3.11a) than that in SP5 (Fig. 3.11b). This is mainly because the location of the maximum strain observed in SP2 was closer to the major shear crack (F-18 in Fig. 3.2) while that observed in SP5 was closer to the top corner of the section. The stress concentrations at the former and latter locations tended to lead to easy debonding and fiber rupture, respectively.

Figs. 3.11c and 3.11d show the development of the maximum strain in FRP sheets and transverse steel reinforcement with the shear deformation for Group 1 and Group 2 beams, respectively. For the first group, just SP1 to SP4 are presented due to the premature failure of SP5 and the different failure mode of SP6. It is seen that the strengthening ratio influenced significantly the strain development in both FRP sheets and transverse steel reinforcement. Given the same drift ratio due to shear deformation, the higher strengthening ratio of LRS FRP sheets was used, the higher strain values developed in both the FRP sheets and the transverse steel reinforcement. For the second group of specimens, SP7 with the highest longitudinal reinforcement ratio developed higher strain values in the FRP sheets with the shear deformation compared to SP9, which had the lowest longitudinal reinforcement ratio. Strains of transverse steel reinforcement in SP9 were not available due to the breakage of gauges. Compared to all other specimens in Group 2, SP8 exhibited the faster strain development in the FRP sheets with the deflection increase during the whole loading period owing to its largest shear-span-to-effective depth ratio ( $a/d = 3.13$ ).

### 3.3.5. Degradation of the shear contribution of concrete

The contribution of concrete to the shear resistance can be isolated from the total member shear force once the shear contributions of transverse steel reinforcement and LRS FRP sheets are known from the analyses on strain readings. The shear contribution of concrete in RC members wrapped with LRS FRP sheets was usually found to have reached its peak value before the full development of the member shear strength, as shown in Fig. 3.12. For example, in SP7 the concrete contribution to shear started degrading at the shear drift ratio of 0.80% while had degraded by 47.6% compared to its peak value at the shear drift ratio of 2.35% (Fig. 3.12a). A similar phenomenon was observed in all other strengthened members such as in SP10 (Fig. 3.12b). The extent of degradation varied from a range of 0~54.6% depending on the volumetric ratio of FRP sheets, the shear-span to effective-depth ratio and the depth of member section. Therefore, the prediction of the degradation of concrete shear contribution is essential for RC members strengthened by LRS FRP composites.

Figure 3.13 shows the relationships between the concrete shear stress ( $v_c$ ) and the member drift ratio due to shear deformation ( $\delta_s$ ). In the first group of specimens, the maximum shear contributions from concrete are different for different specimens in spite of their identical sectional dimensions because the fully wrapped FRP sheets provided confinement to concrete and hence enhanced its compressive concrete strength, as shown in Fig. 3.13a and Table 3.4 ( $v_{c-test}$  at peak load). In addition, the mark “x” in Figs. 3.13a and 3.13b indicates the shear drift ratio levels at which the member's shear strength was reached in SP4, SP7 to SP10 as examples. These levels (i.e.,  $\delta_{sp}$ ) for all other specimens can be found in Table 3.4. In the second group of specimens, the degradation of the concrete shear contribution in SP8, which had a higher shear-span to effective-depth ratio, started earlier than that in other specimens, indicating that the shear-span to effective-depth ratio influenced the initiation of concrete degradation. In SP10, the concrete shear degradation suddenly lost after the peak due to insufficient transverse reinforcement.

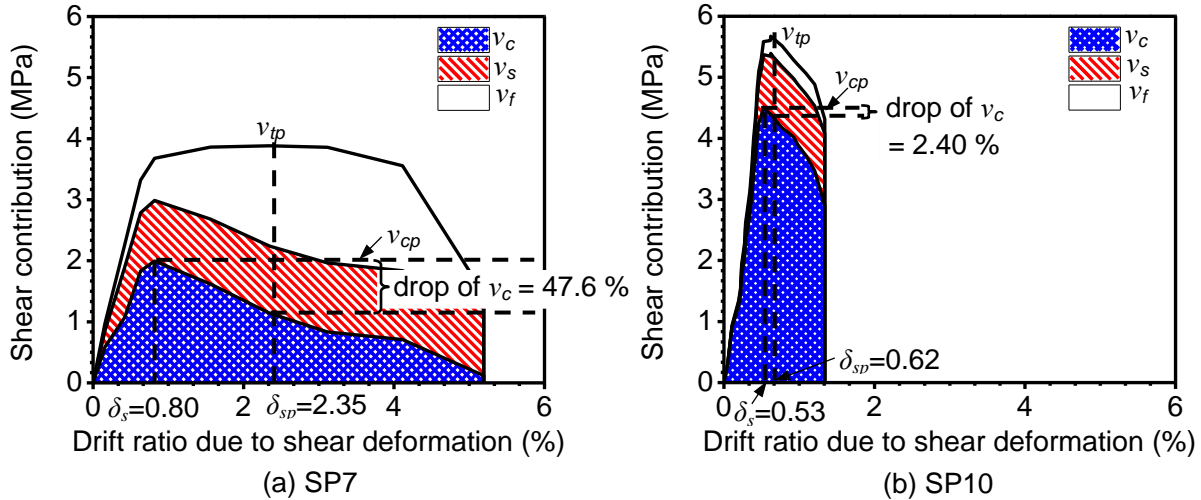
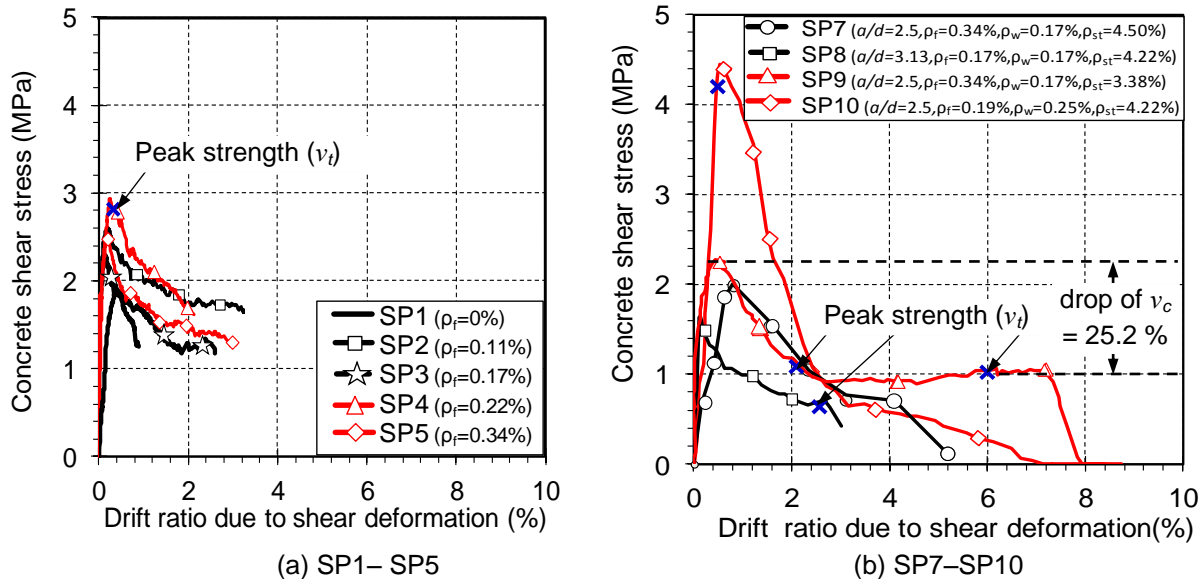


Fig. 3.12 Component of shear contribution


 Fig. 3.13 Relationships between concrete shear stress ( $v_c$ ) and drift ratio due to shear deformation at mid-span ( $\delta_s$ )

The shear contribution of concrete in an RC beam depends on the stiffness of both longitudinal and transverse reinforcement (Sato et al. 1997) [52]. When the yielding of longitudinal reinforcement in tension region takes place the stiffness of this reinforcement starts to reduce, leading to the decrease of the potential shear strength of the RC beam. The yielding of longitudinal reinforcement is followed by the uplifting of the neutral axis, which limits the contribution of concrete in the compression zone. The change of neutral axis also increases the compression strain that accelerates the softening or crushing of concrete. Similarly, the yielding of transverse reinforcement also leads to its stiffness reduction and no further increase in its contribution to the member shear strength. Therefore, it is highly possible that to predict the degradation in the shear contribution of concrete in LRS FRP-strengthened RC members by correlating it to the strain levels of the longitudinal reinforcement and transverse reinforcing materials (i.e., including both FRP sheets and transverse steel reinforcement).

### **3.4. SUMMARY**

An experimental program involving tests on ten RC beams strengthened in shear with fully wrapped LRS PET FRP sheets has been conducted. The test parameters include the strengthening ratio, the longitudinal reinforcement ratio as well as the shear-span to effective-depth ratio. In conclusion, PET FRP sheets with a large rupture strain can be used to enhance the shear strength of RC beams while substantially increasing the member ductility. In particular, PET FRP sheets did not rupture at the peak load and led to a ductile shear failure of the strengthened RC members. This failure mode also enabled us to clearly observe the behavior of shear strength degradation of concrete with the increase of shear deformation until the rupture of PET FRP sheets. Moreover, the increase of amount of PET FRP sheets led to an increase of the shear strength and shear ductility whereas a lower longitudinal reinforcement ratio and a smaller shear-span to effective-depth ratio corresponded to improved shear ductility. It is found that PET FRP sheets developed very high strains; namely the maximum strains of 1.4-6.0% at the peak shear loads and as high as 15.0% at the termination of tests. Finally, the initiation of the degradation of the shear contribution of concrete occurred even before the peak strength was developed in PET FRP-strengthened RC members. The shear contribution of concrete was found to degrade by 0-54.6% depending on the volumetric ratio of FRP sheets, the shear-span to effective-depth ratio and the member depth. This degradation of concrete contribution to shear strength is eligible in the case of no axial loading for the current study.

Owing to the close relation between the concrete shear deterioration, the member shear deformation and the strain levels in the transverse reinforcing materials including both FRP sheets and transverse steel reinforcement as observed in the current experimental results, further study will be carried out to build up a comprehensive model to explain the above relation. The development of such a comprehensive model will be reported and discussed in the next chapter.

## CHAPTER 4

### MATERIAL AND STRENGTH MODELS

#### 4.1. INTRODUCTION

A new method to predict load-deformation envelope responses of reinforced concrete (RC) columns both with and without fiber reinforced polymer (FRP) jacketing under seismic loading is presented. Firstly, the material stress-strain relationships such as concrete, steel reinforcement and jacketing materials are established. In concrete stress-strain model, the confinement effect in the pre-and post-peak regions is proposed for more precise prediction. Secondly, strength models consisting of flexural and shear strengths are developed. The flexural strength is predicted based on section analysis or fiber model, where as shear strength is developed based on truss mechanism. For steel jacketing, steel plates are assumed to limit an opening of shear cracks in vertical, horizontal and shear directions. For FRP jacketing, FRP sheets are assumed to resist the shear crack opening only in the fiber alignment. The interaction between flexural and shear strengths will be proposed. A flexure-shear interaction (FSI) analytical method is presented which allows a more precise prediction of the load-deformation responses of RC columns with and without seismic jacketing. In this FSI analytical method, conventional section analysis is applied by including a parameter for the confinement ratio as a function of the secant stiffness of the steel shear and fiber reinforcements. By including the effects of shear, the truss mechanism proposed by Sato et al. [52-54] is combined with the section analysis. After the onset of shear cracks, the additional flexural deformation due to the tension shift phenomenon is included for a more precise prediction of the flexural deformation. Use of a shear deformation model based on the truss mechanism accounts for the effects of tension stiffening, fiber confinement and proposed strut angle. The shear and flexural deformations are combined with the pull-out deformations to obtain an accurate prediction of the total deformations of the columns. The proposed analytical method can demonstrate shear strength and ductility enhancement of RC columns confined with both low and high fracture strain fiber materials, including steel jacket, CFRP, AFRP, PEN and PET FRP sheet.

#### 4.2. MATERIAL MODELS FOR STRENGTH ANALYSIS

##### 4.2.1. Concrete

Fig. 4.1 illustrates the stress-strain relationships of (a) concrete under compression, (b) concrete under tension, (c) reinforcing steel, and (d) reinforcing fiber. For a typical compressive concrete stress-strain relationship, as shown in Fig. 4.1a, separation into pre-peak and post-peak regions is convenient to examine the influence of confinement and concrete strength degradation. This separation of pre- and post-peak regions on the basis of relevant important criteria has successfully been developed in many studies [35,69]. These criteria for both regions are dependent on each other. For instance, the compressive strain of concrete at peak strength controls the criteria in both regions, while the ultimate strain significantly controls the criteria in the post-peak region. In the pre-peak region, the confinement effect provided by transverse steel reinforcement and fiber reinforcement as a jacket is described by a second-order parabolic function based on the models of Mander et al. [35] and Wang and Restrepo [69]. For the post-peak or softening region, it is assumed that, according to the previous models [30,35,69], the descending branch is a linear curve until the value of stress becomes equal to the residual stress, which is a constant even for

further increase in strain. The concrete model proposed by Jirawattanasomkul et al. [30] can be applied to evaluate the degradation in strength. The partial confinement effect in the section subjected to bending moment, where the confinement effect only exists in the compression zone, is considered in this model. In the post-peak region, the effective concrete strength is considered as the residual concrete strength. Figure 4.1b illustrates the corresponding stress-strain relationship for concrete under tension.

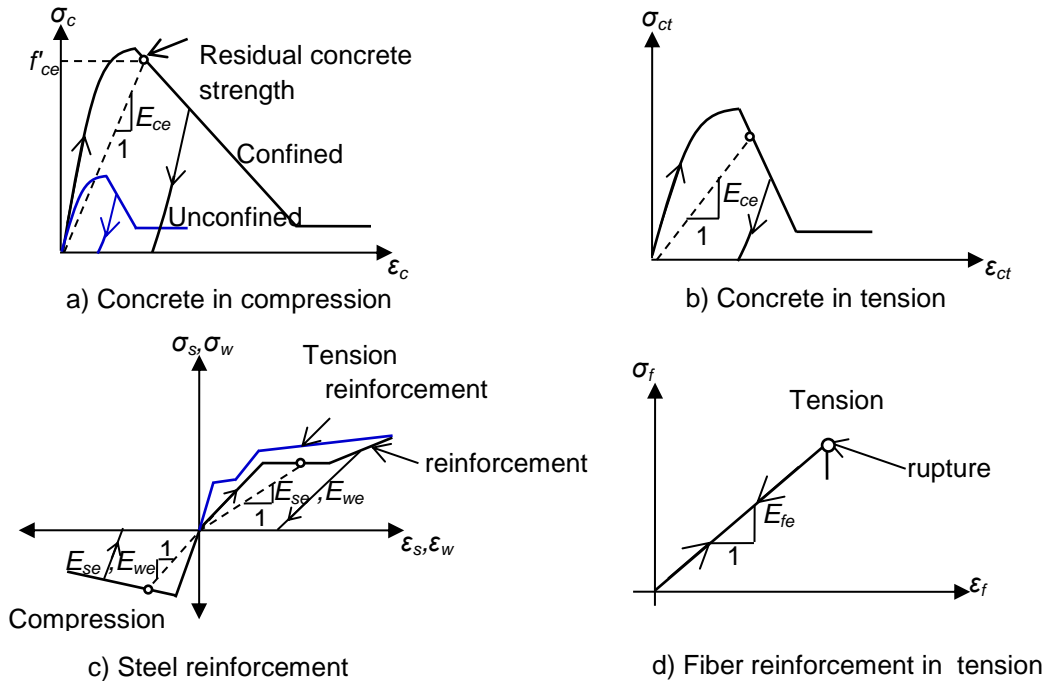


**Fig. 4.1** Stress-strain relationships and secant moduli

**4.2.2. Steel reinforcement**

Fig. 4.1c shows the stress-strain relationship of steel reinforcements. For the steel reinforcement under tension, a tri-linear model, which is applied for the un-embedded steel reinforcement stress-strain curve in tension, and includes the effects of (1) elasticity, (2) the yield plateau, and (3) strain-hardening. In the elastic region, the secant modulus of reinforcement ( $E_{se}$ ) is constant with a value equal to the Young's modulus. After the yielding point is reached, the steel reinforcement behaves plastically, resulting in a reduction of the secant modulus. For the embedded steel reinforcement, the stress-strain model proposed in CEB-FIP Model Code 1990 [12] is applied, which consists of stages for un-cracked concrete, crack formation, stabilized cracking and post-yielding. Regarding the compression part of the stress-strain curve, the buckling of reinforcement modeled by Dhakal et al. [17] causes a sudden reduction in the secant modulus, leading to a corresponding reduction in the compressive stress.

**4.2.3. FRP sheet**

Fig. 4.1d shows the stress-strain relationship of FRP reinforcements. The stress increases linearly with increasing tensile strain; a constant value of secant modulus is therefore obtained until rupture, when the secant modulus loses its stability. FRP jackets are subjected to only tensile loading since they elongate owing to the expansion of the inner concrete [30,69]. Therefore, in the analytical method, the stress-strain relationship of fibers is applied only for the tension region.

#### 4.2.4. Confinement effect

One important application of FRP-jacketing is the confinement effect due to fiber and steel tie. In fact, the confinement effect exists only in the compression region which can be indicated by the neutral axis depth ( $x_e$ ) and the lateral confining pressure provided by FRP jacket can be calculated by the simplified assumption [30] as in Fig. 4.2(a). For simplicity, the effective lateral confining pressure in y-direction ( $f_{ly,f}$ ) is a ratio of the neutral axis depth to the total depth ( $x/x_e$ ), whereas the lateral confining pressure in x-direction ( $f_{lx,f}$ ) is a half of the total concrete expansion. Therefore, the effective confinement in both directions is expressed in Eq. 8 and Eq. 9.

$$f_{lx,f} = \frac{1}{2} \rho_f \varepsilon_f E_f \quad (4.1)$$

$$f_{ly,f} = \frac{x}{x_e} \rho_f \varepsilon_f E_f \quad (4.2)$$

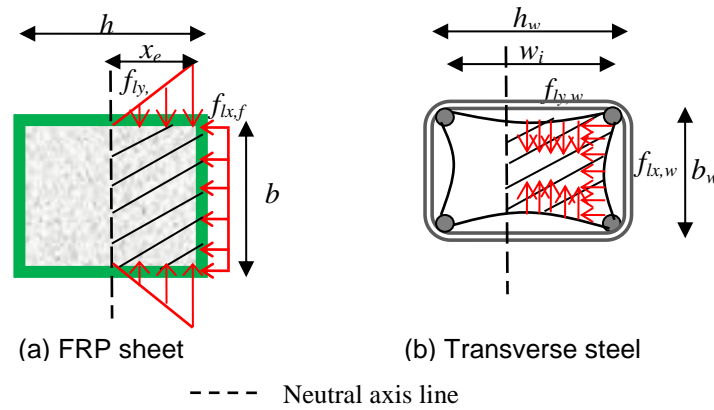


**Fig. 4.2** Lateral confining pressure

In Fig.4.2(b), the effective core concrete enclosed by steel tie is proposed as the arching action by Mander et al. [35]. In the assumption, the lateral pressure provided by steel tie in x- ( $f_{lx,w}$ ) and y-directions ( $f_{ly,w}$ ) is a function of stiffness of steel tie ( $E_w$ ) and the strain of steel tie ( $\varepsilon_w$ ) measured from the experiment.

$$f_{lx,w} = k_w \rho_w \varepsilon_w E_w \quad (4.3)$$

$$f_{ly,w} = k_w \rho_w \varepsilon_w E_w \quad (4.4)$$

Moreover, Mander et al. [35] developed the effective confinement coefficient ( $k_w$ ). The core dimensions to centerlines of perimeter steel tie in x- and y- directions are  $h_w$  and  $b_w$ , respectively. The clear distance between adjacent longitudinal bars is  $w_i$  and  $s'$  is a clear vertical spacing of tie reinforcement as shown in Fig. 4.3.

$$k_w = \frac{\left(1 - \sum_{i=1}^n \frac{(w_i)^2}{6b_w h_w}\right) \left(1 - \frac{s'}{2b}\right) \left(1 - \frac{s'}{2h}\right)}{(1 - \rho_{cc})} \quad (4.5)$$

where:  $A_{cc}$  = area of the core section enclosed by the center lines of steel tie and  $\rho_{cc}$  = ratio of total area of longitudinal reinforcement to area of the core section ( $A_c$ ).

$$k_w = \frac{\left(1 - \sum_{i=1}^m \frac{(w_y)^2}{6bd} - \sum_{i=1}^n \frac{(w_x)^2}{6bd}\right) \left(1 - \frac{s}{2b}\right) \left(1 - \frac{s}{2d}\right)}{1 - \rho_{cc}} \quad (4.6)$$

$$k_w = \frac{\left(1 - \frac{s}{2d_s}\right)^2}{1 - \rho_{cc}} \quad (4.7)$$

Since both steel tie and fiber jackets enclose the core section, the total lateral pressure in x- ( $f_{lx}$ ) and y- directions ( $f_{ly}$ ) derives from the summation of the lateral pressure provided by fiber sheet and steel tie. The maximum lateral stress ( $f_l$ ) is considered by using the larger value between Eqs. (4.8) and (4.9). To address the confinement effect to the concrete strength, Mander et al. [35] proposed the confined compressive strength of concrete ( $f'_{cc}$ ) as a function of the maximum lateral stress and the unconfined compressive strength ( $f'_c$ ) as in Eq. (4.10). In this equation, the concrete strength is equal to the unconfined concrete strength in case of no lateral pressure ( $f_l=0$ ).

$$f_{lx} = f_{lx,w} + f_{lx,f} \quad (4.8)$$

$$f_{ly} = f_{ly,w} + f_{ly,f} \quad (4.9)$$

$$f'_{cc} = f'_c \left( -1.254 + 2.254 \sqrt{1 + \frac{7.94 f_l}{f'_c}} - 2 \frac{f_l}{f'_c} \right) \quad (4.10)$$

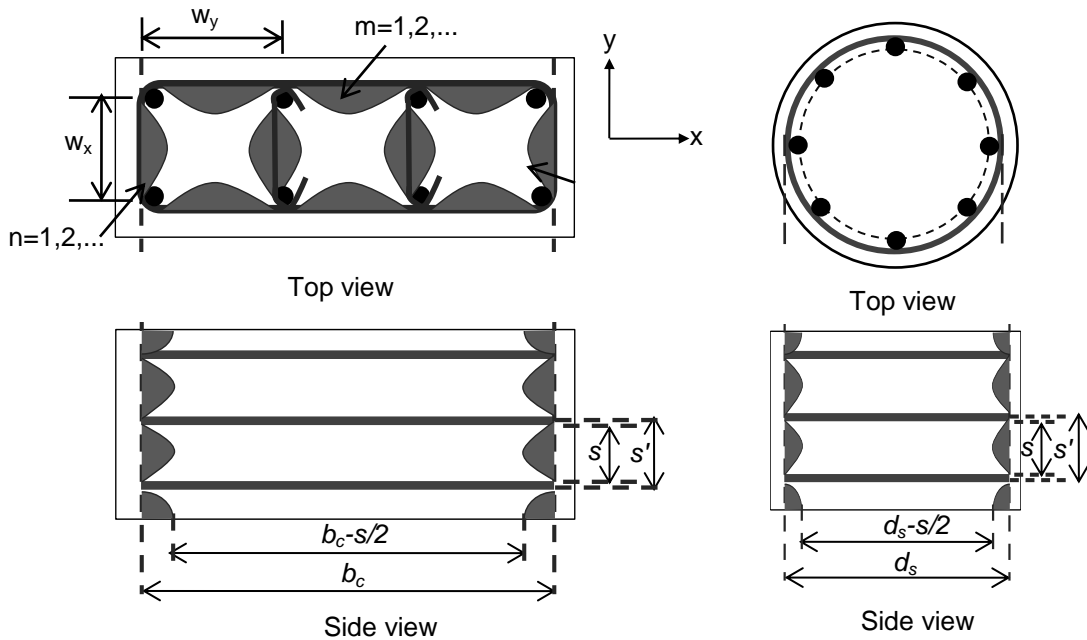
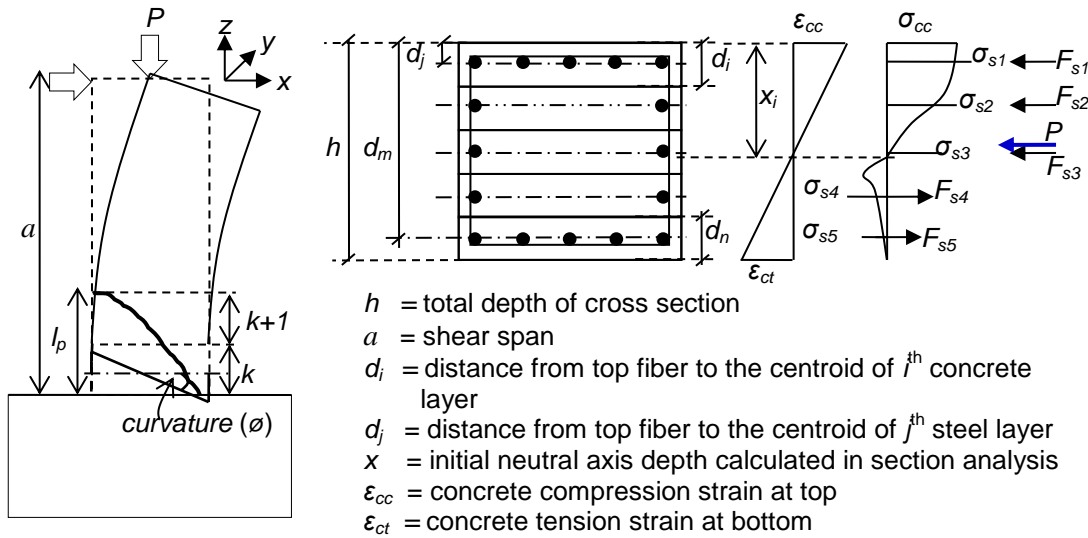


Fig. 4.3 Lateral confining pressure

### 4.3. FLEXURAL STRENGTH

The FSI analytical method makes use of both flexural and shear strength models. In the flexural strength model, conventional section analysis is applied using the stress-strain relationships of materials as mentioned in the previous section. By satisfying the compatibility and equilibrium conditions, the mechanical properties—secant stiffness and effective concrete strength—can be obtained. These properties are applied in the shear strength model which accounts for the effect of shear crack. One finds that the neutral-axis depth calculated from the shear strength model based on truss mechanism is reasonably accurate, whereas the flexural strength model gives an overestimate [34,38-39,52-54,65]. Because of this, the neutral axis depth obtained from the shear strength model is assigned in the flexural strength model. Then the stress-strain relationships of the materials are iterated in order to satisfy the compatibility condition and force equilibrium.



**Fig. 4.4** Section analysis

To calculate the flexural strength, a section analysis is performed by dividing the section area into a number of discrete strips, and it is assumed that plane sections remain planes at any loading level. In this analysis, the increments in strain for the compression at the top fiber are fixed, and the strain across the depth of the cross-section is assumed to be proportional to the distance from the neutral axis, as shown in Fig. 4.4. In the flexural strength model, the enhancement of flexural strength is a consequence of the confined concrete stress-strain relationship. For a given flexural cross section, the force and moment equilibrium conditions are given by Eq. (4.11) and Eq. (4.12), respectively. The corresponding shear force,  $V_{mu}$ , is obtained using Eq. (4.3).

$$P = \sum_{i=1}^n \sigma_{ci} A_{ci} + \sum_{j=1}^m \sigma_{sj} A_{sj} \quad (4.11)$$

$$M = \sum_{i=1}^n \sigma_{ci} A_{ci} d_i + \sum_{j=1}^m \sigma_{sj} A_{sj} d_j \quad (4.12)$$

$$V_{mu} = \frac{M}{a} \quad (4.13)$$

where

$$\sigma_{ci} = \text{stress in } i^{\text{th}} \text{ concrete layer} = \epsilon_{ci} E_{ci},$$

- $\sigma_{sj}$  = stress in  $j^{\text{th}}$  longitudinal reinforcement =  $\varepsilon_{sj}E_{sj}$ ,
- $A_{ci}$  = area of  $i^{\text{th}}$  concrete layer,
- $A_{sj}$  = area of  $j^{\text{th}}$  longitudinal reinforcement,
- $i, j$  = 1,2,3...n or m.
- $P$  = axial force,
- $M$  = moment at the considered cross section,
- $a$  = shear span (mm).

As expressed in Fig. 4.4, the strain compatibility equations of the  $i^{\text{th}}$  concrete and the  $j^{\text{th}}$  longitudinal reinforcement are given by the following equations:

$$\varepsilon_{ci} = \varepsilon_{ct} + (\varepsilon_{cc} - \varepsilon_{ct}) \frac{d_i}{h} \tag{4.14}$$

$$\varepsilon_{sj} = \varepsilon_{ct} + (\varepsilon_{cc} - \varepsilon_{ct}) \frac{h - d_j}{h} \tag{4.15}$$

From the section analysis, the secant moduli of materials ( $E_{se}$ ,  $E_{we}$ ,  $E_{ce}$ ), the effective concrete strength ( $f'_{ce}$ ), the strain of concrete at the compression edge ( $\varepsilon_{cc}$ ) and the initial neutral axis depth ( $x_i$ ) can be obtained. These parameters are applied in the shear strength model. However, the neutral axis depth used in the flexural strength model is not the same as that used in the shear strength model (Fig. 4.4) because of the shear crack opening (see Chapter 4.4).

#### 4.4. SHEAR STRENGTH MODEL

The main limitation of the section analysis is that the effect of the shear strength behavior, such as shear crack opening and reduction of the neutral axis depth on the flexural strength is not taken into account. The post-peak region of the load-deformation response is dominated by the shear strength behavior. To account for this, the truss mechanism approach proposed by Sato et al. [52-54] is combined with the section analysis to predict the shear strength more precisely.

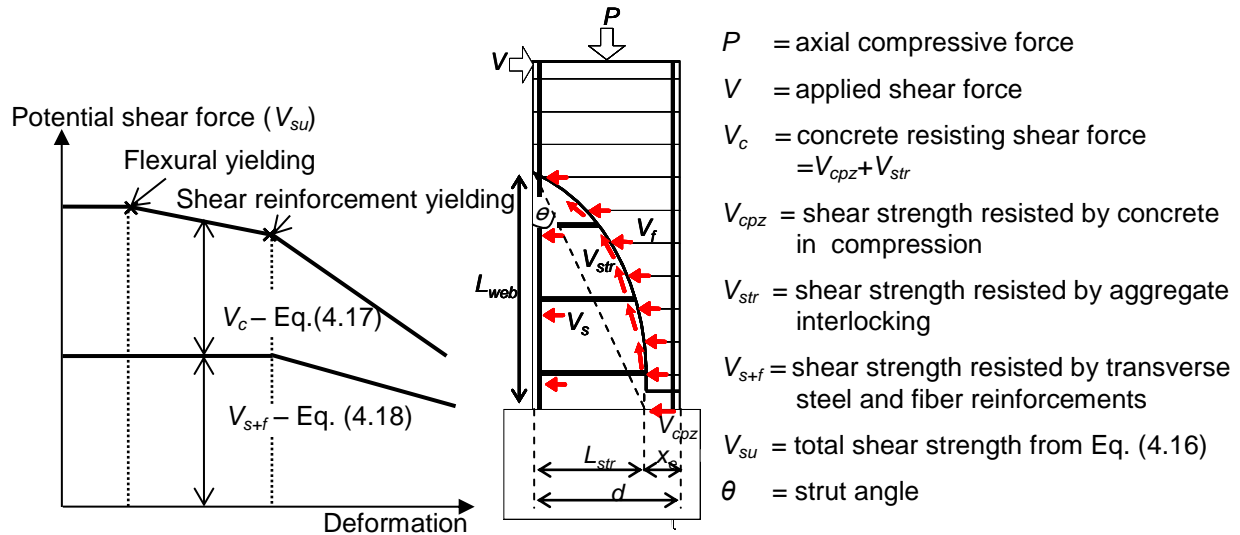


**Fig. 4.5** Shear strength model

Figure 4.5 illustrates the concept of the shear strength model based on the truss mechanism by Sato et al. [52-54]. This model is applicable for RC beams considering the yielding of reinforcements in reduction in stiffness. Although the shear resisting mechanism of RC beams is similar to that in RC columns, the location of the critical compression zone where concrete crushing occurs is different. For columns, this concrete compression zone is located near the tip of the major diagonal shear crack. Owing to the similarities between beam and column cases, Sato et al.'s model is implemented in the proposed analytical approach as a base for shear strength prediction, as explained later.

Previous experimental observations [5-6,34,38-39,41,47,52-54,57] showed that the shear strength of RC columns depends significantly on the secant stiffness of the flexural and shear reinforcements. As explained previously, the secant stiffness is obtained from the stress-strain relationships of materials which satisfy the compatibility and equilibrium conditions in the flexural strength model. When the flexural reinforcement reaches its yield point, a reduction of the flexural stiffness occurs, and then a drop of potential shear capacity is observed. Moreover, the potential shear capacity further decreases after the yielding of the shear reinforcement, because the shear reinforcement contribution shows no further increase.

The total shear strength can be expressed as a sum of the contribution from the concrete ( $V_c$ ) and the shear reinforcement ( $V_{s+f}$ ), as shown in Eq. (4.16). This shear reinforcement consists of contribution from transverse steel and fiber reinforcements.

$$V_{su} = V_c + V_{s+f} \quad (4.16)$$

The effective concrete strength ( $f'_{ce}$ ) is another important parameter in the shear strength model [5-6,34,38-39,41,47,52-54,57]. As indicated in Fig. 4.1a, the effective concrete strength, which is a function of strain in the post-peak region, is considered as the residual concrete strength in the compressive softening region. As a result, the concrete resisting force degrades after the onset of the reduction in the effective concrete strength.

In the post-peak region, the observed shear force for a given deformation can be considered as the remaining shear strength for that deformation. Column shear strength is influenced by several parameters, including column cross-sectional dimensions, shear-span to effective-depth ratio, concrete compressive strength, flexural reinforcement stiffness, transverse reinforcement stiffness, and axial load. While various existing shear strength models incorporate some of these variables [2,12,27,34,38-39,41,47,52-54,57], the development of a new shear strength model considering all the salient factors for columns is proposed. Following a review of available data and previous models, the shear strength contributed by concrete ( $V_c$ ) is modified based on the formula in JSCE-2007 accounting for the ideas proposed by Sato et al. [52-54] involving the stiffness of RC members, including the flexural and shear reinforcements. Using the experimentally observed shear force components, the shear strength can be assumed to depend on four parameters: the secant stiffness of the flexural reinforcement ( $\rho_s E_{se}$ ), the shear reinforcement ( $\rho_w E_{we} + \rho_f E_{fe}$ ), the shear-span to effective-depth ratio ( $a/d$ ) and the effective concrete strength ( $f'_{ce}$ ). Using a non-linear regression analysis, the concrete contribution to shear strength can be written as:

$$V_c = \beta_d \cdot \beta_p \cdot \beta_s \cdot \beta_w \cdot f_{vcd} \cdot b \cdot d \quad (4.17)$$

$$\text{where } f_{vcd} = 0.23 \sqrt[3]{f'_{ce}}, \beta_d = \sqrt[4]{a/d}, \beta_p = \sqrt{\frac{P}{2.5 A_g f'_{co}}}, \beta_s = \sqrt[4]{\rho_s E_{se}} \text{ and } \beta_w = \sqrt[4]{\rho_w E_{we} + \rho_f E_{fe}}.$$

In order to calculate the shear reinforcement contribution in Eq. (4.16), an approach related to that of the model of Sato et al. [52-54] is implemented. The average strains of the transverse steel reinforcement and fiber reinforcement ( $\varepsilon_w$  and  $\varepsilon_f$ ) are estimated, and the strains of both steel shear reinforcement and fiber reinforcement are considered to be equal to the average shear strain ( $\bar{\varepsilon}_w$ ):

$$V_{s+f} = bL_{web}(\rho_w\sigma_w + \rho_f\sigma_f) \quad (4.18)$$

where  $\sigma_w = \bar{\varepsilon}_w E_{we}$  and  $\sigma_f = \bar{\varepsilon}_w E_{fe}$

$$\bar{\varepsilon}_w = \frac{0.066}{\sqrt{\frac{a}{d} + 1}} \left( e^{-0.12\sqrt{\rho_w E_{we} + \rho_f E_{fe}} + \frac{4}{\sqrt{\rho_s E_{se}}} - 0.2\sqrt{f'_{ce}}} \right) \left( 1 + \left( \frac{\sigma'_n}{f'_{cc}} \right)^{0.2} \right) \quad (4.19)$$

To estimate the shear strength provided by the shear reinforcement shown in Fig. 4.3, the projected shear crack lengths along the vertical and horizontal axes ( $L_{str}$  and  $L_{web}$ ) together with the diagonal compression stress inclined at an angle  $\theta$  are calculated according to Eqs. (4.20) and (4.21):

$$L_{str} = h - x_e \quad (4.20)$$

$$L_{web} = \frac{L_{str}}{\tan \theta} \quad (4.21)$$

Sato et al. [52-54] proved that the neutral axis depth from the flexural strength model is inapplicable after shear cracking. This is because the plane-remains-plane assumption is no longer applicable. The neutral axis depth is reduced, resulting in an increase in the compressive stress. Their formula (Sato et al. [52]) indicated that the concrete compression depth ( $x_e$ ) is related to the initial neutral axis depth obtained from the section analysis ( $x_i$ ). Anggawidjaja et al. [6] modified formula proposed by Sato et al. by including the influence of fiber reinforcement on the neutral axis depth as shown in the following equation:

$$\frac{x_e}{x_i} = \left( \frac{1 - e^{-0.42a/d}}{1 + 3.2^{-0.12(\rho_w E_{we} + \rho_f E_{fe})^{0.4}}} \right) \left( 1 + \left( \frac{\sigma'_n}{f'_{cc}} \right)^{0.7} \right) \left( 1.25e^{-0.08\left(\frac{\rho_s E_{se}}{1000}\right)} \right) \quad (4.22)$$

In the case of steel jacket, the truss mechanism depicts the general case of shear reinforcement inclined at an angle  $\alpha$  to the vertical. It illustrates the relation between the external force ( $V_{s+j}$ ) to be resisted by the various internal forces. To satisfy equilibrium along the A-A section, the internal forces should balance with the external forces as shown in Fig. 4.6(a). The internal forces consist of the following: tension force in tension reinforcement ( $T_{st,t}$ ), compression force in compression reinforcement ( $C_c$ ), shear resisting force along shear crack ( $V_{str}$ ) and shear force carried by steel shear reinforcement ( $T_s$ ). The applied external forces are axial compression ( $P$ ) and applied lateral loads ( $V'_{s+j}$ ). Figure 4.6(b) is a simplified free body diagram including the jacket. The jacket induces a tension force along the tension tie direction ( $T_{jt}$ ) and a shear force along the shear cracking plane ( $S_{jt}$ ). Note that there is no  $S_{jt}$ -component in case of FRP-jacketing.

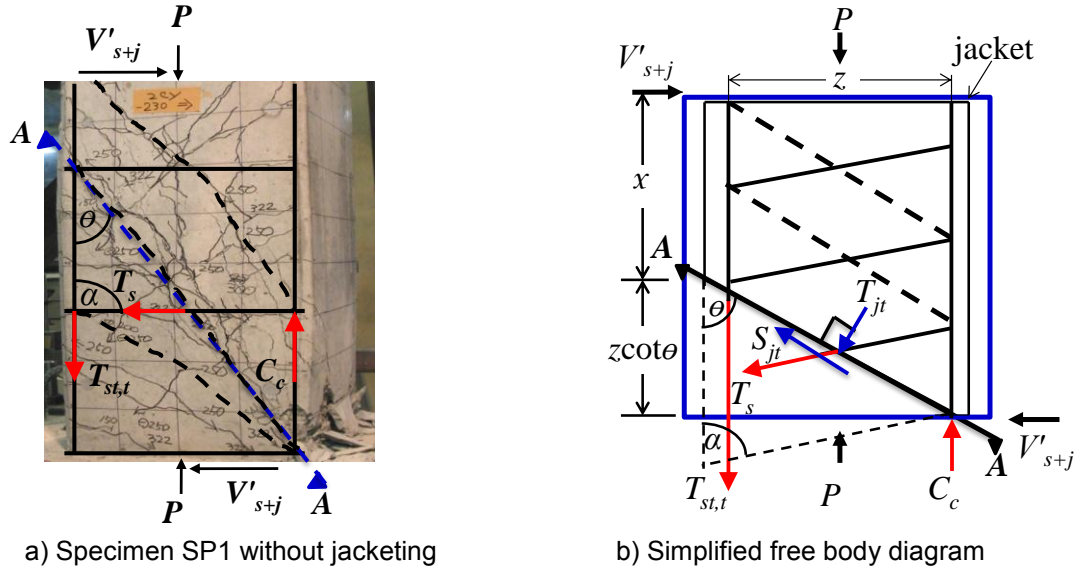


Fig. 4.6 Free body diagram of a cracked RC column

From the equilibrium condition, the shear force carried by the steel shear reinforcement and jacket can be obtained as follows:

$$V_{s+j} = T_s \sin \alpha + (T_{jt} + S_{jt}) \sin \theta \quad (4.23)$$

- FRP-jacketing (without  $S_{jt}$ -component):

$$V_{s+j} = bL_{web} \overline{\varepsilon_w} (\rho_w E_{we} + \rho_j E_{je}) \quad (4.23a)$$

- For rectangular steel-jacketing:

$$V_{s+j} = bL_{web} \overline{\varepsilon_w} (\rho_w E_{we} + \rho_j E_{je}) + S_{jt} \sin \theta \quad (4.23b)$$

- For elliptical steel-jacketing:

$$V_{s+j} = bL_{web} \rho_w E_{we} \overline{\varepsilon_w} + \int_0^{D-t_j} \frac{4\rho_j t_j}{2} (\sigma_{jt} + \tau_{jt} \sin \alpha) dx \quad (4.23c)$$

where  $S_{jt} = \tau_{jt} A_{jt}$ ,  $T_{jt} = \sigma_{jt} A_{jt}$  and  $A_{jt} = t_j z / \sin \theta$ .

Figure 4.7 shows reinforced concrete and steel jacket elements. For the given state of stress in alternative jackets (Fig. 4.7(a)), we can determine the normal and shearing forces exerted on the oblique face of the shaded triangular element as shown in Fig. 4.7(b). To evaluate these new stress components, we consider the force equilibrium of a triangular element in the directions of  $x'$  and  $y'$ :

$$\sigma_{jt} = \sigma_{xx} \sin^2 \theta + \sigma_{yy} \cos^2 \theta - \tau_{xy} \sin 2\theta \quad (4.24)$$

$$\tau_{jt} = (\sigma_{yy} - \sigma_{xx}) \sin \theta \cos \theta + \tau_{xy} \cos 2\theta \quad (4.25)$$

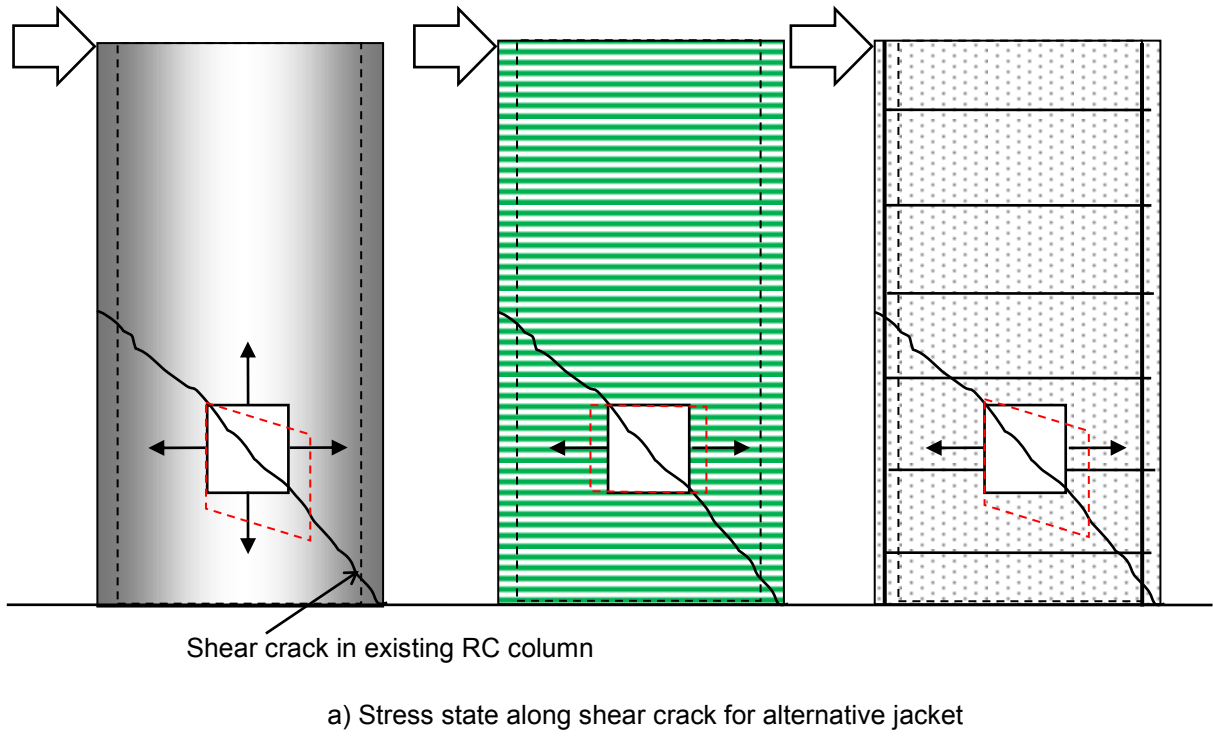


Fig. 4.7 Stress state of alternative jackets

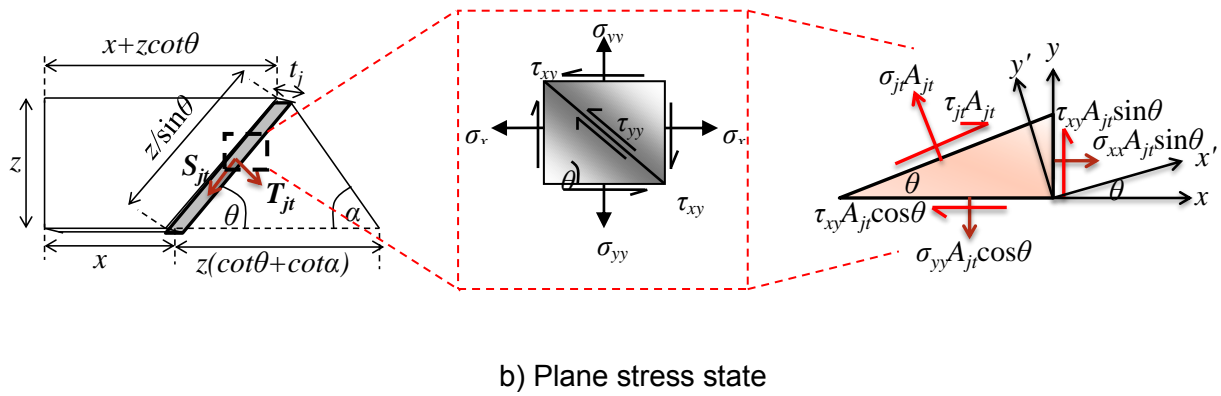
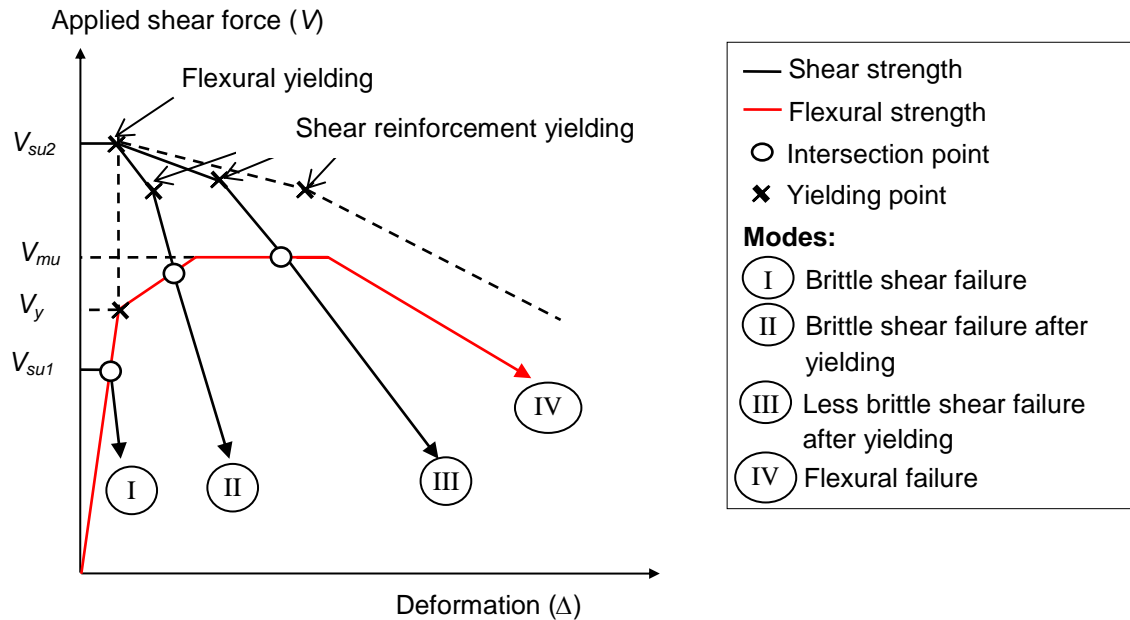


Fig. 4.7 Stress state of alternative jackets (continued)

#### 4.5. INTERACTION BETWEEN FLEXURAL AND SHEAR STRENGTHS

Fig. 4.8 illustrates the concept for failure modes of RC columns using interaction between the flexural and shear strengths. The relationship between the applied shear force ( $V$ ) and the total deformation of these columns ( $\Delta$ ) is indicated together with the flexural behavior under various conditions of shear strength ( $V_{su1}$  and  $V_{su2}$ ), where  $V_{su1}$  represents the shear strength of columns with insufficient shear reinforcement that fail in brittle shear before the flexural yielding ( $V_y$ ), and  $V_y$  is defined as the shear force at yielding of longitudinal reinforcement. On the other hand,  $V_{su2}$  represents the shear strength of columns with sufficient shear reinforcement, so shear failure occurs after the flexural yielding followed by shear reinforcement yielding, the latter being defined as the yielding of the shear reinforcement. This shear reinforcement yielding causes not only a reduction in stiffness but also leads to no further increase in



**Fig. 4.8** The concept for failure modes of RC columns

shear reinforcement contribution to the shear capacity, in turn leading to a further decrease in the potential shear strength. The intersection point between the curves representing the flexural strength and shear strength corresponds to the peak shear force, and this point corresponds to the initiation of the post-peak behavior. The failure mode can be distinguished by different cases of the intersection point. Mode I corresponds to a brittle shear failure, as the intersection point occurs before the flexural yielding ( $V_y$ ). This means that the potential shear strength is smaller than the flexural yielding strength. Although the shear failure causes a catastrophic collapse, many studies [34,47] show that shear failure after yielding can be observed when RC members reach their flexural yielding strength ( $V_y$ ) and peak flexural strength ( $V_{mu}$ ) before they fail in shear. Therefore, Mode II corresponds to a brittle shear failure after yielding in which the intersection point comes before the peak flexural strength ( $V_{mu}$ ) is reached. Mode III corresponds to a shear failure after yielding, which occurs when the curves representing the flexural and shear strengths intersect with each other after the development of the peak flexural strength. Finally, Mode IV corresponds to a flexural failure, as the shear strength is higher than the flexural strength even for large deformations. For the actual behavior of load-deformation response in RC columns, the applied

shear force ( $V$ ) should be equal to the smaller value of the two quantities  $V_{mu}$  and  $V_{su}$  for a given deformation.

#### 4.6. DEFORMATIONS MODELS

It is necessary to establish deformation models in order to evaluate the load-deformation response accurately. For RC columns, the total deformation is made up of flexural, shear and pull-out deformations.

##### 4.6.1. Flexural deformation model

The flexural deformation in the elastic region is estimated from the flexural stiffness,  $EI$ . After flexural cracking, an effective moment of inertia ( $I_e$ ) is considered to obtain the effective stiffness or the  $EI$ -value in the range between the partially cracked and fully cracked sections. Using Branson's equation [10], the effective moment of inertia is defined as the flexural rigidity of the cracked columns in the elastic range in which no yielding of tension reinforcement occurs:

$$I_e = I_g \left( \frac{M_{cr}}{M_{max}} \right)^3 + I_{cr} \left[ 1 - \left( \frac{M_{cr}}{M_{max}} \right)^3 \right] \quad (4.26)$$

The flexural deformation can be determined as follows:

$$\Delta_f = \frac{Va^3}{3E_c I_e} \quad (4.27)$$

where

$V$  = applied shear force (N),

$a$  = shear span (mm),

$I_g$  = moment of inertia of un-cracked cross section ( $\text{mm}^4$ ),

$I_{cr}$  = moment of inertia of cracked section ( $\text{mm}^4$ ),

$M_{max}$  = maximum moment in the member at the stage deflection is computed (N.mm),

$M_{cr}$  = cracking moment at the section (N.mm).

In the shear crack region ( $L_{web}$ ), the flexural deformation is calculated by the integration of curvature ( $\phi$ ) along the column length as in Eq. (4.28):

$$\Delta_f = \int_0^{L_{web}} \int_0^{L_{web}} \phi dz dz \quad (4.28)$$

where  $\phi = (\varepsilon_{cc} - \varepsilon_{ct}) / D$ ,  $\varepsilon_{cc}$  = strain of concrete at the compression edge,  $\varepsilon_{ct}$  = strain of concrete at the tension edge, and  $D$  = distance between the compression and tension edges.

Shear cracking results in a tension shift that produces an increase in the curvature. This in turn results in an increase in the flexural deformation. This will be discussed in Chapter 4.7.

## 4.6.2. Shear deformation model

### 4.6.2.1. Shear deformation in pre-yielding region

The system used to evaluate the shear deformation is shown in Fig. 4.9a. It consists of an RC column simulated as a truss system along the shear span length. The truss system is divided into a truss unit illustrated by coordinates,  $A$ ,  $B$ ,  $C$  and  $D$  in Fig. 4.9b. On movement of these target coordinates to the arbitrary coordinates,  $A'$ ,  $B'$ ,  $C'$  and  $D'$ , the shortening of the compression strut ( $\Delta l_{st,c}$ ) and the elongation of the tension tie ( $\Delta l_{st,t}$ ) generate the shear deformation components  $\Delta_{s1}$  and  $\Delta_{s2}$ , respectively, resulting in the total shear deformation,  $\Delta_s$  ( $= \Delta_{s1} + \Delta_{s2}$ ). These quantities are expressed as follows (Ueda et al. [65]):

$$\Delta_{s1} = \frac{\Delta l_{st,c}}{\sin \theta} = \frac{V'_{s+f}}{E_{ce} b (\cot \theta + \cot \alpha) \sin^4 \theta} \quad (4.29)$$

$$\Delta_{s2} = \frac{\Delta l_{st,t}}{\sin \alpha} = \frac{V'_{s+f}}{E_{we} (\cot \theta + \cot \alpha) \left[ \frac{1}{s} \left( A_w + \frac{E_{ce}}{E_{we}} A_{ce} \right) + \left( \frac{E_{fe}}{E_{we}} t_f \right) \right] \sin^3 \alpha} \quad (4.30)$$

where

- $b$  = width of cross section (mm),
- $E_{ce}$  = secant modulus of concrete (MPa),
- $E_{we}$  = secant modulus of transverse steel reinforcement (MPa),
- $E_{fe}$  = secant modulus of fiber reinforcement (MPa),
- $s$  = spacing of transverse steel reinforcement (mm),
- $t_f$  = thickness of fiber reinforcement (mm),
- $A_w$  = cross-sectional area of transverse steel reinforcement,
- $A_{ce}$  = cross-sectional area of surrounding effective concrete in tension,  $= A_{ceo} (V_{crack} / V)^3$ ,
- $A_{ceo}$  = cross-sectional area of surrounding effective concrete in tension immediately after shear crack  
 $= A_w f_{wy} / f_t$ ,
- $f_{wy}$  = yield strength of transverse steel reinforcement,
- $f_t$  = tensile strength of concrete,
- $V_{crack}$  = shear force at diagonal shear cracking suggested in JSCE-2007 standard specification [27],
- $V$  = applied shear force,
- $V'_{s+f}$  = shear force carried by transverse steel and fiber reinforcements,
- $\theta$  = strut angle,
- $\alpha$  = angle of transverse steel reinforcement.

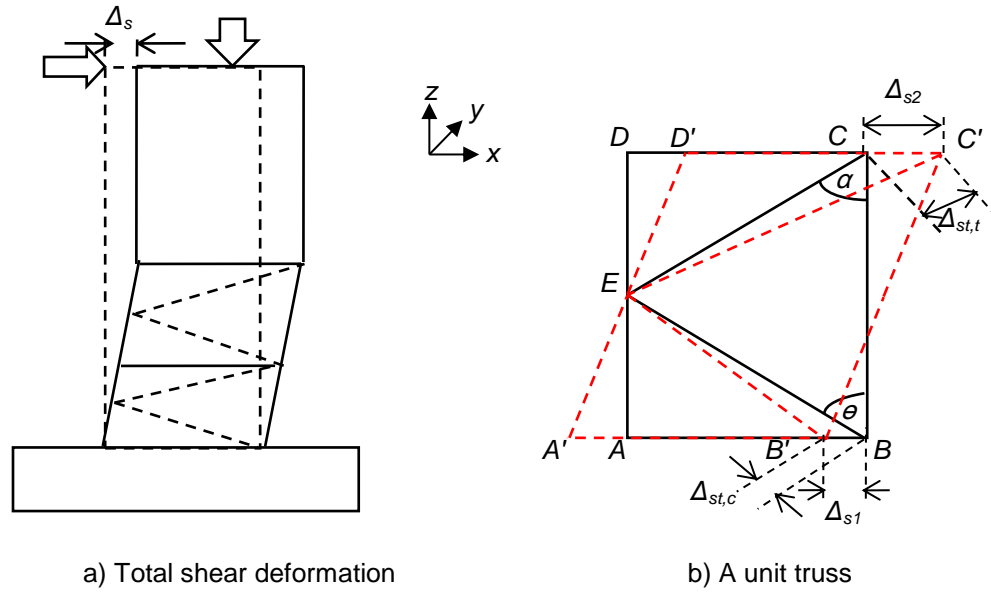


**Fig. 4.9** Truss analogy for shear deformation

Many studies [6,64-65] showed that the strut angle is a key factor affecting the shear deformation. Based on the formula proposed by Ueda et al. [65], the strut angle ( $\theta$ ) can be obtained by using a nominal shear stress,  $\nu (=V/bd)$ . The equations are shown as follows:

$$\theta = -\alpha(\nu - \nu_0)^2 + \theta_0, \text{ for } \nu_0 \leq \nu < 1.7\nu_c \quad (4.31)$$

$$\theta = \theta_1 \left( \frac{1.7\nu_0}{\nu} \right)^\beta, \text{ for } 1.7\nu_c \leq \nu \quad (4.32)$$

where

$$\theta_0 = 3.2 \left( \frac{a}{d} \right) + 40.2, \text{ for } a/d \leq 1.5 \quad (4.33)$$

$$\theta_1 = -\alpha_1(1.7\nu_c - \nu_0)^2 + \theta_0 \quad (4.34)$$

$$\nu_0 = 0.9\nu_c \quad (4.35)$$

$$\nu_c = 0.2(f'_{co})^{1/3} (100\rho_s)^{1/3} (1000/d)^{1/4} \left( 0.75 + \frac{1.4}{a/d} \right) \quad (4.36)$$

$$\alpha_1 = 0.4 \left( \frac{a}{d} \right)^2 + 2.9 \quad (4.37)$$

$$\beta = (0.7 - 32\sqrt{\rho_s\rho_w})a/d \quad (4.38)$$

To calculate the shear deformation, the shear force components in Eqs. (4.39) and (4.40)—shear force carried by concrete ( $V'_c$ ) and shear force carried by shear and fiber reinforcement ( $V'_{s+f}$ )—need to be clarified. In the pre-peak region, the applied shear force is not equal to the shear strength, so that the

concrete and shear reinforcement contributions that resist the applied shear force cannot be explicitly determined. In the post-peak region, the applied shear force is equal to the remaining shear strength, so the  $V'_c$ - and  $V'_{s+f}$ -values can be directly calculated from the shear strength model. The following steps, therefore, are taken to estimate the shear force components in the pre-peak region:

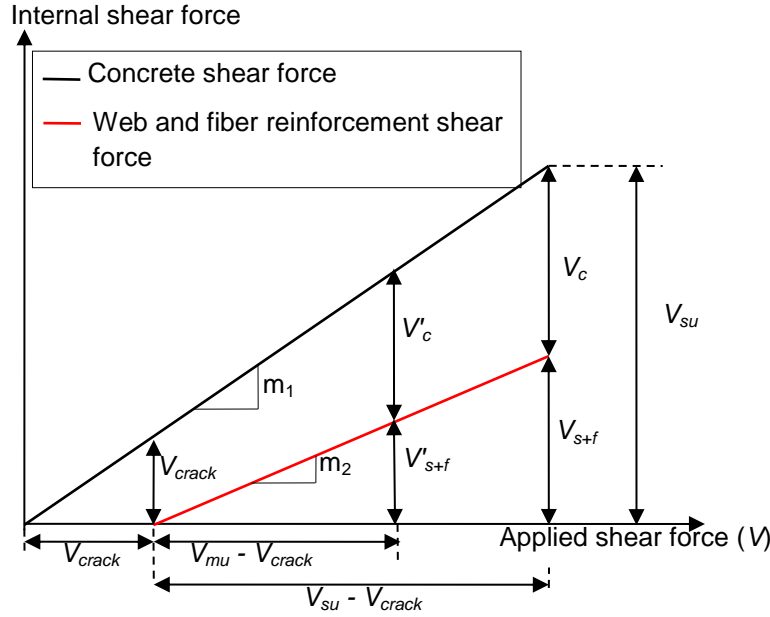


**Fig. 4.10** Shear force components and internal shear resistance relationship

- 1) For a given flexural reinforcement strain, the sectional moment and the effective concrete strength ( $f'_{ce}$ ) are calculated. The strength enhancement due to the confinement effect is taken into account in the calculation of the effective concrete strength.
- 2) The total shear strength ( $V_{su}$ ) as well as each shear force component ( $V_c$  and  $V_{s+f}$ ) are then calculated by the shear strength model.
- 3) Each shear force component is assumed to vary linearly from the shear cracking load ( $V_{crack}$ ) to the total shear strength ( $V_{su}$ ), as shown in Fig. 4.10, so that each shear force component ( $V'_c$  and  $V'_{s+f}$ ) under the shear force corresponding to the calculated moment can be calculated as follows:

$$V'_{s+f} = m_2 (V_{mu} - V_{crack}) = \frac{V_{s+f}}{V_{su} - V_{crack}} (V_{mu} - V_{crack}) \quad (4.39)$$

$$V'_c = V_{mu} - V'_{s+f} = V_{mu} - \left( \frac{V_{mu} - V_{crack}}{V_c + V_{s+f} - V_{crack}} \right) V_{s+f} \quad (4.40)$$

where

$V'_{s+f}$  = shear force carried by transverse steel and fiber reinforcements,

$V'_c$  = shear force carried by concrete,

$m_1$  = slope of the internal and applied shear forces before shear cracking, which is equal to 1

$m_2$  = slope of the internal and applied shear forces after shear cracking,  $= V_{s+f} / (V_{su} - V_{crack})$ .

#### 4.6.2.2. Shear deformation in post-yielding region

Although the current method presented in Chapter 4.6.2.1 can predict the shear deformation, it is not applicable to the post-yielding region. To improve the applicability of the model, a modified strut angle for the post-yielding region is obtained using a nonlinear regression approach in order to obtain a better shear-deformation correlation with the experiment. The strut angle in the calculation of the shear deformation is modified on the basis that the experimental value of shear deformation should be equal to that calculated. By changing the strut angle until these values show the best fit, the value of strut angle is obtained as a function of different parameters. These important parameters are the shear-span-to-depth ratio, stiffness of reinforcement and compressive concrete strength according to studies of previous researchers [65,70]. The model for the strut angle is as follows:

$$\theta = (-0.3 \ln A^2 + 4.4 \ln A - 10.74) (0.4 \ln B^2 - 4 \ln B + 12.9) (-0.8 \ln C^2 + 4 \ln C - 1.5) \quad (4.41)$$

where  $A = \rho_s E_{se}$ ,  $B = \rho_w E_{we} + \rho_f E_{fe}$  and  $C = f'_{ce}$ .

#### 4.6.3. Pull-out deformation model

In addition to the shear and flexural deformations, the pull-out of the steel reinforcement under tension at the section above the basement footing of the specimen should be included in the total deformation. Pull-out deformations stem from the elongation of the reinforcement relative to the anchoring concrete. These deformations result in additional lateral displacements that are not included in the flexural analysis. Slip models of the steel reinforcement have been developed by several groups [5-6,38-39,59]. A steel reinforcement embedded in concrete can be modeled by assuming linear elastic behavior and a uniform bond stress over the development length of the reinforcement. According to previous studies by Anggawiddjaja et al. [6], the slip model proposed by Shima et al. [59] shows good agreement with experimental results, and the pull-out deformation makes a large contribution after the yielding of the tension reinforcement. In the FSI analytical method, the same slip model is applied to calculate the pull-out deformation. From the pull-out model, it is clear that the pull-out deformation ( $\Delta_p$ ) is influenced by the flexure and shear strength behaviors because the slip is related to the depth of the neutral axis [52-54].

### 4.7. INTERACTION OF FLEXURE AND SHEAR ON DEFORMATION MODEL

Regarding the section analysis, the flexural deformation can only be reliably predicted before the onset of shear cracking. However, shear cracking increases the stress on the tension reinforcement, which invalidates the plane-remains-plane assumption in the section analysis. This phenomenon that is termed tension shift [21,65].

As shown in the free body diagram illustrated in Fig. 4.11, the cracked column is depicted as a truss analogy with the diagonal compression stress inclined at an angle  $\theta$  and the shear reinforcement aligned at an angle  $\alpha$ . The figure also illustrates the resisting force in the compression ( $C_c$ ) and the tension reinforcement ( $T_{st,t}$ ). In equilibrium, the shear force component carried by the shear reinforcement ( $V'_{s+f}$ ) should satisfy a balance condition with a tension force along the shear crack length ( $T_s$ ). The increase in the tensional stress due to the tension shift can be expressed by an additional tension force in the tension reinforcement ( $\Delta T$ ). Based on Ueda's model [65], the tension force increases when the shear force is larger than the diagonal shear crack force ( $V_{crack}$ ), as follows:

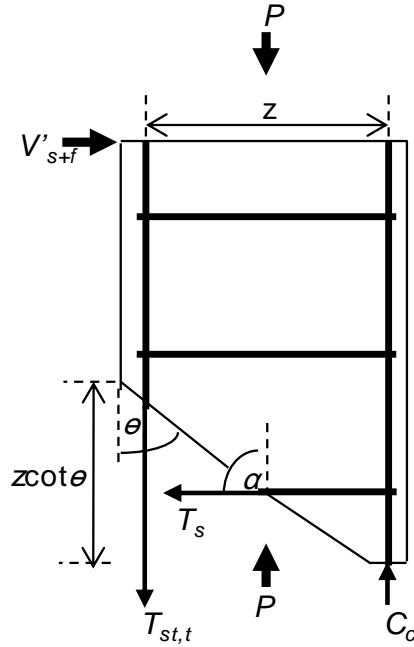


Fig. 4.11 Tension shift phenomenon [65]

$$\text{If } V \leq V_{crack}, \Delta T = 0 \quad (4.42)$$

$$\text{If } V > V_{crack}, \Delta T = V'_{s+f} \left( \frac{\cot \theta - \cot \alpha}{2} \right) \quad (4.43)$$

This additional tension force induces greater tensile stress, and the sectional moment ( $M$ ) remains the same even after shear cracking. This is because the diagonal compression strut force and/or the tension force in the shear reinforcement cancel the additional moment induced by the additional tension force in the tension reinforcement.

According to the tension shift effect, the additional tension force influences the increment of strain in the tension reinforcement. Consequently, an additional curvature ( $\Delta\phi$ ) is produced by the incremental strain, which leads to a larger flexural deformation. Moreover, the neutral axis depth due to shear cracking ( $x_c$ ) theoretically affects the flexural deformation in terms of the additional curvature of the section. In the shear cracking region or the plastic hinge region ( $L_{web}$ ), and accounting for the tension shift effect, the flexural deformation is given as follows:

$$\Delta_{f-shift} = \int_0^{L_{web}} \int_0^{L_{web}} \Delta\phi dz dz \quad (4.44)$$

where  $\Delta\phi$  = additional curvature of section.

After flexural yielding, the secant stiffness of flexural reinforcement continuously decreases with the increase in flexural deformation. According to the shear strength model, the contribution to the shear strength from the concrete (Eq. (4.17)) decreases with the decrease in secant stiffness of flexural reinforcement. The contribution of the shear reinforcement (Eq. (4.18)) then tends to increase under the same shear force, which results in an increase in shear deformation.

#### 4.8. THE FSI ANALYTICAL PROCEDURE

Figure 4.12 presents the analytical procedure for the FSI method. The first step in the analytical procedure assumes a fixed value of the strain in the concrete strain at the compression edge, which is defined as  $\varepsilon_{cc}$ . The section analysis is performed by dividing the section into number of strips, as previously explained in Fig. 4.2. By adding an incremental axial strain ( $\Delta\varepsilon_c$ ) until the compatibility and force equilibrium conditions are satisfied in the iteration process, all parameters—secant modulus of flexural reinforcement ( $E_{se}$ ), effective concrete strength ( $f'_{ce}$ ), initial neutral axis depth ( $x_i$ ) and flexural strength ( $V_{mu}$ )—can thus be determined. Using these parameters, the shear strength model based on the truss mechanism is considered. This model also requires an initial fixed value of the average shear reinforcement strain denoted by  $\varepsilon_w$  to determine the average shear reinforcement strain in Eq. (4.19). To ensure the accuracy of the fixed average shear reinforcement strain, an iteration process is performed by adding an incremental shear strain ( $\Delta\varepsilon_w$ ) until the initial fixed value of the average shear reinforcement strain is equal to that obtained from Eq. (4.19). Then, the neutral axis depth, including the shear crack effect ( $x_e$ ), is obtained and compared with the initial neutral axis depth from the section analysis ( $x_i$ ). The section analysis is then reanalyzed by updating the  $x_i$ -value to be fixed as the  $x_e$ -value ( $x_i = x_e$ ). During the reanalysis of the neutral axis depth in the section analysis, the two unknowns which are the strains at the compression and tension edges are varied until the equilibrium and compatibility conditions are satisfied. Then the shear strength value ( $V_{su}$ ) is calculated. If the  $V_{su}$ -value is larger than the  $V_{mu}$ -value, the behavior of RC columns is considered to be in the pre-peak region. If the  $V_{su}$ -value is smaller than the  $V_{mu}$ -value, the behavior of RC columns is considered to be in the post-peak region. Because the shear strength controls the post-peak behavior of RC columns, the  $V_{mu}$ -value should be equal to the  $V_{su}$ -value in the equilibrium equation. To account for this reduction of strength capacity in the post-peak region,  $\Delta\varepsilon_c$  is subtracted from  $\varepsilon_{cc}$ , resulting in the unloading stress-strain relationships of materials in the iteration process. Finally, the deformation components—flexure ( $\Delta_f$ ), shear ( $\Delta_s$ ), pull-out ( $\Delta_p$ ) and additional flexural deformation due to tension shift ( $\Delta_{f-shift}$ )—are calculated, and then the load-deformation response can be obtained.

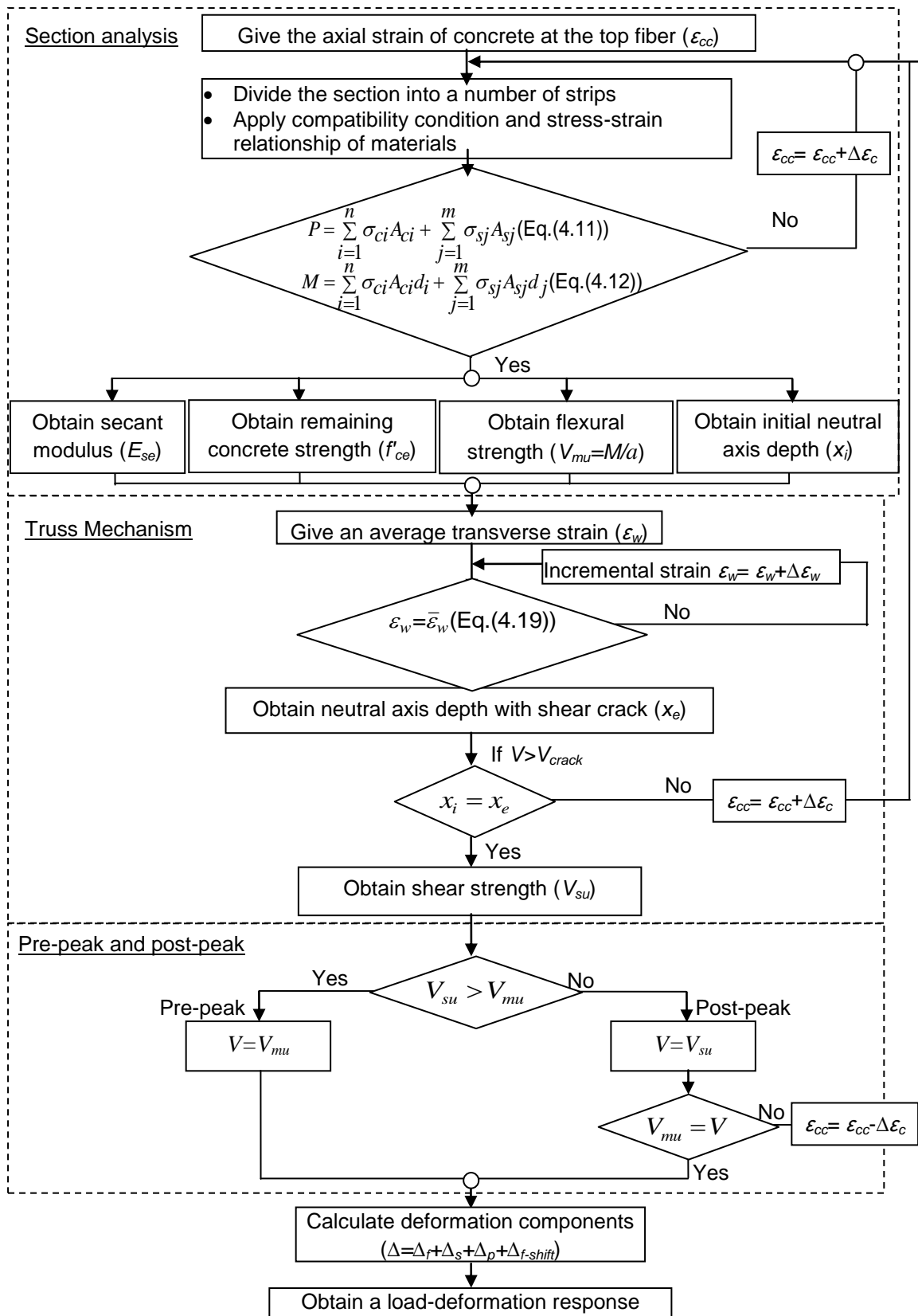


Fig. 4.12 The FSI analytical procedure

#### **4.9. SUMMARY**

In this chapter, the FSI analytical method is proposed based on both strength and deformation models. This flexure-shear interaction (FSI) analytical method for both strength and deformation includes (i) a shear strength model representing degradation of shear strength in post-peak region, (ii) a shear deformation model in the plastic hinge zone in the post-peak region, (iii) a flexural strength model considering confinement effects of transverse reinforcement and jacket, and (iv) a flexural deformation model. The interactions include (i) neutral axis depth reduction due to shear cracking, (ii) flexural reinforcement stress increase due to shear cracking (tension shift effect), (iii) effects of yielding of flexural reinforcement on shear strength, and (iv) effect of concrete compression softening on shear strength. The proposed analytical method is demonstrated to predict accurately the pre-peak and post-peak load-deformation response, including the strain response of shear reinforcement until the ultimate point of the rupture of non- and FRP-jacketed RC columns. This analytical method will be extended its application in the cases of steel jacketing.

The verification of the proposed shear strength model as well as the FSI analytical method will be shown in the next chapter, in which includes several RC members strengthened by FRP with high fracture strain (PEN and PET), conventional fiber (AFRP and CFRP) and steel plates.

## CHAPTER 5

### MODEL VERIFICATION

#### 5.1. INTRODUCTION

In this chapter, the verification of proposed models is described for both RC beams and columns. The proposed analytical approach is verified by means of a series of experiments on various cross-section of RC beams and columns (e.g., square, rectangular and elliptical section) strengthened with and without seismic jacketing tested under reversed cyclic loading. The parameters considered here are compressive strength of concrete, longitudinal reinforcement ratio, transverse steel reinforcement ratio, fiber volumetric ratio, shear-span to effective depth ratio, axial load ratio, and type of jacketing materials (e.g., FRP sheets and steel plate with welding connection). In the discussion part, the peak shear strength and load-deformation responses obtained from experiments and models are compared. The proposed confinement model is also verified in terms of load-deformation responses with and without taking into account of confinement effect. The fracture of FRP jacketing materials such in conventional FRPs (e.g., CFRP) is predicted and compared with that in experiment. For steel-jacketed RC members, the assumption that steel jacket limits the opening of shear cracks in vertical, horizontal and shear directions, will be proved by comparing with several shape of cross-section. In addition, the ultimate deformation defined at 80% of peak load and deformation components (e.g., flexural, shear, pull-out, and tension split induced deformations) are also evaluated in this chapter.

#### 5.2. LOAD-DEFORMATION MODELS AND COMBINED RESPONSE

##### 5.2.1. Comparison of peak shear strength from experiments and models

###### 5.2.1.1. Beam tests

In Table 2.1, the analytical parameters are taken to estimate the shear. The analytical parameter consists of the compressive strength of concrete ( $f'_c$ ) which is from the experimental observation whereas the confined compressive strength ( $f'_{cc}$ ) is from Eq. 4.10. The other parameters are shear-span to effective-depth ratio ( $a/d$ ), the stiffness of tension reinforcement ( $p_s E_s$ ), steel tie ( $p_w E_w$ ) and fiber ( $p_f E_f$ ). In this study, the shear strength components consist of shear strength contributed by concrete ( $V_c$ ) and shear reinforcement ( $V_s$ ) so the verification of shear strength can separate in each component, if the data is available.

The ultimate shear strength from the experiments [30,44] is compared with the total shear strength ( $V_{total}=V_c+V_s$ ) predicted by the proposed model. In Fig. 5.1, the  $V_{total}$  obtained from models correlates well with the shear strength observed in the experiment with and without PET strengthening.

The experimental results tested by the authors are shown as a blue rectangular marker in all the graphs. Starting from the comparison between calculated and experimental concrete shear strength, the results from the experiment and model are illustrated in Fig. 5.2a. The concrete shear strength is considered from the actual shear contribution of concrete at ultimate load. However, the experimental observations showed the reduction of concrete shear strength after the shear crack becomes wider which leads to not only the loss of shear force due to the aggregate inter-locking and also the decrease of concrete compression zone. The proposed model shows a good correlation with the experimental results in terms

of concrete shear strength. In Fig. 5.2b, the shear strength carried by fiber and steel tie obtained from the model is conservative compared with the experimental results. This is because the shear crack is assumed to be equal to  $45^\circ$ . With this assumption, the number of fiber and steel tie across the shear crack is slightly underestimated. In fact, the inclination of the shear crack is smaller than the assumed value so the calculated shear force shows conservative value.

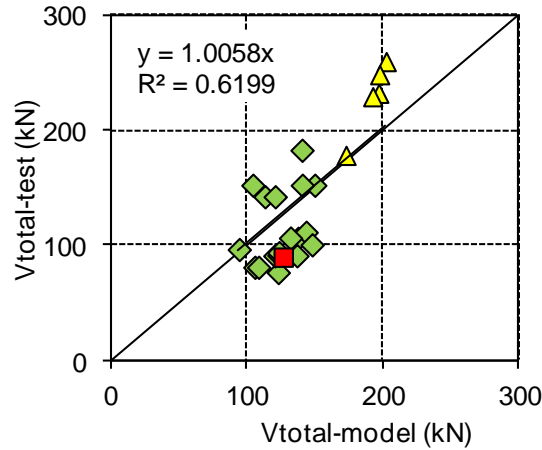


**Fig. 5.1** Comparison between  $V_{total}$  from experiment and  $V_{total}$  from model

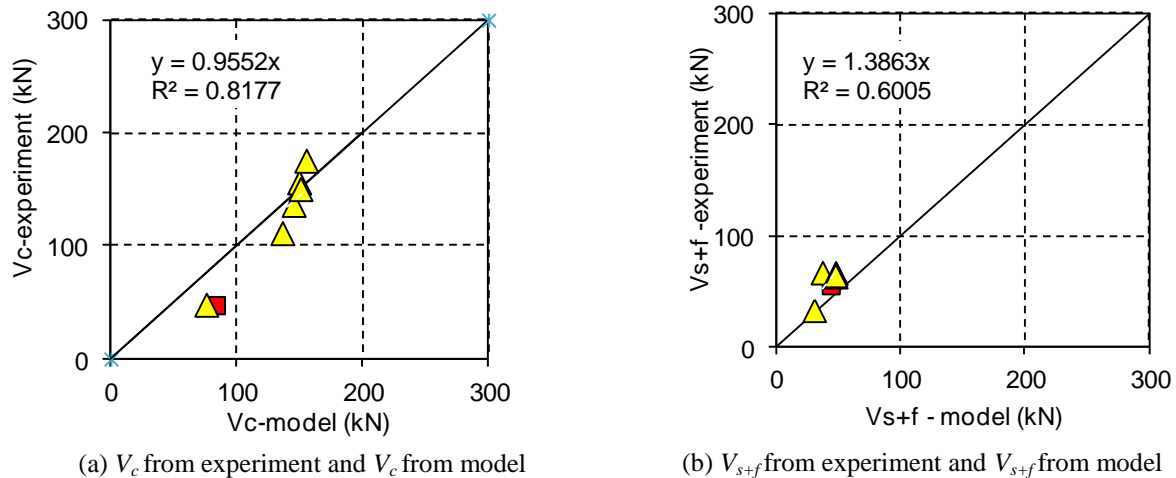


**Fig. 5.2** Comparison between shear strength resisted by concrete and transverse reinforcement

**5.2.1.2. Column tests**

To evaluate the applicability and accuracy of the FSI analytical method, experimental results of twenty tests on RC columns failing in shear, flexure-shear and flexure were compiled. Data sets of a total of fifteen square RC columns (denoted as SP) tested by Anggawiddjaja et al. [5-6] are used, involving various types of FRP jackets, Aramid, PEN and PET fibers. The cross-sections of their columns are  $400 \times 400 \text{ mm}^2$  and  $600 \times 600 \text{ mm}^2$ . Fig. 9 shows a test setup and an example of a specimen tested by Anggawiddjaja et al. [5-6]. Data sets of RC columns tested by Iacobucci et al. [23] are also used. In their study, reinforced concrete square columns with insufficient shear steel reinforcement were used to represent existing old columns designed according to old seismic specifications. Their main focus was on

testing RC columns with and without CFRP jacketing under lateral cyclic displacement and high axial load ratio ( $P/f'_{co}A_g$ ). Their columns are denoted as AS and ASC with a cross-section of  $305 \times 305 \text{ mm}^2$ . Additionally, the FRP was aligned along the entire height of the specimens. The fibers were oriented perpendicular to the longitudinal axis of the column or in the shear direction. According to the flat coupon tensile tests [5-6,23], the fracture strains of Aramid, PEN, PET and carbon fiber composite are 4.1%, 4.5%, 13.8% and 1.26%, respectively. More data sets on plain RC columns failing in shear tested by Saatcioglu and Ozceb [51] and by Sezen et al. [57] are used to verify the applicability of the analytical method to typical reinforced concrete. In their study, reinforced concrete square columns are used with varied shear steel reinforcement ratio, concrete compressive strength and axial load ratio. Their columns are denoted as U1-U4, 2CLD12, 2CHD12, 2CVD12 and 2CLD12M with a cross-section of  $350 \times 350 \text{ mm}^2$  and  $457 \times 457 \text{ mm}^2$ . The details of the specimens are previously shown in Table 2.2, in which column (1) shows the specimen labels, and the types of FRP jacket, when applicable are shown in columns (2). The material and geometry properties are shown in columns (3) to (10) in the order of shear-span to depth ratio ( $a/d$ ), unconfined concrete compressive strength ( $f'_{co}$ ), ratio of the tension reinforcement ( $\rho_s$ ), ratio of steel shear reinforcement ( $\rho_w$ ), volumetric ratio of fiber reinforcement ( $\rho_f$ ) and an axial load ratio ( $P/f'_{co}A_g$ ). The comparison of the peak shear strength obtained from experiment and models are shown in Fig. 5.3.

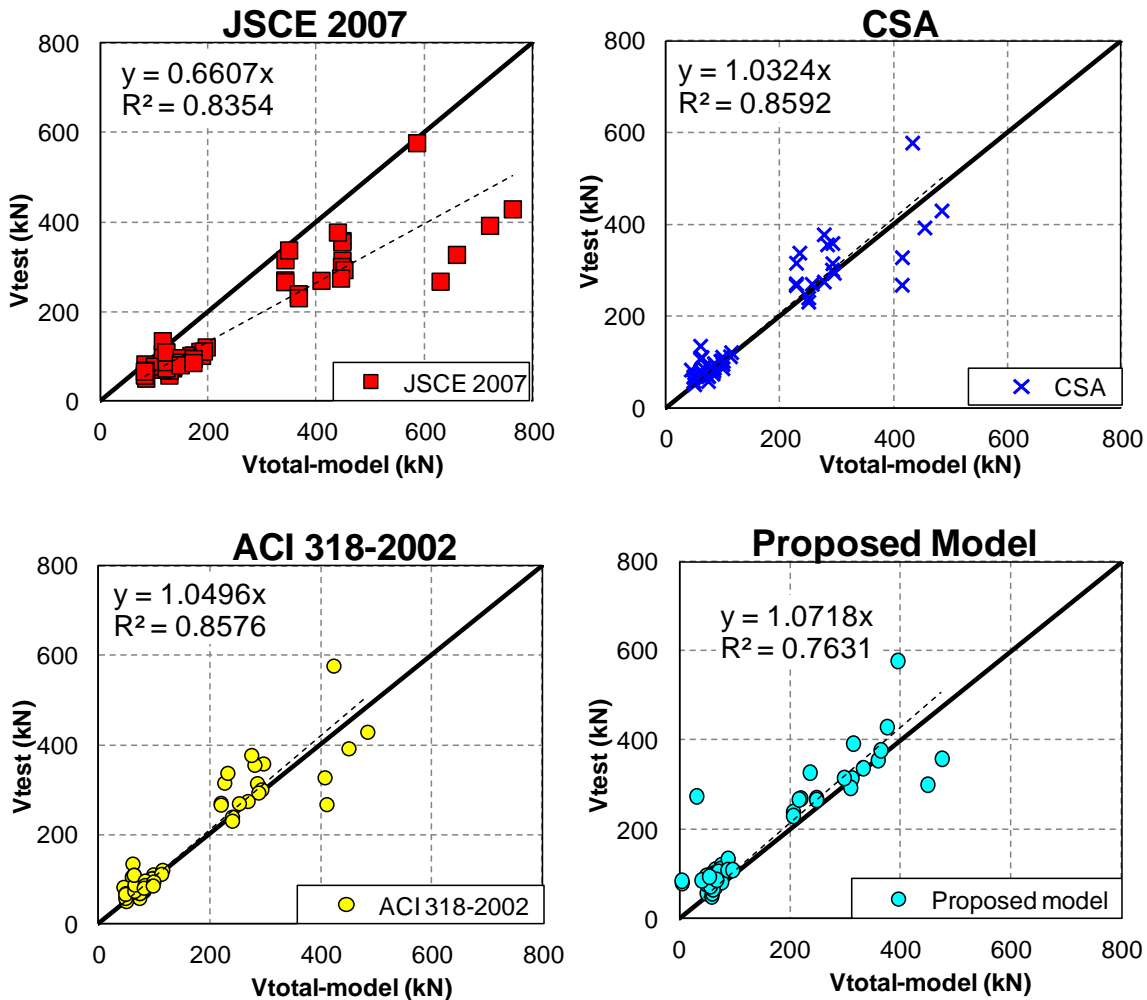


Fig. 5.3 Peak shear strength from experiments and various models

5.2.2. Comparison of load-deformation from experiments and models

For simplicity, analytical and experimental load-deformation responses under reversed cyclic load are shown as envelopes to the curve. The strength and deformation models were applied. Regarding the flexural strength model, the section analysis including the confinement effect correctly predicts the load-deformation response of the specimen failing in flexure (SP2 and SP3), as shown in Fig. 5.4, and similar results were observed in other specimens. As shown in Fig. 5.4, the confinement effect can be clearly seen, especially in the post-peak region.

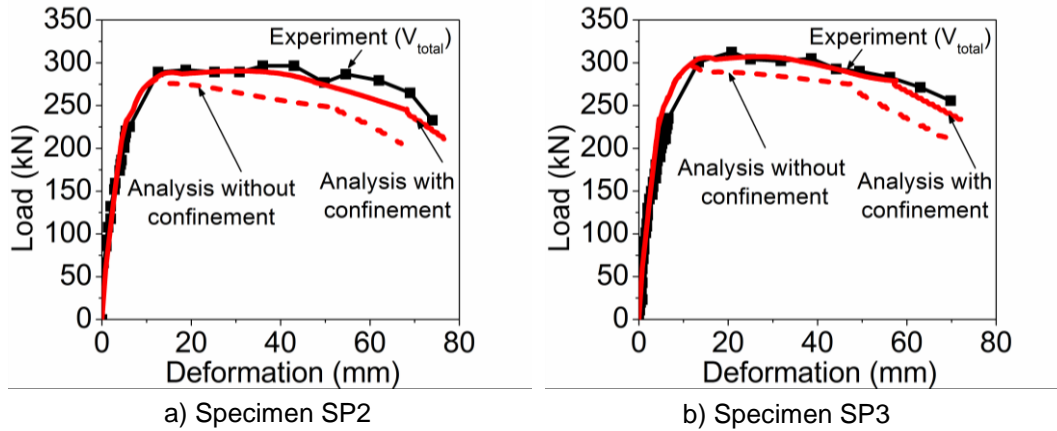
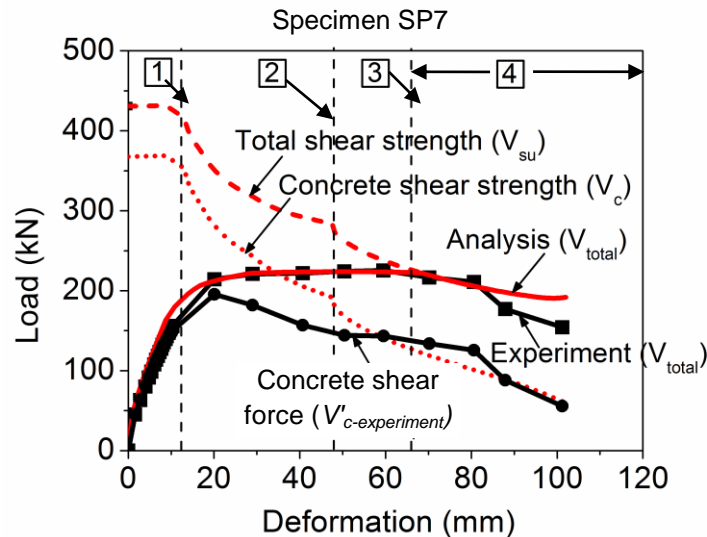


Fig. 5.4 Load-deformation responses with and without the confinement effect

To evaluate the shear strength degradation in the post-peak region, the specimens failing in shear were taken. Figure 5.5 shows the load-deformation response corresponding to the strength models and experimental result of SP7, which exhibited a less brittle shear failure after yielding (see Fig. 4.4).



1= flexural yielding line, 2= shear yielding line, 3 = intersection line, 4 = post-peak region

Fig. 5.5 Load-deformation response corresponding to the strength models and experiment

The testing results can be considered separately in the pre-peak and post-peak regions. In the pre-peak region, where the curves of the flexural and shear strengths do not intersect, the total shear strength ( $V_{su}$ ) starts to drop after the flexural yielding point (see point 1 in Fig. 5.5). Further decrease can then be observed after the shear reinforcement yielding point is passed (point 2). After the intersection point, the shear strength becomes dominant, leading to a drastic decrease in load-carrying capacity. In the post-peak region, the observed concrete shear force ( $V'_c$ -experiment) is considered as the residual concrete shear strength ( $V_c$ ). The concrete shear force from experiment ( $V'_c$ -experiment) is calculated by subtracting the  $V'_{s+f}$ -value from an applied shear force ( $V$ ) measured by the loading machine. The  $V'_{s+f}$ -value is obtained from the measured value using two strain gauges, which are mounted on the steel and fiber reinforcements. Good correlation between the concrete shear force in the post-peak region obtained from experiment and concrete shear strength calculated from Eq. (6) can be achieved in the post-peak region.

### **5.2.2.1. Experimental results of Anggawiddjaja et al.**

The load-deformation responses of specimens tested by Anggawiddjaja et al. [5-6] are shown in Fig. 5.6. For specimens SP1-4, the effectiveness of Aramid, PEN and PET FRP jacket in strength and ductility enhancement is examined, as shown in Figs. 5.6(a)-(d). The experimental results reveal that specimen SP4 with PET FRP has a higher ductility than the PEN FRP (SP3), Aramid (SP2) and the control (SP1) specimens. The analytical results for SP1-4 correlate well with the experimental results. The FSI analytical method can accurately predict the behavior of specimens SP2 and SP3 failing in flexure (Mode IV), and that of specimens SP1 and SP4 failing in brittle and less brittle shear after yielding (Mode II and III). For flexure failure, the analytical results of specimens SP2 and SP3 show the reduction of load-carrying capacity due to the buckling of reinforcement. For shear failure after yielding, specimens SP1 and SP4 clearly show the decrease in the load-carrying capacity at the intersection point of flexural and shear strengths.

For specimens SP5-10, the effects of the fiber volumetric ratio ( $\rho_f$ ) and the shear reinforcement ratio ( $\rho_w$ ) on the improvement of strength and ductility are examined, as shown in Figs. 5.6(e)-(j). A sudden decrease in load-carrying capacity is observed in SP8 (the control specimen) because concrete strength reduction due to compression softening, spall-off and reduction of reinforcement stiffness occurs simultaneously. However, specimens jacketed by PET FRP, namely SP5, SP6, SP7, SP9 and SP10, show higher values of both load-carrying capacity and ductility, which can be predicted by the FSI analytical method. In specimens SP7, SP9 and SP10, the FSI analytical method can also predict the rupture of PET fiber. Note that the rupture in the analysis means that the calculated fiber strain ( $\varepsilon_f$ ) reaches the rupture strain obtained from the fiber coupon test.

Specimens SP11 and SP12 were tested to determine the effects of column size and fiber ratio, as shown in Figs. 5.6(k) and (l). As for these specimens, the FSI analytical method can accurately predict not only the load-deformation response but also the rupture of PET fiber which affects the ultimate deformation.

Specimens SP13-15 were tested to investigate the effects of replacing transverse steel reinforcement with FRP by increasing the fiber volumetric ratio and reducing web reinforcement. In Figs. 5.6(m)-(o), the experimental and analytical results are compared, and show good agreement.

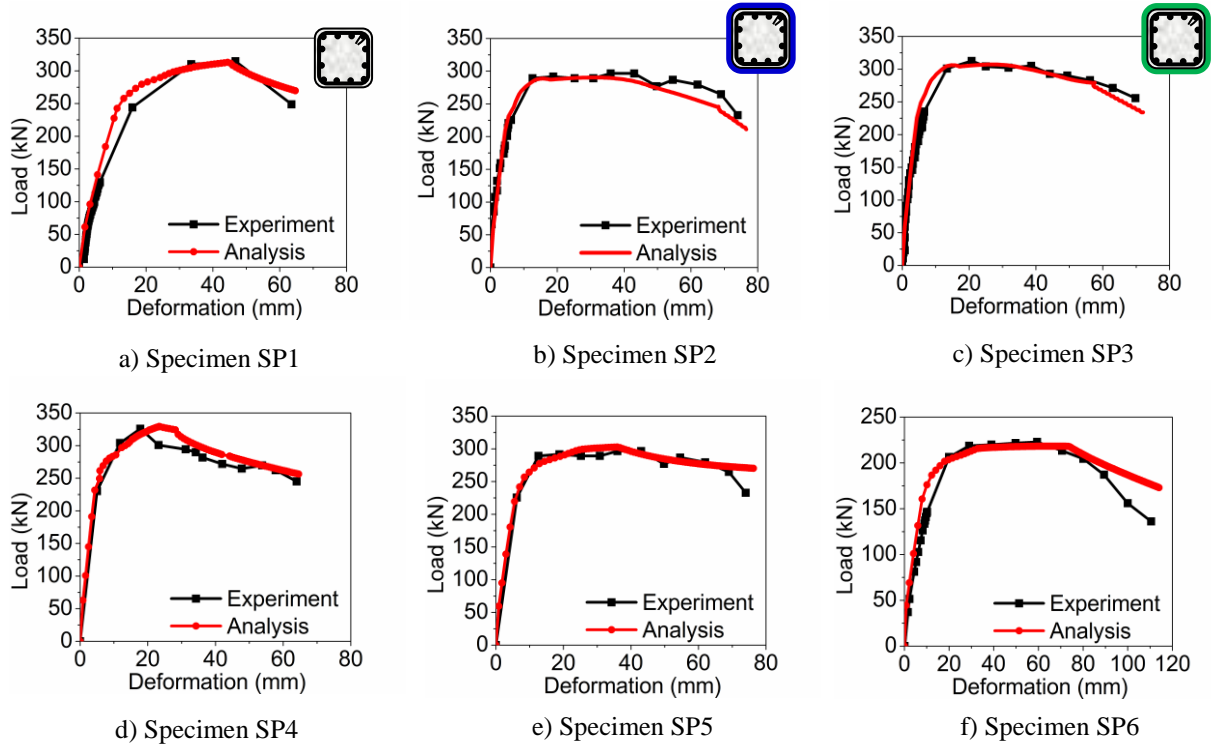
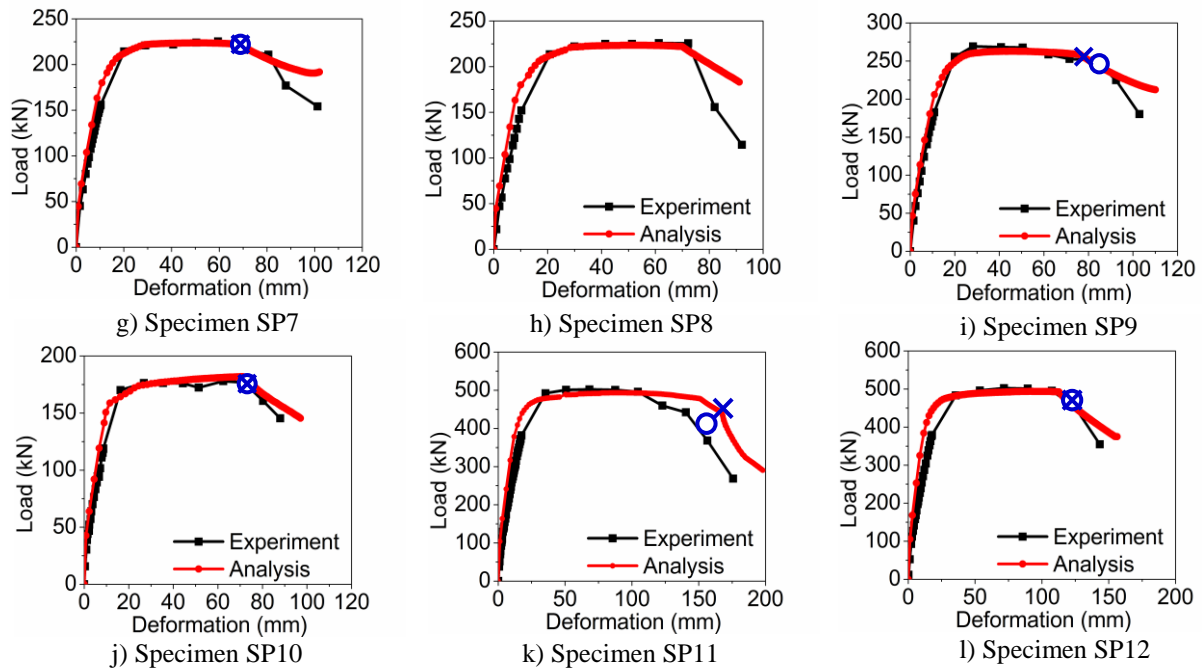


Fig. 5.6 Load-deformation responses of specimens tested by Anggawiddjaja et al. [5-6]



○ Breakage of fiber in experiment    × Breakage of fiber in analysis

Fig. 5.6 Load-deformation responses of specimens tested by Anggawiddjaja et al. (continued)

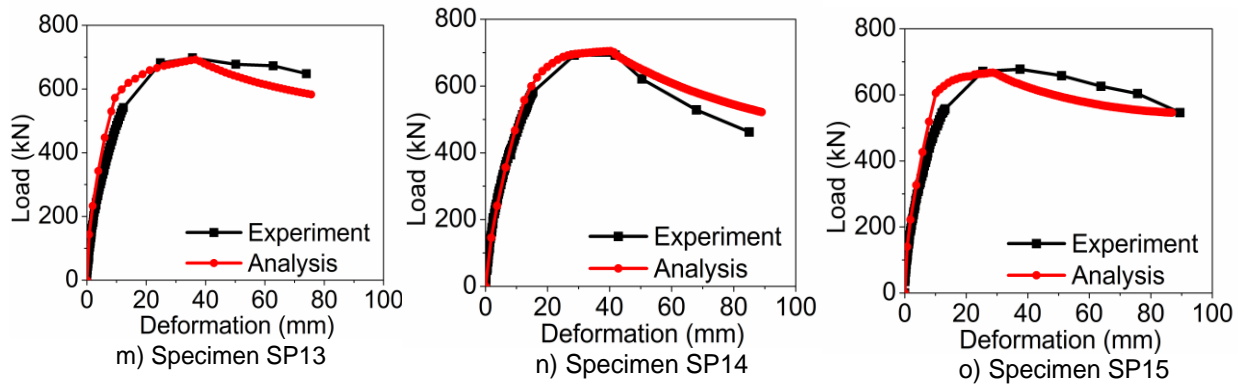


Fig. 5.6 Load-deformation responses of specimens tested by Anggawiddjaja et al. [5-6] (continued)

5.2.2.2. Experimental results of Iacobucci et al.

To verify the FSI analytical method for specimens jacketed by CFRP, the experimental and analytical results of Iacobucci et al. [23] are compared in Figs. 5.7(a)-(e). The load-carrying capacity of specimen AS-NS1 failing in brittle shear after yielding (Mode II) suddenly drops owing to concrete spall off and less confinement of shear reinforcement. The proposed analytical approach overestimates the post-peak region of the load-deformation behavior because of an overestimation of the shear strength. Moreover, the concrete is assumed to carry 20% of the compressive strength in the softening-concrete model, whereas in fact the cover concrete cannot carry load after its spall-off. To examine the influence of fiber ratio on the shear strength and ductility, the retrofitted columns ASC-NS2-5 were analyzed. It can be seen that the analytical method can accurately predict the post-peak behavior of these retrofitted columns, including the rupture of carbon fiber.

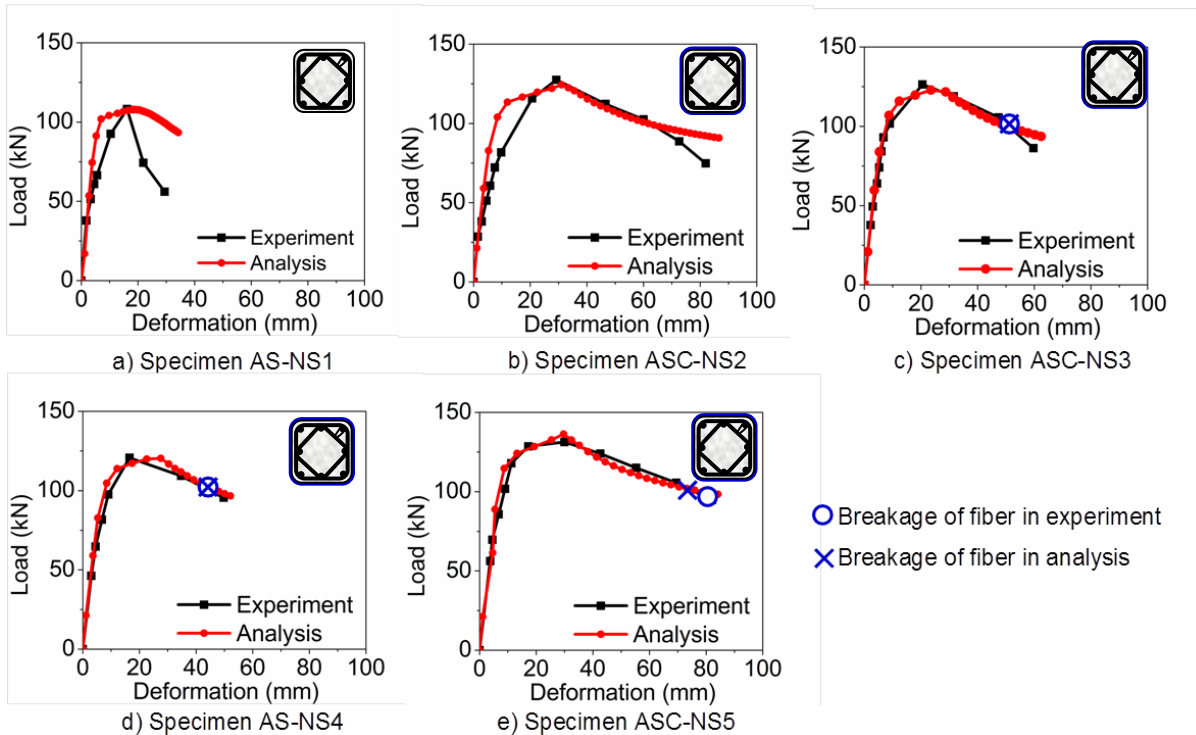


Fig. 5.7 Load-deformation responses of specimens tested by Iacobucci et al. [23]

5.2.2.3. Experimental results of Saatcioglu and Ozceb

To verify the FSI analytical method for plain RC columns, the experimental and analytical results of Saatcioglu and Ozceb [51] are compared in Fig. 5.8. Specimens U1-U4 fail in brittle shear after yielding (Mode II). The analytical approach can accurately predict the post-peak behavior of these plain RC columns.

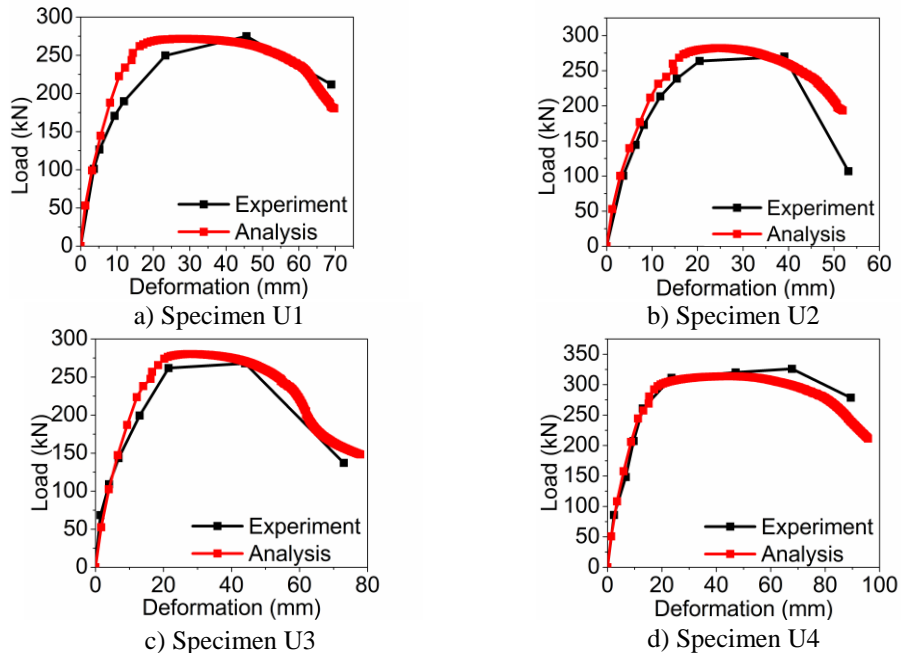


Fig. 5.8 Load-deformation responses of specimens tested by Saatcioglu and Ozceb [51]

5.2.2.4. Experimental results of Sezen et al.

To verify the FSI analytical method for plain RC columns, the experimental and analytical results of Sezen et al. [57] are compared in Fig. 5.9. The load-carrying capacity of Specimens 2CLD12, 2CHD12, 2CVD12 and 2CLD12M fail in less brittle shear after yielding (Mode III) are shown. The analytical approach can accurately predict the post-peak behavior of these plain RC columns.

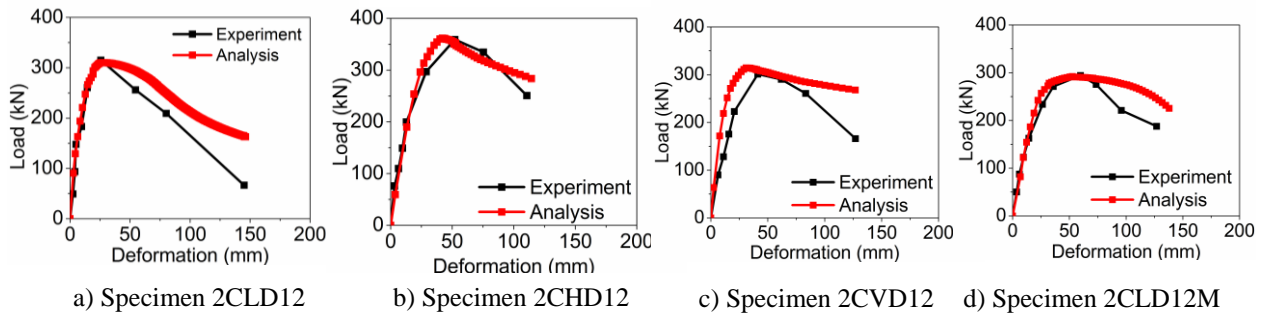


Fig. 5.9 Load-deformation responses of specimens tested by Sezen et al. [57]

5.2.2.5. Experimental results of Aboutaha et al. and Priestley et al.

Steel jacketing is a more common retrofit technique than concrete jacketing. Aboutaha et al. [1] proved that steel jacketing shows several advantages: a smaller increase in the cross-sectional dimensions, ease and speed of construction, lower cost of structural intervention and interruption of use, and a smaller

increase in additional stiffness to the retrofitted column. Figure 5.10 demonstrates the load-deformation responses from the experiment carried out by Aboutaha et al. [1] and from the analytical method. With a rectangular jacket (Specimen SC10 in Fig. 5.10(a)), the column showed subsequent improved behavior compared to the control column (Specimen SC9 in Fig. 5.10 (b)). The steel jacket is effective in a passive confinement. The level of lateral confinement induced in the concrete by flexible restraint as the concrete attempts to expand laterally in the compression zone depends on the strength and stiffness of the steel jacket. The steel jacket also resists the lateral dilation of columns associated with the development of diagonal shear cracks. In both the case of confinement of flexural hinges or potential shear failures, the steel jacket can be considered equivalent to a continuous steel shear reinforcement.

Figure 5.10 demonstrates the load-deformation responses from the experiment of Priestley et al. [45-46] and from the analytical method. By encasing rectangular columns with elliptical steel jackets, as shown in Fig. 5.10 (c)-(d), extensive tests of Priestley et al. [45-46] have established that such jackets provide excellent enhancement of the flexural performance of inadequately confined columns. However, changing the rectangular column section by elliptical jacketing enlarges the column section significantly, and may not always be desirable or practical.

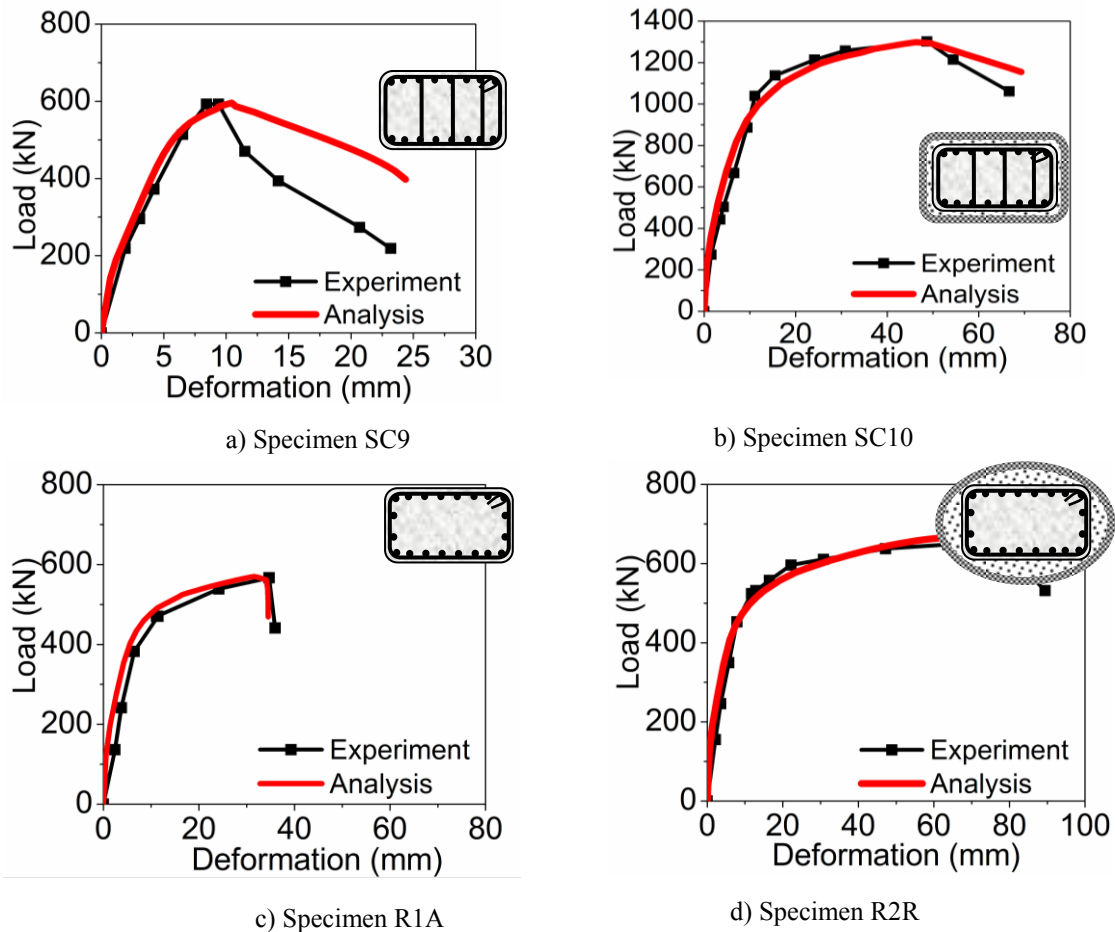


**Fig. 5.10** Load-deformation responses of specimens tested by Aboutaha et al [1] and Priestley et al.[45-46]

The overall load-deformation responses from the analytical predictions agree well with the experiment in terms of both strengths and deformations in the cases of both with and without FRP-jacketing. In addition,

the FSI analytical method is applicable not only to FRP with high fracture strain (PET and PEN) but also to FRP with low fracture strain (AFRP and CFRP).

### 5.3. COMPARISON OF CALCULATED AND MEASURED SHEAR FORCE COMPONENTS

Figure 5.10 shows comparisons of the shear force components and average shear strain obtained from experiments and models. These experimental shear forces are taken from the peak value of each cycle of cyclic load-deformation responses. The experimental shear force carried by transverse steel and fiber reinforcements ( $V'_{s}$ -experiment and  $V'_{f}$ -experiment) is obtained from strain gauges mounted on the transverse steel and fiber reinforcements. The concrete shear force from experiment ( $V'_c$ -experiment) is calculated by subtracting the  $V'_{s+f}$ -value from the applied shear force ( $V$ ). The shear force carried by the transverse steel and fiber reinforcements as calculated from Eq. (4.39) fits well to that of the experiment, as shown in Figs. 5.10a and 5.10b. Moreover, good correlation between the concrete shear force predicted from Eq. (4.40) and that in the experiment is demonstrated in Fig. 5.10c. The average shear strains obtained from the experiment and calculated from Eq. (4.19) are compared, and show good agreement as shown in Fig. 5.10d.

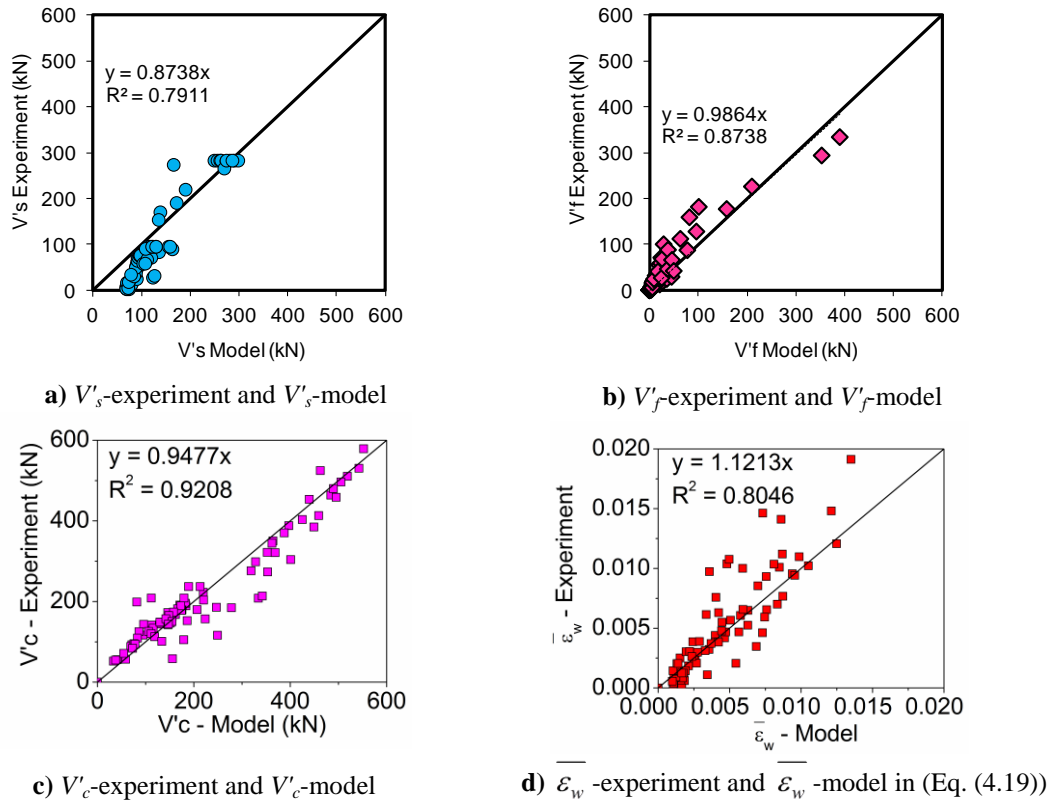


**Fig. 5.10** Comparisons of the shear force components and average shear strain obtained from experiments and models

### 5.4. COMPARISON OF DEFORMATION COMPONENTS FROM EXPERIMENTS AND MODELS

The predicted ultimate deformation of the specimens shown in Table 1 agrees well with the experimental ultimate deformation, as shown in Fig. 5.11. The ultimate deformation state occurs when the deformation

reaches the region where the remaining load-carrying capacity becomes lower than the yield load, as stated in the JSCE seismic specification [28].

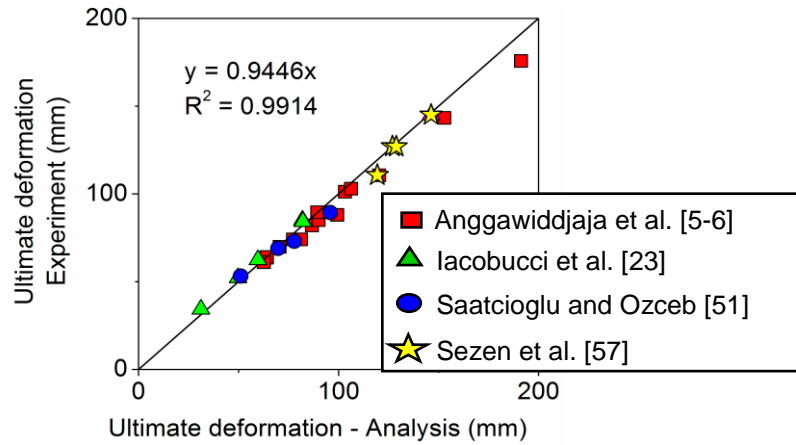


**Fig. 5.11** Ultimate deformation of experiment and analysis

The calculated deformation components of the total deformation at the ultimate deformation agree well with that of the experimental deformation results, as shown by the example of SP5 in Fig. 5.12. It can be seen that the early-stage shear deformation gives a small contribution to the total deformation. After the onset of shear cracking, shear deformation increased significantly. At the ultimate state of the column, the increases in the shear deformation as well as an additional deformation due to the tension shift are significant and should not be neglected. It is evident that the contribution of shear deformations to the total deformations can be significant, especially in RC columns with insufficient transverse steel reinforcement. For instance, the contribution of shear deformation to the total deformation of Specimen SP5 [5-6] significantly increases with increasing deformations as a result of further shear cracking, while inducing an additional deformation due to the tension shift, as shown in Fig. 5.12. Shear deformation after yielding based on the strut angle models is shown in Fig. 5.13.

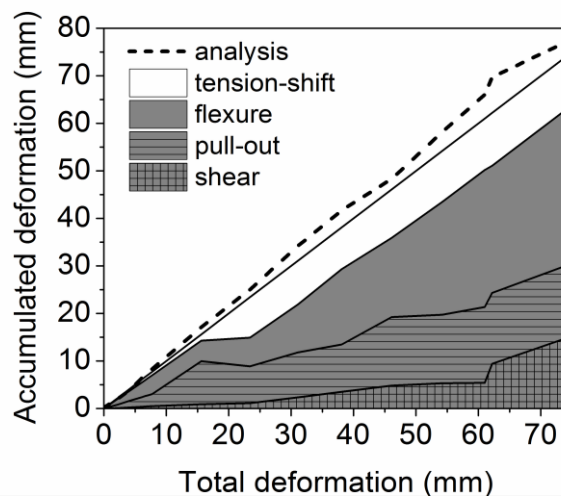
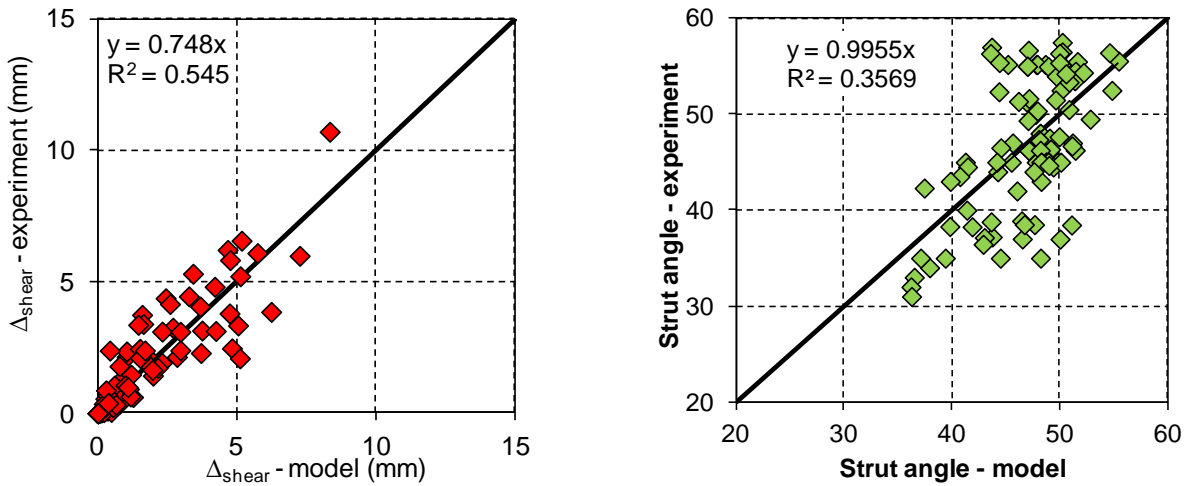


**Fig. 5.12** Deformation components of specimen SP5



a) Shear deformation of experiment and model      b) Compression strut angle of experiment and model

**Fig. 5.13** Shear deformation after yielding

### 5.5. SUMMARY

An accurate prediction method for load and deformation is necessary to ensure the safety of structures. This chapter aimed to develop an analytical method that can precisely predict not only the strength but also the deformation capacity of reinforced concrete columns with and without FRP-jacketing. In summary, the proposed flexure-shear interaction (FSI) analytical method can successfully predict the load-deformation envelope responses of RC columns with and without FRP-jacketing. The flexural strength model meshes with the shear strength model through the neutral axis depth of the shear crack region, whereas the shear strength model meshes with the flexural strength model through the yielding of reinforcement and effective concrete strength. In specimens failing in shear, the reduction in load-carrying capacity with increase in deformation can be considered as a reduction of the contribution of the shear strength behavior caused by the reduction in secant stiffness of both shear and flexural reinforcements and residual concrete strength. However, in specimens failing in flexure, the load-carrying capacity decreases due to concrete crushing along with the buckling of the compression reinforcement. The influence of the shear strength behavior on the flexural deformation is introduced through the tension shift phenomenon which increases the flexural deformation. Meanwhile, the flexural strength behavior affects the shear deformation through the yielding of flexural reinforcement, which decreases the shear strength of concrete and also increases the shear reinforcement strain, causing the increase of the shear deformation. The proposed analytical methods can successfully evaluate the advantage of PET FRP with high fracture strain over conventional FRPs with low fracture strain (e.g., CFRP and AFRP). RC members strengthened by PET FRP have higher strength and deformability whereas RC members strengthened with CFRP and AFRP have high strength but lower deformability. In addition, the FSI analytical methods successfully predict shear strength of RC members jacketed by both FRP sheets and steel plate. This validates the assumption that steel jacket limits the opening of shear cracks in vertical, horizontal and shear directions, whereas FRP jacket can resist the shear crack opening only along the fiber alignment. The proposed analytical method is applicable for RC members with normal strength of concrete, the axial loading ratio range 0-0.65, shear-span to effective-depth ratio of 2.0-4.5, and jacketed with FRP or steel plates. More details of available range will be discussed in the next Chapter.

## CHAPTER 6

### CONCLUSIONS AND FUTURE CONCERN

#### 6.1. CONCLUSIONS

##### 6.1.1. Observed behavior of test specimens and evaluation of experimental data

An experimental program involving tests on ten RC beams strengthened in shear with fully wrapped LRS PET FRP sheets has been conducted. The test parameters include the strengthening ratio, the longitudinal reinforcement ratio as well as the shear-span to effective-depth ratio. The following conclusions can be drawn from the test results:

- (1) PET FRP sheets with a large rupture strain can be used to enhance the shear strength of RC beams while substantially increasing the member ductility. In particular, PET FRP sheets did not rupture at the peak load and led to a ductile shear failure of the strengthened RC members. This failure mode also enabled us to clearly observe the behavior of shear strength degradation of concrete with the increase of shear deformation until the rupture of PET FRP sheets.
- (2) The increase of amount of PET FRP sheets led to an increase of the shear strength and shear ductility whereas a lower longitudinal reinforcement ratio and a smaller shear-span to effective-depth ratio corresponded to improved shear ductility.
- (3) PET FRP sheets developed very high strains; namely the maximum strains of 1.4-6.0% at the peak shear loads and as high as 15.0% at the termination of tests,.
- (4) The initiation of the degradation of the shear contribution of concrete occurred even before the peak strength was developed in PET FRP-strengthened RC members. The shear contribution of concrete was found to degrade by 0-54.6% depending on the volumetric ratio of FRP sheets, the shear-span to effective-depth ratio and the member depth. This degradation of concrete contribution to shear strength is eligible in the case of no axial loading for the current study.

##### 6.1.2. Analytical methods

An accurate prediction method for load and deformation is necessary to ensure the safety of structures. This research aimed to develop an analytical method that can precisely predict not only the strength but also the deformation capacity of reinforced concrete columns with and without FRP-jacketing. The findings of this study can be summarized as follows:

- 1) The proposed flexure-shear interaction (FSI) analytical method can successfully predict the load-deformation envelope responses of RC columns with and without FRP-jacketing. The flexural strength model meshes with the shear strength model through the neutral axis depth of the shear crack region, whereas the shear strength model meshes with the flexural strength model through the yielding of reinforcement and effective concrete strength.
- 2) In specimens failing in shear, the reduction in load-carrying capacity with increase in deformation can be considered as a reduction of the contribution of the shear strength behavior caused by the reduction in secant stiffness of both shear and flexural reinforcements and residual concrete strength. However,

in specimens failing in flexure, the load-carrying capacity decreases due to concrete crushing along with the buckling of the compression reinforcement.

- 3) The influence of the shear strength behavior on the flexural deformation is introduced through the tension shift phenomenon which increases the flexural deformation. Meanwhile, the flexural strength behavior affects the shear deformation through the yielding of flexural reinforcement, which decreases the shear strength of concrete and also increases the shear reinforcement strain, causing the increase of the shear deformation.
- 4) Steel jacket limits the opening of shear cracks in vertical, horizontal and shear directions. However, FRP jacket can resist the shear crack opening in uni-direction occurring only along the fiber alignment.

The FSI analytical method can precisely predict the strain response of shear reinforcement, including the rupture of the FRP jackets. It is proven that FRP with high fracture strain (PEN and PET) is less likely to fracture than conventional fiber (AFTP and CFRP) at ultimate deformation.

### **6.1.3. Applicable range of the proposed analytical methods**

Since RC specimens used to develop models in this current research were tested under limited condition and some parameters, the applicable range of the proposed FSI analytical method for predicting the load-deformation responses should be addressed as follows:

- 1) The shear strength model can be applied in only RC members with normal concrete compressive strength ( $f'_c < 50\text{MPa}$ ). Currently, the advancement of material technology and production has led to higher grades of concrete strengths such as High strength Concrete (HSC). However, HSC is not considered in the current shear strength model.
- 2) The axial load ratio is one of the important factors for shear strength of RC columns. In the current shear strength model, the specimens used for developing models are subjected to the constant axial load ratio ( $P/A_g f'_c$ ) in range 0–0.65.
- 3) The member's shear span is considered by use of the shear-span to effective-depth ratio ( $a/d$ ). It is imperative to address that shear span length of RC members are in the range of normal beams or columns in the current study. Therefore, the  $a/d$ -value is in range 2.0–4.5. This means slender and short RC members (e.g. long or short columns) are not included.
- 4) The application of the current model is limited to the strengthening of undamaged concrete because of the lack of experimental observation of strengthening of damaged concrete. The damaged RC members here are referred to those members exposed in the harsh environment such as chloride attack.
- 5) The analytical method can predict RC members subjected to monotonic flexure-shear loading. To predict the behavior of RC members subjected to the reversed cyclic loading, the FSI analytical method is extended to RC members under cyclic loading. The cyclic loads were applied horizontally to the member's axis with constant axial loading. The displacement was controlled at the top of the specimens. The reversed cycle was applied when longitudinal reinforcement at the bottom of the pier yielded, considered as flexural yielding displacement ( $\delta_y$ ), and the corresponding load was yielding load ( $P_y$ ). Therefore, this type of push-pull loading was applied in all specimens.

## 6.2. FUTURE CONCERN

To have a further completeness of the present study or to formulate direct guidelines on retrofitting design and material selections in retrofitting and strengthening applications, the following issues should be concerned:

- 1) The use of High strength Concrete (HSC) elements ( $f'_c > 50\text{MPa}$ ) for concrete structures has become common in building owing to several advantages of HSC in earthquake resistant structures. Generally, concrete structures are inherently heavy, and hence induce substantial inertial forces. High strength concrete members will have the distinct advantage of reducing these inertial forces by reducing member's sizes. Higher elastic modulus will reduce the drift due to lateral load. Other aspects relevant to high strength concrete members are discussed in the next section. High strength concrete is structurally a different material and rules applicable to normal strength concrete are not always conservative when applied to high strength concrete because of their different in fracture modes and microstructure. Therefore, current shear strength model, originally intended for concrete strengths ( $f'_c < 50\text{MPa}$ ), needs to be re-evaluated for HSC in the future.
- 2) The axial load can represent the weight of superstructures (e.g. bridge decks and bridge slabs) on RC columns or bridge piers. During major earthquakes, the axial loads are varied owing to level ground shaking. Therefore, the inconstant axial load should be concerned to ensure that the RC columns can carry weight of superstructures.
- 3) The shear-span to effective-depth ratio ( $a/d$ ) significantly influences to shear behavior of RC members. Slender RC members are always dominated by flexural strength behavior, whereas short (or deep) RC members are usually dominated by shear strength behavior. As a result, RC members with different  $a/d$ -value entirely exhibit dissimilar failure modes, depending on the range of the  $a/d$ -value. Hence, wider range of  $a/d$ -value should be extended to demonstrate more precise behaviors of RC members subjected to seismic loads.
- 4) Generally, RC members exposed to severe environments such as chloride attack are often deteriorated, leading to reduction of their life cycle. Their damaging effects due to exposure environment should be evaluated before seismic strengthening in order to improve the prediction of their seismic performance. Future study for this issue will aim to clarify the effect of chloride attack prior seismic strengthening. One of the deteriorations is the reduction of steel reinforcement's area because of corrosion. This project will be cooperated with the research group in Zhejiang University, China.
- 5) During serious seismic events, behaviors of RC structures subjected to reversed cyclic loading depend on a loading speed or strain increment rate, known as a loading history. This loading speed significantly influences the material properties of RC structures and their behaviors, especially in seismic loading. Therefore, the current study is successfully satisfied in the cases of RC structures under static loading precisely. However, it has been confirmed experimentally that the behavior under static loading is similar to that under seismic loading. In the cases of seismic loading, the influence of load history on material behaviors can be investigated by applying different number of cycles, as shown in Fig. 6.1. This shows different number of loading histories, representing various ground shaking accelerations. For RC structures loaded under less number of cycles in each peak loading history (Fig. 6.1a), the ultimate deformation reaches much later whereas, for RC structures

loaded under more number of cycles in each peak loading history (Fig. 6.1b), the ultimate deformation can reach earlier. Considering each peak loading history, the damages due to higher number of cycles are more serious than that due to lower number of cycles. It is worthwhile mentioning here that the various types of loading histories should be further investigated to ensure the damage level of RC structures under seismic loading.

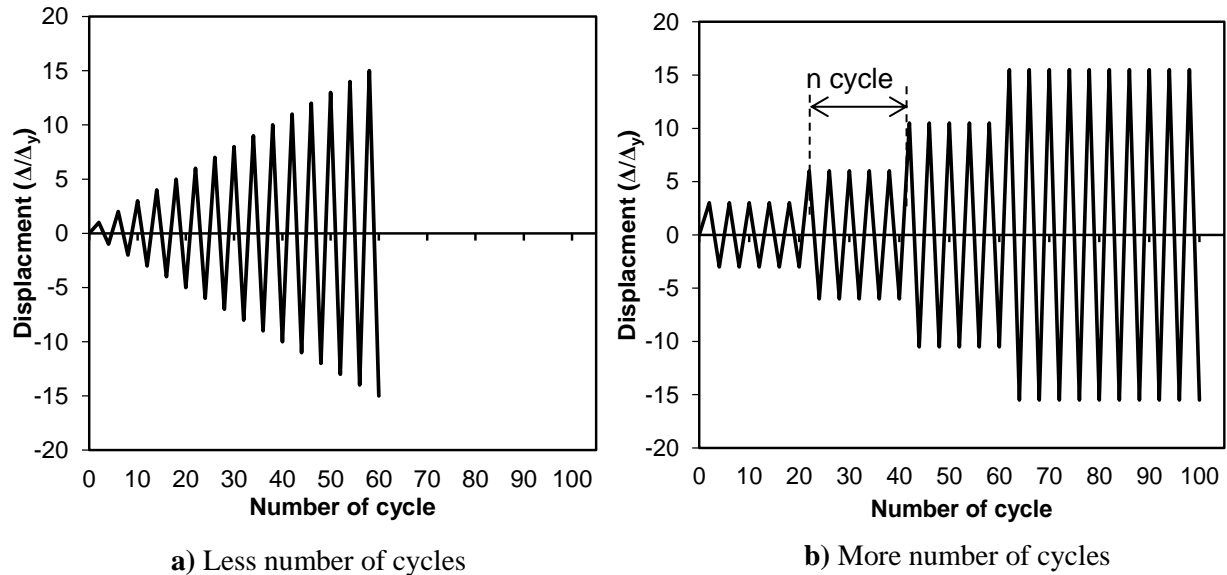


**Fig. 6.1** Variation of loading history

- 6) For seismic strengthening, there are several materials commonly used to improve seismic performance such as FRP, steel, concrete and cementitious materials. To justify the most appropriate material for seismic strengthening, other alternative materials, besides FRP and steel plates, should be investigated extensively. Finally, the comparison between alternative materials to help engineers select appropriate materials for construction.

In addition, the validity of the proposed analytical method should be extended to more case studies. The current analytical method and computer programming developed in this research will be world widely opened to other researchers in order to permit more investigation of this analytical method. In the future, the analytical programs will be uploaded.

## REFERENCES

- [1] Aboutaha, R. S., Engelhardt, M. D., Jirsa, J. O., and Kreger, M. E. (1999). "Rehabilitation of shear critical concrete columns by use of rectangular steel jackets." *ACI Structural Journal*, 96(1), 68-78.
- [2] ACI Committee 318. (2005). "Building code requirements for structural concrete (ACI 318-05)." *American Concrete Institute*, Farmington Hills, MI, USA.
- [3] ACI Committee 440. (2002). "Guide for the design and construction of externally bonded FRP systems for strengthening concrete structures." *American Concrete Institute*, Farmington Hills, MI, USA.
- [4] Alsiwat, J. M., and Saatcioglu, M. (1992). "Reinforcement anchorage slip under monotonic loading." *Journal of Structural Engineering*, 118(9), 2421-2438.
- [5] Anggawidjaja, D., Ueda, T., Dai, J., and Nakai, H. (2006). "Deformation capacity of RC piers wrapped by new fiber-reinforced polymer with large fracture strain." *Journal of Cement and Concrete Composites*, 28(10), 914-927.
- [6] Anggawidjaja, D., and Ueda, T. (2009). "PET, high fracturing strain fiber, for concrete structure retrofitting: shear force and deformation enhancement: experiments, analysis and model." VDM Verlag Dr. Müller, Germany, 1-64.
- [7] Bai, Y.L., Dai, J.G. and Teng, J.G. (2013). "Cyclic compressive behavior of concrete confined with large rupture strain FRP composites." *Journal of Composites for Construction*, ASCE (Accepted for publications)
- [8] Bakis, C. E., Bank, L. C., Brown, V. L., Cosenza, E., Davalos, J. F., Lesko, J. J., Machida, A., Rizkalla, S. H., and Triantafillou, T. C. (2002). "Fiber-reinforced polymer composites for construction-state-of-the-art review." *Journal of Composites for Construction*, ASCE, 6(2), 73-87.
- [9] Bentz, E. C., Vecchio, F. J., and Collins, M. P. (2006). "Simplified modified compression field theory for calculating shear strength of reinforced concrete elements." *ACI Structural Journal*, 103(4), 614.
- [10] Branson, D. E. (1968). "Design procedures for computing deflections." *ACI Journal Proceedings*, 65(9), 730-742.
- [11] Canadian Standards, A. (2004). "Design of Concrete Structures (CSA-A23. 3-04)." Mississauga, Ontario, 1-214.
- [12] CEB-FIP Model Code 90. (1993). Design code. Thomas Telford, London.
- [13] Chaallal, O., Nollet, M. J., and Perraton, D. (1998). "Strengthening of reinforced concrete beams with externally bonded fiber-reinforced-plastic plates: Design guidelines for shear and flexure." *Canadian Journal of Civil Engineering*, 25(4), 692-704.
- [14] Dai, J. G., Bai, Y.L. and Teng, J.G. (2011), "Behavior and modeling of concrete confined with FRP composites of large deformability." *Journal of Composites for Construction*, ASCE, 15(6), 963-973.
- [15] Dai, J.G., Lam, L., and Ueda, T. (2012). "Seismic retrofit of square RC columns with polyethylene terephthalate (PET) fibre reinforced polymer composites." *Journal of Construction and Building Materials*, 27(1), 206-217.
- [16] Dai, J. G. and Ueda, T. (2012). "Strength and deformability of concrete members wrapped with fibre reinforced polymer composites with a large rupture strain." *Journal of Innovative Materials and Techniques in Concrete Construction*, 14, 225-241.
- [17] Dhakal, R. P., and Maekawa, K. (2002). "Modeling for postyield buckling of reinforcement." *Journal of Structural Engineering*, 128(9), 1139-1147.

- [18] Debernardi, P. G., and Taliano, M. (2006). "Shear deformation in reinforced concrete beams with thin web." *Magazine of Concrete Research*, 58(3), 157-171.
- [19] Elwood, K. J., and Eberhard, M. O. (2009). "Effective stiffness of reinforced concrete columns." *ACI Structural Journal*, 106(4).
- [20] FIB. (2001). "Externally Bonded FRP Reinforcement for RC Structures," *The International Federation for Structural Concrete*. Lausanne, Switzerland.
- [21] Hines, E. M., Restrepo, J. I., and Seible, F. (2004). "Force-displacement characterization of well-confined bridge piers." *ACI Structural Journal*, 101(4), 537-548.
- [22] Hsu, T. T. C. (1988). "Softened truss model theory for shear and torsion." *ACI Structural Journal*, 85(6), 624-635.
- [23] Iacobucci, R. D., Sheikh, S. A., and Bayrak, O. (2003). "Retrofit of square concrete columns with carbon fiber-reinforced polymer for seismic resistance." *ACI Structural Journal*, 100(6), 785-794.
- [24] Ito, A., Aoki, Y., and Hashimoto, S. (2002). "Accurate extraction and measurement of fine cracks from concrete block surface image." *Proceeding of 28<sup>th</sup> Annual Conference of the Industrial Electronics Society*, Industrial Electronics Society, 3(1), 2202-2207.
- [25] Japan Society of Civil Engineers (JSCE). (2001). "Recommendations for upgrading of concrete structures with use of continuous fiber sheets." *Japan Society of Civil Engineers*, Tokyo, 41.
- [26] Japan Society of Civil Engineers (JSCE). (2002). "Test method for tensile properties of continuous fiber sheets." *Japan Society of Civil Engineers*, JSCE-E541-2000.
- [27] Japan Society of Civil Engineers (JSCE) Series 41. (2007). "Standard specification for concrete structures - structural performance verification." *Japan Society of Civil Engineers*, Tokyo.
- [28] Japan Society of Civil Engineers (JSCE) Series 5. (2007). "Standard specification for concrete structures - seismic performance verification." *Japan Society of Civil Engineers*, Tokyo.
- [29] Jaqin, H., Nakai, H., Ueda, T., Sato Y., and Dai, J. (2005). "Seismic retrofitting of RC piers using continuous fiber sheet with large fracturing strain." *Journal of Structural Engineering*, JSCE, 51A , 893-902.
- [30] Jirawattanasomkul, T., Ikoma, Y., Zhang D., and Ueda, T. (2011) "Shear strength of reinforced concrete members strengthened with FRP jacketing." *Proceedings of Japan Concrete Institute*, Japan Concrete Institute, 33(2), 991-996.
- [31] Karbhari, V. M., and Zhao, L. (2000). "Use of composites for 21st century civil infrastructure." *Computer Methods in Applied Mechanics and Engineering*, 185(2-4), 433-454.
- [32] Kuchma, D., Yindeesuk, S., Nagle, T., Hart, J., and Lee, H. H. (2008). "Experimental validation of strut-and-tie method for complex regions." *ACI Structural Journal*, 105(5), 578-589.
- [33] Lechat, C., Bunsell, A. R., and Davies, P. (2011). "Tensile and creep behavior of polyethylene terephthalate and polyethylene naphthalate fibres." *Journal Material Science*, 46(2), 528-533.
- [34] Maekawa, K., and An, X. (2000). "Shear failure and ductility of RC columns after yielding of main reinforcement." *Engineering Fracture Mechanics*, 65(2-3), 335-368.
- [35] Mander, J. B., Priestley, M. J. N., and Park, R. (1988). "Theoretical Stress-strain Model for Confined Concrete." *Journal of Structural Engineering*, 114(8), 1804-1826.
- [36] Markeset, G., and Hillerborg, A. (1995). "Softening of concrete in compression - Localization and size effects." *Cement and Concrete Research*, 25(4), 702-708.
- [37] Massone, L. M., and Wallace, J. W. (2004). "Load-deformation responses of slender reinforced concrete walls." *ACI Structural Journal*, 101(1), 103-113.

- [38] Mostafaei, H., and Kabeyasawa, T. (2007). "Axial-shear-flexure interaction approach for reinforced concrete columns." *ACI Structural Journal*, 104(2), 218-226.
- [39] Mostafaei, H., and Vecchio, F. J. (2008). "Uniaxial shear-flexure model for reinforced concrete elements." *Journal of Structural Engineering*, ASCE, 134(9), 1538-1547.
- [40] Ozcebe, G., and Saatcioglu, M. (1989). "Hysteretic shear model for reinforced concrete members." *Journal of Structural Engineering*, 115(1), 132-148.
- [41] Park, H. G., Yu, E. J., and Choi, K. K. (2012). "Shear-strength degradation model for RC columns subjected to cyclic loading." *Engineering Structures*, 34, 187-197.
- [42] Park, J. W., and Kuchma, D. (2007). "Strut-and-tie model analysis for strength prediction of deep beams." *ACI Structural Journal*, 104(6), 657-666.
- [43] Pesic, N., and Pilakoutas, K. (2005). "Flexural analysis and design of reinforced concrete beams with externally bonded FRP reinforcement." *Materials and Structures*, 38(2), 183-192.
- [44] Placas, A., and Regan, P. E. (1971). "Shear failure of reinforced concrete beams." *ACI Journal Proceedings*, 68(10), 763-773.
- [45] Priestley, M. J. N., Seible, F., Xiao, Y., and Verma, R. (1994). "Steel jacket retrofitting of reinforced concrete bridge columns for enhanced shear strength-Part 1: Theoretical considerations and test design." *ACI Structural Journal*, 91(4), 394-405.
- [46] Priestley, M. J. N., Seible, F., and Xiao, Y. (1994). "Steel jacket retrofitting of reinforced concrete bridge columns for enhanced shear strength--Part 2: Test results and comparison with theory." *ACI Structural Journal*, 91(5), 537-551.
- [47] Priestley, M. J. N., Verma, R., and Xiao, Y. (1994). "Seismic shear strength of reinforced concrete columns." *Journal of Structural Engineering*, ASCE, 120(8), 2310-2327.
- [48] Priestley, M. J. N. (2000). "Performance-based seismic design." Keynote Address, *Proceeding of 12<sup>th</sup> World Conference on Earthquake Engineering*, Auckland, New Zealand, 1-22.
- [49] Priestley MJN, Calvi GM, Kowalsky MJ. (2007). "Direct displacement-based seismic design of structures", *IUSS Press*, Pavia, Italy.
- [50] Qi, C., Weiss, J., and Olek, J. (2003). "Characterization of plastic shrinkage cracking in fiber reinforced concrete using image analysis and a modified Weibull function." *Materials and Structures*, 36(6), 386-395.
- [51] Saatcioglu, M., and Ozcebe, G. (1989). "Response of reinforced concrete columns to simulated seismic loading." *ACI Structural Journal*, 86(1), 3-12.
- [52] Sato, Y., Ueda, T., and Kakuta, Y. (1997). "Shear strength of reinforced and prestressed concrete beams with shear reinforcement." *Concrete Library International of JSCE*, 29, 233-247.
- [53] Sato Y, Ueda T, Kakuta Y. "Shear resisting model of reinforced and prestressed concrete beams based on finite element analysis. *Bulletin of the Faculty of Engineering*, Hokkaido University, No 171. 1994:1-17.
- [54] Sato Y, Ueda T, Kakuta Y. (1996). "Shear strength of prestressed concrete beams with FRP tendon. *Concrete Library of JSCE*, 27, 189-208.
- [55] Seible, F., Priestley, M. J. N., Hegemier, G. A., and Innamorato, D. (1997). "Seismic retrofit of RC columns with continuous carbon fiber jackets." *Journal of Composites for Construction*, ASCE, 1(2), 52-62.
- [56] Senda, M. and Ueda, T. (2008). "Experimental study on shear strengthening by continuous fiber with high fracturing strain." *Proceedings of the Concrete Structure Scenarios*, JSMS, 8, 249-256 (in Japanese).

- [57] Sezen, H., and Moehle, J. P. (2004). "Shear strength model for lightly reinforced concrete columns." *Journal of Structural Engineering*, 130(11), 1692-1703.
- [58] Sezen, H., and Setzler, E. J. (2008). "Reinforcement slip in reinforced concrete columns." *ACI Structural Journal*, 105(3), 280-289.
- [59] Shima, H., Chou, L.-L., and Okamura, H. (1987). "Micro and macro models for bond in reinforced concrete." *Journal of the Faculty of Engineering*, University of Tokyo, 39(2), 133-194.
- [60] Sigrist, V. (2011). "Generalized Stress Field Approach for Analysis of Beams in Shear." *ACI Structural Journal*, 108(4), 479-487.
- [61] Sirbu, G., Ueda, T., and Kakuta, Y. (2001). "A study on shear resisting mechanism of RC columns strengthened with carbon fiber sheets." *Journal of Structural Engineering*, JSCE, 47(3), 1289-1298.
- [62] Susantha, K. A. S., Ge, H., and Usami, T. (2001). "Uniaxial stress-strain relationship of concrete confined by various shaped steel tubes." *Engineering Structures*, 23(10), 1331-1347.
- [63] Tumialan, G., Nanni, A., Ibell, T., and Fukuyama, H. (2002). "FRP composites for strengthening civil infrastructure around the world." *Sampe Journal*, 38(5), 9-15.
- [64] Ueda, T., Pantaratorn, N., and Sato, Y. (1995). "Finite element analysis on shear resisting mechanism of concrete beams with shear reinforcement." *Proceedings-Japan Society of Civil Engineers*, 273-286.
- [65] Ueda, T., Sato, Y., Ito, T., and Nishizono, K. (2002). "Shear deformation of reinforced concrete beam." *Journal of Materials*, Concrete Structures and Pavements, JSCE, 711(56), 205-215.
- [66] Ueda, T., (2009). "Seismic application of sustainable fiber material." *Proceedings of US-Japan Workshop*. US-Japan Workshop on Life Cycle Assessment of Sustainable Infrastructure Materials, Sapporo, Japan, October, 1-9.
- [67] Vecchio, F. J., and Collins, M. P. (1986). "The modified compression-field theory for reinforced concrete elements subjected to shear." *ACI Journal*, 83(2), 219-231.
- [68] Vecchio, F. J. (1989). "Nonlinear finite element analysis of reinforced concrete membranes." *ACI Structural Journal*, 86(1), 26-35.
- [69] Wang, Y. C., and Restrepo, J. I. (2001). "Investigation of concentrically loaded reinforced concrete columns confined with glass fiber-reinforced polymer jackets." *ACI Structural Journal*, 98(3), 377-385.
- [70] Wang, Y. C. (2003). "Analytical and experimental study on seismic performance of RC T-beams with design deficiency in steel bar curtailment." *Engineering Structures*, 25(2), 215-227.
- [71] Xu, S. Y., and Zhang, J. (2012). "Axial-shear-flexure interaction hysteretic model for RC columns under combined actions." *Engineering Structures*, 34, 548-563.

**APPENDIX A**

**Calculation of shear contribution**

According to JSCE specifications, JSCE 2001; JSCE 2007 [23,25], total shear strength ( $v_t$ ) consists of the contribution to shear strength due to concrete ( $v_c$ ), transverse steel reinforcement ( $v_s$ ) and FRP sheet ( $v_f$ ).

$$v_t = v_c + v_s + v_f \quad (\text{A-1})$$

The concrete and transverse steel contributions to shear strength can be calculated as follows:

$$v_c = 0.20 \cdot \sqrt[3]{f'_c} \cdot \sqrt[4]{1000/d} \cdot \sqrt[4]{100\rho_w} \quad (\text{A-2})$$

$$v_s = \left[ A_w f_{wy} (\sin \alpha_s + \cos \alpha_s) / s_s \right] \cdot z / (bd) \quad (\text{A-3})$$

where  $f'_c$  is compressive strength of concrete;  $b$  is width of member,  $d$  is effective depth of member;  $\rho_w$  is ratio of transverse steel reinforcement;  $A_w$  is cross-sectional area of transverse steel reinforcement;  $f_{wy}$  is yielding strength of transverse reinforcement;  $\alpha_s$  is angle of transverse steel reinforcement to the member's axis; and  $z$  is  $d/1.15$ .

The shear contribution provided by FRP sheet is its tensile capacity and is computed based on the shear reinforcing efficiency of the FRP sheet ( $K$ ) as shown in Eq. (A-4).

$$v_f = K \cdot \left[ A_f f_{fu} (\sin \alpha_f + \cos \alpha_f) / s_f \right] \cdot z / (bd) \quad (\text{A-4})$$

where  $K = 1.68 - 0.67R$  in which  $0.4 \leq K \leq 0.8$  and  $R = (\rho_f E_f)^{1/4} (f_{fu} / E_f)^{2/3} (1 / f'_c)^{1/3}$  in which  $0.5 \leq R \leq 2.0$ ;  $A_f$  is cross-sectional area of the FRP sheet;  $f_{fu}$  is design tensile strength of the FRP sheet ( $\text{N/mm}^2$ );  $s_f$  is spacing of the FRP sheet;  $E_f$  is modulus of elasticity of the FRP sheet ( $\text{kN/mm}^2$ );  $\rho_f$  is volumetric ratio of the FRP sheet; and  $\alpha_f$  is angle of the FRP sheet to the member axis.